Identification of affected cellular targets, mechanisms and signaling pathways in a mouse model for spinal muscular atrophy with respiratory distress type 1 (SMARD1)

.....

Identifizierung betroffener zellulärer Zielmoleküle, Mechanismen und Signalwege in einem Maus-Modell für spinale Muskelatrophie mit Ateminsuffizienz Typ 1 (SMARD1)

Julius-Maximilians-Universität Würzburg

Doctoral thesis for a doctoral degree
at the Institute of Clinical Neurobiology
and
at the Graduate School of Life Sciences,
Julius-Maximilians-Universität Würzburg,
Section Neuroscience

submitted by

Verena Surrey

from

Haan, Germany

Würzburg 2018

Submitted on: ……..……..

Office stamp

Members of the *Promotionskomitee*:

Chairperson: Prof. Dr. Markus Sauer

Primary Supervisor: PD Dr. Sibylle Jablonka

Supervisor (Second): Prof. Dr. Utz Fischer

Supervisor (Third): Prof. Dr. Carmen Villmann

Date of Public Defense: ……

Date of Receipt of Certificates: ……..

Table of Contents

Abstract

Spinal muscular atrophy with respiratory distress type 1 (SMARD1) is a fatal monogenic motoneuron disease in children with unknown etiology caused by mutations in the *immunoglobulin μ-binding protein 2* (*IGHMBP2*) gene coding for DNA/RNA ATPase/helicase. Despite detailed knowledge of the underlying genetic changes, the cellular mechanisms leading to this disease are not well understood. In the *Nmd*^{2J} ("neuromuscular disorder") mouse, the mouse model for the juvenile form of SMARD1 patients, in which similar pathological features as diaphragmatic paralysis and skeletal muscle atrophy are observed. *Ex vivo* studies in *Nmd*^{2J} mice showed that loss of the motor axon precedes atrophy of the gastrocnemius muscle and does not correlate with neurotransmission defects in the motor endplate. The already described independent myogenic anomalies in the diaphragm and heart of the *Nmd*^{2J} mouse raised the question whether spinal motoneuron degeneration develops cell autonomously. Ighmbp2 is predominantly localized in the cytoplasm and seems to bind to ribosomes and polysomes, suggesting a role in mRNA metabolism.

In this Ph.D. thesis, morphological and functional analyses of isolated Ighmbp2-deficient (Ighmbp2-def.) motoneurons were performed to answer the question whether the SMARD1 phenotype results from dysregulation of protein biosynthesis. Ighmbp2-deficient motoneurons show only negligible morphological alterations with respect to a slight increase in axonal branches. This observation is consistent with only minor changes of transcriptome based on RNA sequencing data from Ighmbp2-deficient motoneurons. Only the mRNA of *fibroblast growth factor receptor 1 (Fgfr1)* showed significant up-regulation in Ighmbp2-deficient motoneurons. Furthermore, no global aberrations at the translational level could be detected using pulsed SILAC (Stable Isotope Labeling by Amino acids in cell culture), AHA (L-azidohomoalanine) labeling and SUnSET (SUrface SEnsing of Translation) methods. However, a reduced β-actin protein level was observed at the growth cones of Ighmbp2-deficient motoneurons, which was accompanied with a reduced level of Imp1 protein, a known *β-actin* mRNA interactor. Live-cell imaging studies using fluorescence recovery after photobleaching (FRAP) showed translational down-regulation of eGFP^{myr}-β-actin 3'UTR mRNA in the growth cones and the cell bodies, although the amount of *β-actin* mRNA and the total protein amount in Ighmbp2-deficient motoneurons showed no aberrations. This compartment-specific reduction of β-actin protein occurred independently of a non-existent direct IGHMBPF2 binding to *β-actin* mRNA. *Fgfr1*, which was upregulated on the RNA level, did not show an increased protein amount in Ighmbp2-deficient motoneurons, whereas a reduced amount could be detected. Interestingly, a correlation could be found between the reduced amount of the Imp1 protein and the increased *Fgfr1* mRNA, since the IMP1 protein binds the *FGFR1* mRNA and thus could influence the transport and translation of *FGFR1*

mRNA. In summary, all data suggest that Ighmbp2 deficiency leads to a local but modest disturbance of protein biosynthesis, which might contribute to the motoneuron defects of SMARD1.

Zusammenfassung

Die spinale Muskelatrophie mit Atemnot Typ 1 (SMARD1) ist eine tödliche, monogene Motoneuron-Erkrankung bei Kindern mit unbekannter Ätiologie. SMARD1 wird durch Mutationen im *Immunoglobulin µ-bindenden Protein 2* (*IGHMBP2*)-Gen verursacht, welches für eine DNA/RNA ATPase/Helikase kodiert. Trotz detaillierter Kenntnisse über die zugrunde liegenden genetischen Veränderungen sind die zellulären Mechanismen, die zu dieser Krankheit führen, nicht gut verstanden. In der *Nmd*^{2J} („neuromuscular disorder“) Maus, dem Mausmodell für die juvenile Form von SMARD1-Patienten, werden ähnliche pathologische Merkmale wie Diaphragma-Lähmung und Skelettmuskelatrophie beobachtet. *Ex vivo*-Studien an *Nmd*^{2J}-Mäusen zeigten, dass der Verlust des motorischen Axons einer Atrophie des Gastrocnemius-Muskels vorausgeht und nicht mit Neurotransmissionsfehlern an der motorischen Endplatte korreliert. Die bereits beschriebenen, unabhängig auftretenden myogenen Anomalien in Zwerchfell und Herz der *Nmd*^{2J}-Maus führten zu der Frage, ob sich die spinale Motoneuron-Degeneration zellautonom entwickelt. Ighmbp2 ist prädominant im Zytoplasma lokalisiert und scheint an Ribosomen und Polysomen zu binden, was auf eine Rolle im mRNA-Stoffwechsel hindeutet.

In dieser Doktorarbeit wurden morphologische und funktionelle Analysen von isolierten Ighmbp2-defizienten (Ighmbp2-def.) Motoneuronen durchgeführt, um die Frage zu beantworten, ob der SMARD1-Phänotyp aus der Deregulierung der Proteinbiosynthese resultiert. Ighmbp2-defiziente Motoneuronen weisen nur geringfügige morphologische Unterschiede hinsichtlich einer leichten Zunahme der axonalen Verzweigungen auf. Diese Beobachtung steht im Einklang mit nur geringen Veränderungen im Transkriptom basierend auf den RNA-Sequenzierungs-Daten in Ighmbp2-defizienten Motoneuronen. Ausschließlich die mRNA des *Fibroblasten-Wachstumsfaktor-Rezeptor 1* (*Fgfr1*) zeigte eine signifikante Hoch-Regulation in Ighmbp2-defizienten Motoneuronen. Des Weiteren konnten keine globalen Aberrationen auf der translationalen Ebene mit Hilfe der gepulsten SILAC (Stable Isotope Labeling by Amino acids in der Zellkultur), AHA (L-Azidohomoalanin)-Markierung und der SUnSET (SUrface SEnsing of Translation) Methoden ermittelt werden. Jedoch konnte eine verringerte β-actin Proteinmenge an den Wachstumskegeln von Ighmbp2-defizienten Motoneuronen beobachtet werden, die von einer Reduktion an Imp1 Protein, einem bekannten *β-actin* mRNA Interaktor, begleitet wurde. Lebendzell-Bildgebungsstudien mittels Fluoreszenz-Recovery after Photobleaching (FRAP) Untersuchung zeigten eine translatorische Herunter-Regulation der eGFP^{myr}-β-actin 3‘UTR mRNA in Wachstumskegeln und Zellkörpern, obwohl die Menge an *β-actin* mRNA und die Gesamt-Proteinmenge in Ighmbp2-defizienten Motoneuronen im Vergleich zu wildtypischen Motoneuronen unverändert war. Diese Kompartiment-spezifische Reduktion von β-actin Protein trat unabhängig von einer nicht vorhandenen direkten IGHMBP2-Bindung an die *β-actin* mRNA

auf. Der auf RNA Ebene hochregulierte *Fgfr1* zeigte hingegen keine erhöhte, aber eine verringerte Proteinmenge in Ighmbp2-defizienten Motoneuronen. Interessanterweise konnte ein Zusammenhang zwischen der reduzierten Menge des Imp1 Proteins und der erhöhten *FGFR1* mRNA gezogen werden. Da das IMP1 Protein neben der *β-actin* mRNA ebenfalls die *FGFR1* mRNA bindet, könnte es so den Transport und die Translation beeinflussen.

Alle Daten deuten zusammenfassend daraufhin, dass Ighmbp2-Mangel zu einer lokalen und geringen Störung der Proteinbiosynthese führt, die aber durchaus zu den beobachteten Motoneuron-Defekten in SMARD1 beitragen könnte.

1. Introduction

Science has been driven for years by the fascination of neurobiology to focus extensively on the development and complex organization of the central nervous system (CNS). Due to the evolutionary progress of this organ, higher organisms can adapt to various environmental influences by developing flexible regulatory mechanisms. These diverse mechanisms are present in embryonic development as well as in the adult organism and are mediated by hormones, neurotrophic factors and extracellular matrix proteins (Kanning et al., 2010; Klausmeyer et al., 2011; Sendtner et al., 2000). In the case of dysfunction of these mechanisms, the crucial role can be recognized, as a result of a neurodegenerative disease. Motoneuron research offers promising ways for possible treatments and thus represents a great motivation for research.

1.1 The Development of the Spinal Cord

Development of the spinal cord is under the control of various developmental control genes and homeodomain (HD) transcription factors. The sonic hedgehog (Shh) concentration gradient decreasing from ventral to dorsal influences the expression of HD transcription factors (Fig. 1A). If the Shh concentration is increased, it suppresses the expression of Class I HD transcription factors such as Pax6, Pax7, Dbx1, Dbx2, and Irx3, whereas the same concentration induces the expression of Class II HD transcription factors such as Nkx6 and Nkx2.2 (Fig. 1B). Five specialized neuroepithelial domains (p0, p1, p2, p3, and pMN) are formed due to the different expression patterns of the different homeodomain proteins along the proliferative ventricular zone. Within these domains, the differentiation of different neuron types and glial cells takes place (Fig. 1B).

During neurogenesis, motoneurons develop from the pMN precursor domain, whereas interneurons emerge from the other four precursor domains (Dessaud et al., 2008). With the delayed onset of gliogenesis, the oligodendrocyte precursors differentiate from the pMN precursor domain and the other four precursor domains take over the formation of astrocytes (Briscoe et al., 2000; Ericson et al., 1996; Lee et al., 2000).

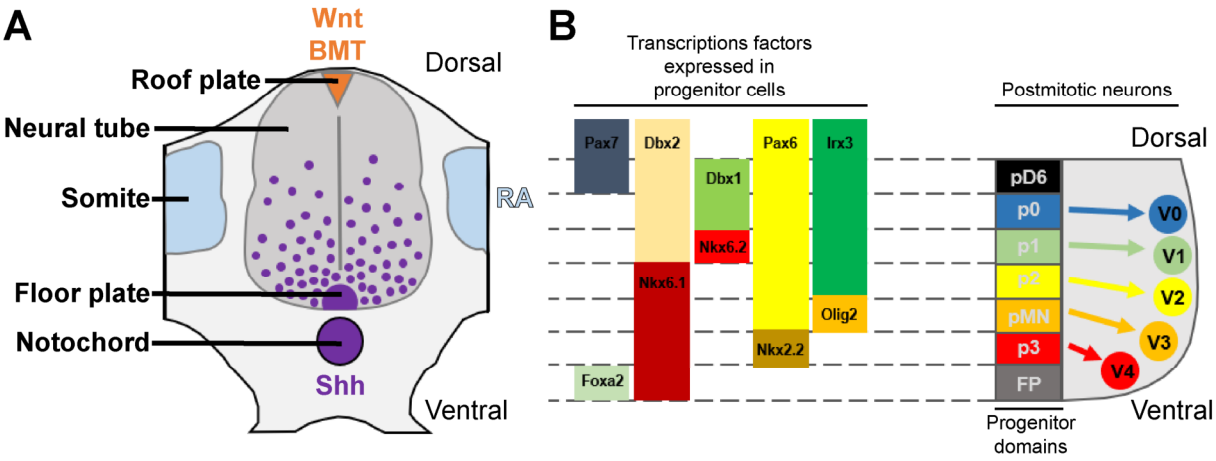

Figure 1 - Dorsal-ventral patterns of progenitor domains in the neural tube are influenced by secreted signals by regulating the spatial expression of transcription factors. (A) Schematic transverse section of an amniotic embryo. Different neurons are produced by the signals in the neural tube and the surrounding tissue within the spinal cord. One of the most important signals is the Shh concentration gradient (purple). Retinoic acid (RA, light blue) is produced from the surrounding Somites and flanking the neural tube. From the roof plate, BMP and Wnt signals (orange) are secreted. (B) Schematic representation of the ventral half of the neural tube. Depending on the Shh concentration gradient, different HD transcription factors are expressed. The same concentration of Shh suppresses the expression of Class I HD transcription factors such as Pax6, Pax7, Dbx1, Dbx2 and Irx3 and induces the expression of Class II HD transcription factors such as Nkx6 and Nkx2. These different expression patterns of the different homeodomain proteins form five specialized neuroepithelial domains (p0, p1, p2, p3, and pMN) along the proliferative ventricular zone. Modified according to (Dessaud et al., 2008).

1.2 Neurotrophic Factors

Neurotrophic factors are small survival factors that play a crucial role in the development of the nervous system (Levi-Montalcini, 1987). At the beginning of the embryogenesis, numerous types of neurons are produced in abundance and in the following developmental process these immature neurons compete for the limiting neurotrophic factors secreted by the target tissue (Oppenheim, 1991). Neurons which were able to form functional connections survive while the other neurons die. The neuronal target tissue releases only minimal amounts of neurotrophic factors, and the excess unlinked neurons are eliminated by apoptosis. This process is called the "neurotrophin hypothesis" (Barde, 1989; Korsching, 1993; Levi-Montalcini, 1987; Thoenen and Barde, 1980; Thoenen, 1995). This observation was the basis for the identification of neurotrophic factors in the twentieth century (Sendtner, 2014). The group of neurotrophic factors can be divided into five different families (Sendtner et al., 2000): the leukemia inhibitory factor (LIF) / Ciliarly neurotrophic factor (CNTF) family, the hepatocyte growth factor (HGF)/ scatter factor (SF) family, the insulin-like growth-factor family, the glia-derived neurotrophic factor (GDNF) family and the neurotrophin family (Sendtner et al., 2000). The family of neurotrophins is particularly interesting for the development and function of the nervous system. The members of this family interact predominantly with cells of the nervous system (Lewin and Barde, 1996). In addition to their survival-promoting properties, neurotrophic factors provide additional functions that have already been described. They support the survival, differentiation, synaptogenesis and

synaptic plasticity of developing neurons (Chao, 2003; Huang and Reichardt, 2001; Kaplan and Miller, 2000; Segal and Greenberg, 1996; Thoenen, 1995).

It has been suspected for a long time that dysregulated neurotrophic signals may contribute to the degeneration of motoneurons, for example in amyotrophic lateral sclerosis and spinal muscular atrophy.

1.3 The Motor System

The locomotor system of all higher organisms is a part of the CNS to control arbitrary movements and thus adapt to environmental conditions. The primary motor cortex is the highest level in the hierarchy of this very complex structured system. From layer V the axons pass the corticospinal tract through the capsula interna and thus form the connection between the cortex cerebri and the thalamus (Fig. 2) (Kandel et al., 2012). They cross the midbrain beyond the pons and pass at the base of the medulla oblongata to form a tract. This tract is called the pyramidal tract (Fig. 2) (Kandel et al., 2012). At the edge between medulla and spinal cord, the two pyramidal tracts cross and form the lateral corticospinal tract of the spinal cord, which ends in the dorsolateral region of the anterior horn (Fig. 2) (Kandel et al., 2012). Here, they transmit their information to the motoneurons or interneurons, which in turn innervate and control the distal muscles (Kandel et al., 2012).

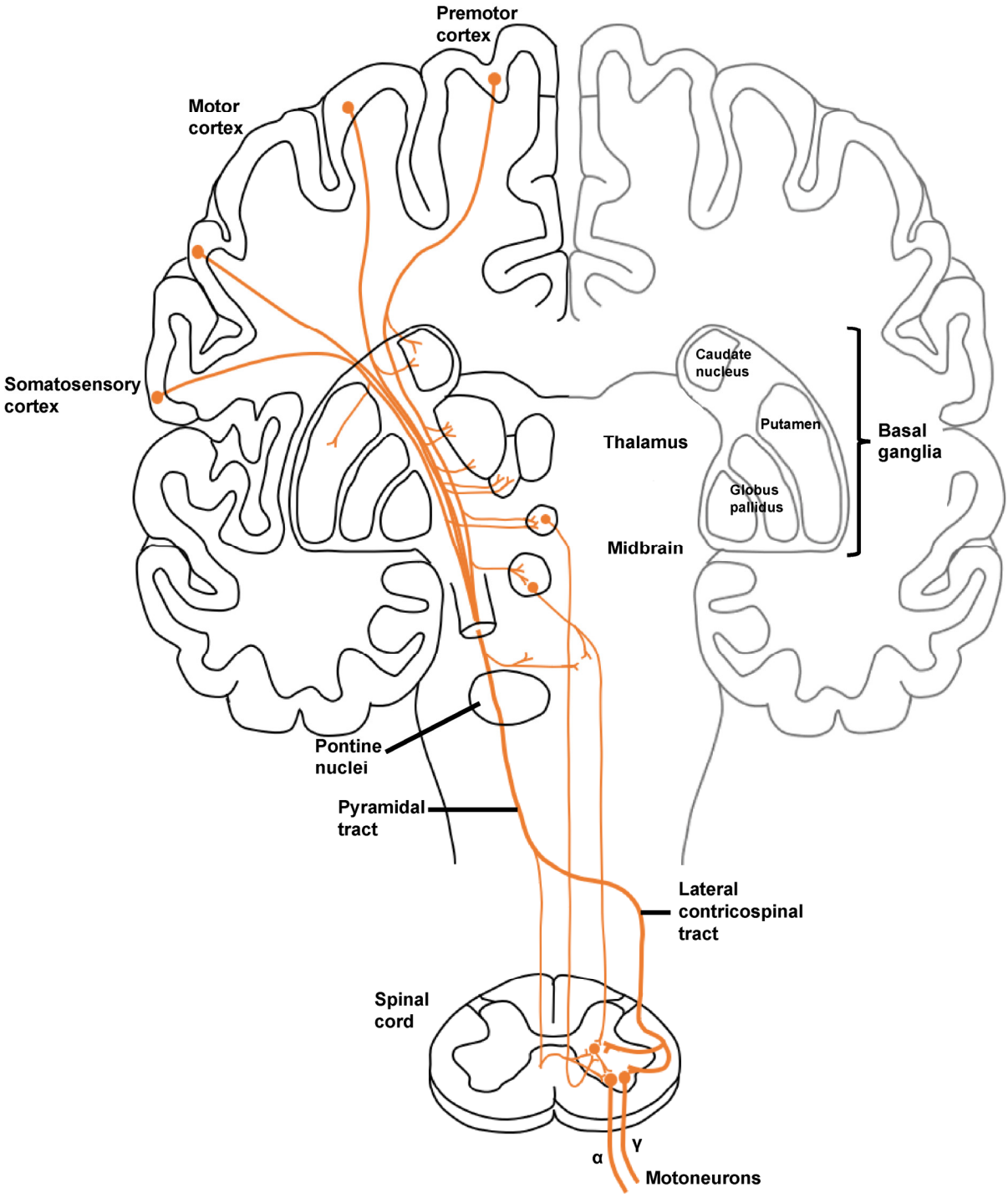

Figure 2 - The corticospinal tract mediates voluntary movement and forms the connection between the cortex cerebri and the spinal cord. This image illustrates the coordination of all involved components of the motor system. The corticospinal tract is shown in orange and ends in the dorsolateral region of the anterior horn of the spinal cord. Here the axons transmit their information to the motoneurons or interneurons that control contraction of the muscles. Modified according to (Kandel et al., 2012) (Figure 16-9, page 367).

1.3.1 The Motoneuron

In general, motoneurons are known as afferent cells that stimulate muscle fibers and thereby exercise direct or indirect muscle control (Buller et al., 1960). Like all neurons, motoneurons have a soma (cell body), an axon and dendrites (Kandel et al., 2012). The

dendrites serve mainly as perception or transmission of stimuli from adjacent nerve cells. On the axon hill, these nerve impulses are transmitted from the soma via the axon through the synapse to the periphery, for example to the muscle fibers (Kandel et al., 2012). Furthermore, a distinction can be made between myelinated and non-myelinated axons, which are responsible for the saltatory transmission of the nerve impulses and thus for the speed of transmission (Kandel et al., 2012). The myelin layer is basically formed by glial cells, whereas the oligodendrocytes in the CNS and the Schwann cells in the peripheral nervous system (PNS) perform this task (Kandel et al., 2012). By covering the axon with myelin, the transmission of nerve impulses is considerably faster, and saves energy and space compared to signal transmission by non-myelinated axons (Huxley and Stampfli, 1949). In addition, motoneurons can be classified as either somatic (innervate skeletal muscles) and visceral motoneurons (innervate smooth muscles) as well as lower (2nd motoneuron) and upper (1st motoneuron) motoneurons (Schmidt, 2001). The lower motoneurons, in turn, can also be divided into three subtypes: α-, β- and γ-motoneurons. β- and γ-motoneurons innervate the intrafusal muscle fibers or the intrafusal fibers within the muscle spindle (Burke et al., 1977), whereas the α-motoneurons represent the largest group and are responsible for the direct generation of muscle contractions and thus stimulate the extra-fusal skeletal muscle fibers. α-Motoneurons are highly differentiated, postmitotic and non-dividing cells. Neurotrophic factors are essential for development, maintenance and restoration after injury (Sendtner et al., 2000). α-Motoneurons and muscle fibers form the basic component of motor control - the motor unit (Kandel et al., 2012). The distal end of each motor axon, the presynaptic terminal, together with the postsynaptic muscle fiber forms a synaptic cleft. Such a synapse is called neuromuscular junction (NMJ).

1.3.2 Neuromuscular Junction (NMJ)

Neuromuscular junctions (NMJ) are the connections of motoneuron and the skeletal muscle fiber through a chemical synapse (Kandel et al., 2012; Tintignac et al., 2015). Its function is to transfer action potentials from the presynaptic membrane of the motoneuron to the postsynaptic muscle fibers to produce muscle contraction (Kandel et al., 2012; Tintignac et al., 2015). The dendrites and soma of the motoneurons are located in the spinal cord, while their axons are sent to the periphery to form a neuromuscular junction with skeletal muscle fibers (Kandel et al., 2012; Tintignac et al., 2015). The axons are surrounded by myelin sheaths formed by the Schwann cells (Kandel et al., 2012; Tintignac et al., 2015). The end of the axon is branched and forms the presynaptic nerve terminals, which are covered by terminal Schwann cells and kranocytes (Tintignac et al., 2015). The motor axon and the postsynaptic skeletal muscle fiber are highly specialized at the NMJ. In the active zone of presynaptic nerve terminals, a high number of mitochondria and acetylcholine (ACh)-filled

vesicles can be observed (Tintignac et al., 2015). The postsynapse is strongly folded and contains aggregates of acetylcholine receptors (AChRs) at the crest and a high concentration of voltage-gated sodium channels $Na_V1.4$ in the troughs of the folds (Tintignac et al., 2015). The specialized distribution of the receptors and the high concentration are necessary for efficient neuromuscular transmission. The pre- and postsynapse is separated by a narrow, 50- to 80-nm-wide gap called the synaptic cleft (Tintignac et al., 2015).

If the action potential reaches the presynapse, voltage-dependent calcium channels (P/Q type) open (Robitaille et al., 1993), calcium enters the presynapse and Ca^{2+} / calmodulin-dependent protein kinase II (CaM kinase) is activated by the increased intracellular calcium concentration (Mayford et al., 1996). The CaM kinase, in turn, phosphorylates synapsin I and thus removes the synaptic vesicles containing the neurotransmitter ACh from the actin cytoskeleton (Evergren et al., 2007). These vesicles are guided by Rap proteins under guanosine triphosphate (GTP) hydrolysis to the active zone of the presynapse (Leenders et al., 2001), where they fuse with the terminal membrane and release ACh into the synaptic cleft (Kandel et al., 2012). ACh binds to its AChRs of the postsynaptic muscle fiber, which is mainly permeable to sodium and potassium and to a lesser extent to calcium ions (Kandel et al., 2012; Tintignac et al., 2015). The net inward current of ACh per vesicle causes 3-4nA in the muscle fiber, the so-called quantal current or miniature endplate current (mEPC) (Tintignac et al., 2015). The simultaneous fusion of several vesicles causes an action potential and generates a current of several hundred nA at the NMJ (Tintignac et al., 2015). This event leads to a local depolarization of the muscle fiber by ~30-40mV, the so-called endplate potential (EPP) (Tintignac et al., 2015). This EPP is much higher than a postsynaptic action potential would require. This buffer is called the "safety factor" of neuromuscular transmission (Wood and Slater, 2001). In case of NMJ dysfunction, this can lead to severe limitations in mobility and breathing. Here, different components of the motor unit can be affected.

1.3.3 Disorders of the Motor Unit

The essential importance of the motor system becomes apparent when drastic and life-threatening diseases occur. Depending on the components of the motor unit, there are various diseases that can be distinguished.

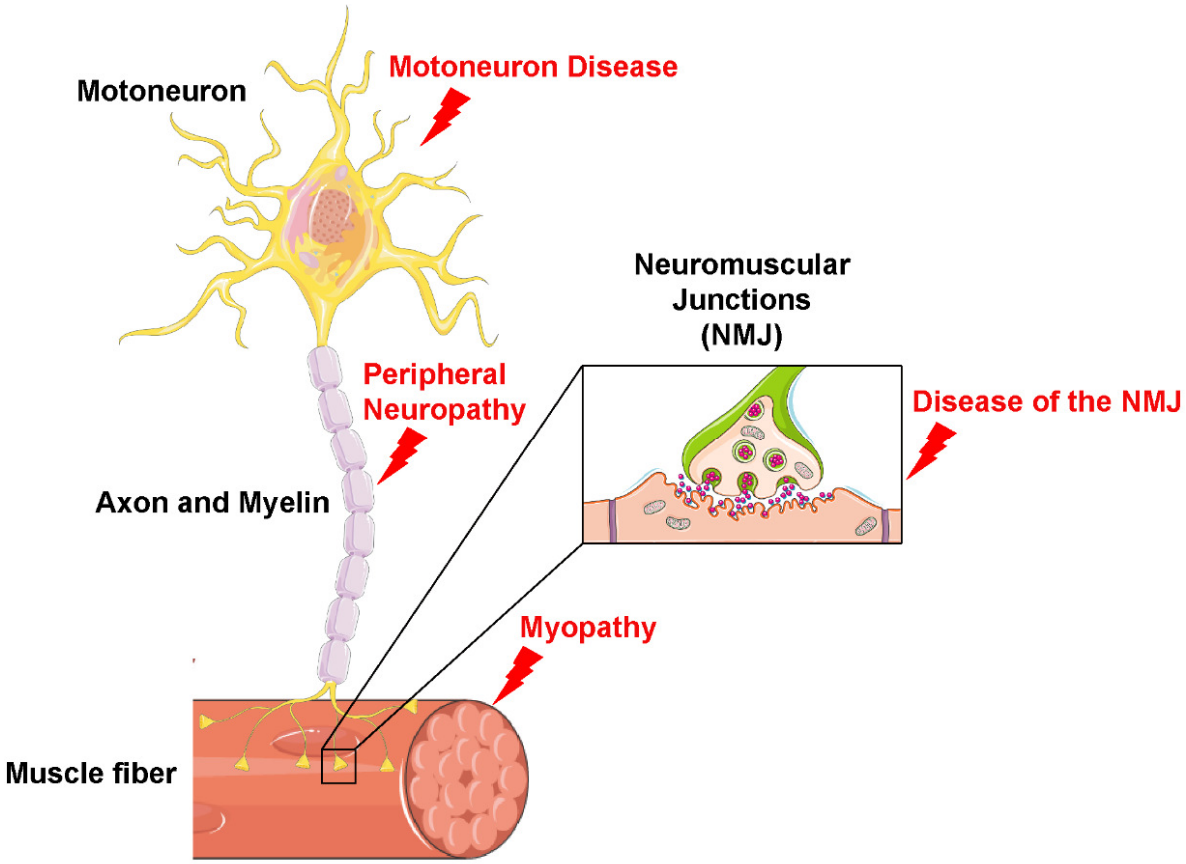

Figure 3 – Motor unit disorder. Graphical illustration of a motoneuron and its neuromuscular junctions (NMJ) at the innervated muscle fiber. Various diseases (highlighted in red) can be distinguished depending on the affected components of the motor unit. Designed with Servier Medical Art by Verena Surrey.

These distinguishing features vary depending on which functional component is affected. The following diseases can be distinguished (Fig. 3): (1) If motor neuron disease is present, the cell body of the motoneuron is usually affected, or death occurs through a dying back mechanism of axons, as can be observed in spinal muscular atrophy (SMA) (Cifuentes-Diaz et al., 2002). (2) If the corresponding axon or myelin sheath is affected, it is referred to as peripheral neuropathy. (3) A disease of the neuromuscular junctions (NMJs) is defined by disturbances of neuromuscular transmission between the motor axon and the muscle. (4) Furthermore, diseases can occur in the muscle fiber innervated by the motor neuron. Such a disease is called myopathy (Kandel et al., 2012).

Neuropathies and myopathies can also be distinguished differential-diagnostically. In a healthy and resting muscle with intact innervation, no activity outside the end-plate can normally be observed (Kandel et al., 2012). In the case of a neurogenic disease with a partially denervated and resting muscle, it is possible to measure spontaneous activities. In a chronic disease, the muscle innervated by a dying motoneuron atrophied, so that some muscle fibers disappear (Kandel et al., 2012). However, it can be observed that the axons of surviving motoneurons develop additional sprouts and re-innervate remaining muscle fibers in the environment. As a result, the muscle fibers are bundled according to their type and the

motor unit becomes larger. This process is called fiber-type grouping. In a myopathic disease with an atrophied and resting muscle with intact innervation, there is no activity or a changed number of motor units (Kandel et al., 2012).

Motoneuron diseases are classified according to the symptoms and the type of affected motoneurons (Donaghy, 1999). Various factors can cause this motoneuron disease such as genetic factors, excitotoxicity, chronic inflammation, aggregated proteins, oxidative stress, dysregulated RNA processing and signaling, impaired axonal transport and abnormal neurofilament accumulation (Bossy-Wetzel et al., 2004; Bruijn et al., 2004; Ferraiuolo et al., 2011). Amyotrophic lateral sclerosis (ALS) is the most common form of motoneuron disease. The variable phenotype is determined by the decline of the upper and lower motoneurons (Christensen et al., 1990; Ekestern, 2004; Kiernan et al., 2011) and depends on how severely the individual motoneuron types are affected. In general, involuntary fasciculations, muscle atrophies, and severe muscle spasms can lead to spastic contractions and obstacles to chewing, speaking, breathing and swallowing (Gubbay et al., 1985; Shaw, 2001).

The difference between ALS, in which both upper and lower motoneurons are affected and the autosomal recessive neurodegenerative disorder of spinal muscular atrophy (SMA) is that in the latter case only the lower motoneurons degenerate. Here, the symptoms and the course of the disease are also variable and varied, and lead to muscle atrophy which results in impaired mobility and, in the end-stage, respiratory failure (Crawford and Pardo, 1996; Korinthenberg et al., 1997; Lunn and Wang, 2008). This variable appearance of classical SMA makes it even more difficult to distinguish SMA from spinal muscular atrophy with respiratory distress type 1 (SMARD1).

1.4 Spinal Muscular Atrophy with Respiratory Distress Type I (SMARD1)

Spinal muscular atrophy with respiratory distress type 1 (SMARD1 or DSMA1) was first described in 1974. Two infants showed symptoms of a classic, proximal pronounced spinal muscular atrophy (SMA) in combination with a very early, severe respiratory distress (Mellins et al., 1974). By additional examinations of the children, the symptoms of the disease could be further distinguished from the more classic SMA symptoms. The respiratory distress occurring in the early stage of the disease could not be attributed to paralysis of the intercostal muscles, but to paralysis of the diaphragm (Bertini et al., 1989; Bove and Lannaccone, 1988; Gilmartin et al., 1977; Grohmann et al., 2003; McWilliam et al., 1985; Murphy et al., 1985; Novelli et al., 1995; Poets et al., 1990; Rudnik-Schoneborn et al., 1996; Schapira and Swash, 1985; Sivan and Galvis, 1990). Muscular atrophy also extends predominantly to the distal muscle regions (Rudnik-Schoneborn et al., 1996). This is an additional alteration to the proximal pronounced muscle weakness of the SMA disease.

Nevertheless, an accurate diagnosis is problematic because SMARD1 symptoms are very similar to SMA. A genetic comparison of these two diseases showed further differences. SMA patients suffer from mutations or deletions of the *survival motor neuron gene 1 (SMN1)*, whereas SMARD1 patients have recessive inherited mutations of the *immunoglobulin μ-binding protein 2 gene (IGHMBP2)* (Grohmann et al., 2001).

1.4.1 Clinical Phenotype of SMARD1

In 1974, Mellins et al. first described a variation of infantile SMA characterized by a pronounced diaphragmatic paresis with respiratory distress (Mellins et al., 1974). Several years later, in 1989, Bertini et al. also described this special form of proximal SMA (Bertini et al., 1989).

First phenotypical symptoms of SMARD1 are characterized by a sudden onset of respiratory distress within the first 13 months of life of the children due to the paralysis of the diaphragm in combination with the onset of distal muscle weakness. Due to the early onset of severe respiratory weakness, the children are usually artificially ventilated in the early stages of the disease. In the course of the disease, this distal muscle weakness spreads to the entire body and results in complete paralysis. Furthermore, intrauterine growth disorders, seizures and dysfunction of the autonomic nervous system (e.g. excessive sweating, cardiac arrhythmia, arterial hypertension, or bladder dysfunction) can also occur (Eckart et al., 2012; Giannini et al., 2006; Grohmann et al., 2001; Grohmann et al., 2003; Guenther et al., 2007; Kaindl et al., 2008; Mohan et al., 2001; Pitt et al., 2003; Rudnik-Schoneborn et al., 2004). Basically, two different SMARD1 types can be distinguished: (1) the infantile and rapidly appearing form, in which the paralysis of the diaphragm is diagnosed within the first 6 weeks to 6 months after birth and (2) the juvenile or slowly progressive form, in which the respiratory distress becomes apparent after several years (Guenther et al., 2007; Guenther et al., 2009b). This symptomatology clearly distinguishes the infantile form of SMARD1 from the classical SMA, since the phenotype occurs in the opposite order. Diaphragm palsy can be observed using differential-diagnostic x-rays by the passive displacement of the diaphragm into the thorax.

In addition, other classic symptoms can be described: paresis of the facial muscles and atrophy of the hand and foot muscles. As previously mentioned, muscle weakness starts in the distal parts of the body. Therefore, the infants show contractures on the fingers, deformed feet and bumps and are no longer able to move them against gravity (Grohmann et al., 2003).

Studies have already shown that muscle innervation is impaired by the death of myelinated axons of motor and sensory nerves. This leads to a high number of de-myelinated axons (Grohmann et al., 2003; Mohan et al., 2001; Wilmshurst et al., 2001).

A similarity to SMA was described by ultrastructural studies on mixed motor and sensory nerves, skeletal muscles, and NMJ since Wallerian degeneration and axonal atrophy were shown (Diers et al., 2005). In the later course of the disease, the sensory nervous system is also affected (Diers et al., 2005; Wilmshurst et al., 2001). The longest lifespan of a juvenile SMARD1 infant that is documented was 11 years (Giannini et al., 2006), in contrast, children with the infantile form of SMARD1 do not survive the first year of their life (Grohmann et al., 2003).

1.4.2 Genetic Background of SMARD1

The encoding Ighmbp2 gene is located on the medium-sized human chromosome 11 (11q13) (Grohmann et al., 2001), which carries a very high number of genes. Mutations in these coding genes are the origin of many diseases (Taylor et al., 2006). In 1996, 200 patients with an early onset SMA could be analyzed, of which 2 had diaphragm involvement and no mutations in survival motor neuron 1 (SMN1) gene on chromosome 5q (Porro et al., 2014; Rudnik-Schoneborn et al., 1996). Three years later, 9 additional cases of SMARD1 were described in three families with different geographical origins (Grohmann et al., 1999; Porro et al., 2014) showing the classical SMARD1 phenotype. Likewise, in these families no reference to the SMA locus on 5q or mutations within 1q- and 7p-loci could be found. 1q and 7p loci are the orthological regions corresponding to the murine *Pmn* gene region, which is also an established model of hereditary motor neuropathies. The genetic analysis of Lebanese and German families regarding diaphragmatic SMA revealed a participation of the region 11q13-q21. The first descriptions of *IGHMBP2* gene mutations in connection with SMARD1 disease were published in 2001 (Grohmann et al., 2001). Here, mutations in six different SMARD1 families were described and in the following years further mutations in the *IGHMBP2* gene were identified (AlSaman and Tomoum, 2010; Grohmann et al., 2003; Guenther et al., 2004; Wong et al., 2006). Various mutations of the gene are known, including frameshift deletions, missense, and nonsense mutations and splice donor mutations (Giannini et al., 2006; Grohmann et al., 2001; Guenther et al., 2009b; Maystadt et al., 2004).

The *IGHMBP2* gene consists of 15 exons and mutations could be described over all 15 exons of the gene. The most frequent regions are exon 10 and 12 (Grohmann et al., 2001; Jedrzejowska et al., 2014; Nomura et al., 2013; Novelli et al., 1995; Pitt et al., 2003). In general, the SMARD1 disease can be distinguished between an infantile and a juvenile form, depending on the temporal occurrence of respiratory weakness (Guenther et al., 2009b).

The functionality of the ATPase/helicase domain seems to play a crucial biochemical role, as the most mutations were found in this area of SMARD1 patients (Guenther et al., 2009b). If helicase activity is impaired, this could lead to disturbances in cellular processes

such as translation, splicing or mRNA processing. Further evidence of a key role in helicase activity is provided by mutations in the senataxin gene. The Ighmbp2 and senataxin proteins show a high homology and are structurally very similar. Missense mutations in the helicase domain of senataxin have been described, which leads to a motoneuron disorder such as the juvenile form of ALS (ALS4) (Chen et al., 2004).

1.4.3 The Helicase Immunoglobulin μ-Binding Protein 2 (Ighmbp2)

In principle, helicases are ubiquitous and highly conserved enzymes that remodel nucleic acids or nucleic acid-protein complexes by ATP hydrolysis and are classified into six superfamilies (SFs) according to their sequence, structure, and functionality. They have many functions in various areas of DNA and RNA metabolism. SF1 and SF2 consist of non-ring-forming helicases and contain all eukaryotic RNA and DNA helicases (Fairman-Williams et al., 2010; Jankowsky, 2011). These families use a highly conserved helicase core consisting of two tandem RecA-like domains. All SF1 and SF2 helicases are characterized by seven sequence motifs and all other motifs define the subfamilies (Gorbalenya et al., 1989; Jankowsky, 2011). The helicase Ighmbp2 belongs to SF1, which is divided into three subgroups - UvrD/Rep, the PIF1 and the UPF1-like helicases (Fairman-Williams et al., 2010). Due to its sequence, Ighmbp2 is classified into the group of UPF1-like helicases, which work on DNA and RNA (Guenther et al., 2009a; Jankowsky, 2011).

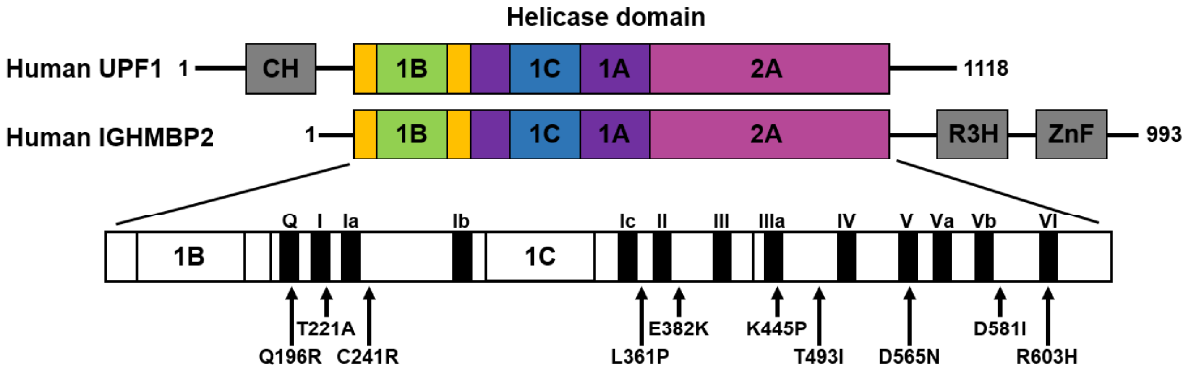

Figure 4 - Domain structure of the human IGHMBP2 protein. Shown are the motifs of the helicase domain, an R3H-type nucleic acid binding domain, and an AN1-type zinc finger motif. Helicase domain of UPF1 is very similar to IGHMBP2 containing two RecA-like helicase domains (1A and 2A) and two subdomains (1B and 1C). In the helicase core, all seven highly conserved sequence motifs of superfamily (SF) 1 and SF2 helicases (I, Ia, II, III, IV, V and VI) can be found. Modified according to (Lim et al., 2012).

IGHMBP2 is a multidomain protein consisting of 993 amino acids (Mizuta et al., 1993) and is composed of a DExxQ type helicase/ATPase domain, a R3H domain and a zinc finger domain (Fig. 4) (Guenther et al., 2009a; Lim et al., 2012). The helicase core of IGHMBP2 includes four domains: two RecA-like domains and two subdomains (Lim et al., 2012). IGHMBP2 as ATP-dependent 5'→3' helicase unwinds RNA and DNA duplices and is co-localized with ribosomal subunits such as the 40S, 60S, and 80S (Guenther et al., 2009a) and with tRNA or factors that are important for tRNA transcription and ribosome maturation

(de Planell-Saguer et al., 2009). Furthermore, Ighmbp2 is predominantly localized in the cytoplasm and axons of isolated motoneurons (Grohmann et al., 2004). It is therefore obvious that Ighmbp2 plays an important role in mRNA translation. Other members of SF1 helicases are described to be involved in different processes of RNA metabolism including transcription, splicing, translation and RNA decay (Jankowsky, 2011). Ighmbp2 has a very high structural similarity to UPF1 and 42% of its helicase domain is similar to Senataxin (Chen et al., 2004). However, the exact function of Ighmbp2 is unknown and its pathogenic role in SMARD1 is unclear.

1.4.4 *Nmd^{2J}* Mouse: Mouse Model for SMARD1

The neuromuscular disorder (*Nmd^{2J}*) mouse line with a spontaneous autosomal-recessive mutation in the *Ighmbp2* gene represents the mouse model for human SMARD1 disease and was first discovered and described in the Jackson Laboratories in 1995 (Cook et al., 1995). It has a point mutation in the fourth intron of the *nmd* gene on chromosome 19, which encodes Ighmbp2. A new splice donor site is induced at an A→G-transition leading to a truncated protein by alternatively spliced mRNA, a frameshift and a premature stop codon (Cox et al., 1998). As a result, the remaining level of functional Ighmbp2 in all tissues is reduced to 20%. The motoneuron disease of the *Nmd^{2J}* mice manifests itself through atrophy of the skeletal muscle and progressive paralysis and thus corresponds to the human phenotype of SMARD1 patients. The first symptoms are the muscle weakness in the hind limbs and the overall decrease in mobility, which can be observed at the age of two to three weeks (Cox et al., 1998). The body size of *Nmd^{2J}* mice is significantly smaller compared to heterozygous littermates. Nevertheless, the survival rate of these mice is very variable ranging from six to ten weeks up to eleven months (Cox et al., 1998; Shababi et al., 2016) and thus resembles SMARD1 patients with a milder course of the disease, which corresponds to the juvenile form of SMARD1 (Grohmann et al., 2004).

The α-motoneurons in the lumbar spinal cord of *Nmd^{2J}* (Ighmbp2-deficient) mice show a massive degeneration, which can already be measured before the first clinical symptoms occur (Grohmann et al., 2004). Postnatal day (P) 10 *Nmd^{2J}* mice already show a significant reduction of 63% of α-motoneurons compared to control mice. In the late stage of the disease, the number of motoneurons drops to 28% (Grohmann et al., 2004). In the early stages between P16 and P21 of the disease, morphologically intact NMJs and undisturbed innervation can be observed (Krieger et al., 2013), which speaks against a “dying back” pathomechanism. This is a clear alteration from classic spinal muscular atrophy (SMA), where the death of the motoneurons originates from the end plates. Furthermore, an increased sprouting of the nerve endings of the *Nmd^{2J}* motoneurons can be detected compared to wildtype controls (Krieger et al., 2013). Further studies have shown that

transgenic expression of wildtype Ighmbp2 cDNA in neurons can stop motoneuron degeneration, but these mice developed severe congestive heart failure due to dilated cardiomyopathy. Besides the motoneurons, this observation points to an important influence of Ighmbp2 on myocytes (Maddatu et al., 2004). When Ighmbp2 was expressed in both myocytes and motoneurons, these double-transgenic *Nmd*^{2J} mice showed a wildtype-like phenotype (Maddatu et al., 2005). However, if the Ighmbp2 level is ubiquitously upregulated using adenoviral gene transfer, this, in turn, leads to a more effective phenotypic rescue (Shababi et al., 2016).

Primary Ighmbp2-deficient motoneurons *in vitro* show a reduced growth cone size with a reduced amount of β-actin protein in combination with an enhanced axonal outgrowth cultured on a synapse-specific laminin-211/221 (Krieger et al., 2014b). However, the survival of Ighmbp2-deficient motoneurons shows no deficits, which in turn indicates other non-cellular autonomous mechanisms. In the blood serum of *Nmd*^{2J} mice a reduction of insulin growth factor 1 (Igf1) can be observed, which can be rescued by external application of polyethylene glycol-coupled (PEG)-IGF1. Thus, motoneuron death cannot be prevented, but the *Nmd*^{2J} mice show increased survival through increased muscles strength (Krieger et al., 2014a; Krieger et al., 2014b).

1.5 Actin Cytoskeleton

Actins in combination with the microtubules and intermediate filaments form the eukaryotic cytoskeleton and have an essential effect on cellular processes and functions. They are distributed throughout the neuron and are found especially in the neurites. The actins form polymers in the shape of a strand and two thin strands wound around each other forming the microfilaments. These microfilaments are constantly built up and disassembled in order to react to extrinsic and intrinsic signals in a dynamic way. This process is controlled by the neuron itself (Kandel et al., 2012). The monomeric, globular G-actins spontaneously polymerize to filamentous F-actins, which are highly dynamic structures (Pollard and Cooper, 2009). Six different actin isoforms can be observed in mammals, encoded by different genes. $\alpha_{cardiac}$-, $\alpha_{skeletal}$-, α_{smooth}- and γ_{smooth}-actin are predominantly found in striated and smooth muscles, while β_{cyto}- and γ_{cyto}-actin are expressed ubiquitously in all cell types. Actin isoforms are 93% similar in identity (Perrin and Ervasti, 2010).

The actin cytoskeleton plays a crucial role in the morphological development of neurons and in the maintenance and structural alteration of adult neurons (Luo, 2002) including axon initiation, growth, guidance, branching, synapse formation as well as stability and is part of the axon initial segment (AIS) (Xu et al., 2013). Impairment of F-actin interferes with the diffusion barrier at AIS, leading to mislocalization of somatodendritic proteins in the

axonal compartment (Song et al., 2009). Actin-microtubule interaction contributes to growth cone extension and axonal growth (Suter and Miller, 2011). Actins are abundantly represented in membrane protrusions, whereby two types of protrusions have to be distinguished: First the filopodia, which have unbranched bundled actin filaments, and second lamellipodia, which have a network of branched actin filaments (Kalil and Dent, 2014).

1.6 Fibroblast Growth Factor Receptor 1 (FGFR1)

The fibroblast growth factor receptors (FGFRs) belong to a superfamily of tyrosine kinase receptors and persist about 800 amino acids (Ornitz and Itoh, 2015). Four different FGFRs are known consisting of an extracellular ligand binding domain, three immunoglobulin-like domains (I-III), a transmembrane domain and a split intracellular tyrosine kinase domain. The latter domains are functionally dimerized upon activation (Chen et al., 2008; Furdui et al., 2006). With the help of 18 different fibroblast growth factors (FGFs), FGFRs can be activated by binding to the extracellular domain of FGFR (Ornitz and Itoh, 2015). FGF-2, also known as bFGF, is a paracrine growth factor that binds to and activates FGFR1 (Ibrahimi et al., 2004). Originally, bFGF was isolated from the brain and pituitary gland as a mitogen for cultured fibroblasts (Gospodarowicz et al., 1975; Gospodarowicz et al., 1978).

The activation of FGFRs by FGF binding depends on cofactors such as heparin, heparan sulfate and klotho (Schlessinger et al., 2000; Suzuki et al., 2008) and results in dimerization, which activates tyrosine kinase and starts several signaling pathways. The following signaling pathways are activated: STAT signaling PI3K/AKT and RAS/RAF/MEK/MAPK signaling (Ornitz and Itoh, 2015).

In general, the FGFRs activated signaling pathways control growth, survival, and differentiation of precursor cells in organogenesis (Borello et al., 2008; Kong et al., 2014; Potthoff et al., 2012; Vincentz et al., 2005). In addition, the specific expression of FGFs is crucial for neurogenesis, as they influence neuronal differentiation (Borello et al., 2008).

It should be noted that FGFRs are involved in many diseases such as Kallmann syndrome (Albuisson et al., 2005; Gill et al., 2004) and several cancers (Acevedo et al., 2007; Ugolini et al., 1999; Wang et al., 2018).

1.7 Insulin-like Growth Factor-2 mRNA Binding Protein 1 (IMP1)

Insulin-like growth factor-2 mRNA binding protein 1 (IMP1) is an RNA binding protein consisting of six RNA binding sites, two RNA recognition motifs and four hnRNP-K homology (KH) domains (Nielsen et al., 1999; Ross et al., 1997; Yisraeli, 2005). RNA binding to the

domains described above influences the stability of RNA, its transport and the translational control of the transcript (Huttelmaier et al., 2005; Leeds et al., 1997; Leung et al., 2006).

High expression of Imp1 during embryonic stages plays a crucial role in the development of the nervous system (Hansen et al., 2004; Nishino et al., 2013). Imp1-deficient mice develop a small cerebral cortex and show a general impairment of embryonic development (Nishino et al., 2013). Previous studies have shown that the interaction of Imp1 with β-actin mRNA regulates growth cone guidance, axonal remodeling and dendritic morphology (Eom et al., 2003; Medioni et al., 2014; Sasaki et al., 2010). RNA looping mediates protein-mRNA interaction, which in turn is predominantly regulated by IMP1 concentration (Nicastro et al., 2017) and β-actin mRNA is released after phosphorylation of IMP1 protein (Ceci et al., 2012; Huttelmaier et al., 2005; Urbanska et al., 2017).

1.8 Objective

This Ph.D. thesis addresses a morphological and functional analysis of primary Ighmbp2-deficient (Ighmbp2-def.) *Nmd*^{2J} motoneurons compared to wildtype (Ighmbp2$^{+/+}$) motoneurons. The investigation can be divided into five main parts. The first part focuses on the production and validation of the self-made polyclonal rabbit anti Ighmbp2 antibody. The second part is concerned with a morphological and functional analysis of Ighmbp2-deficient and Ighmbp2$^{+/+}$ motoneurons regarding axonal outgrowth, branching behavior, spontaneous Calcium (Ca^{2+}) transients at the distal axon, growth cone size and signal intensity of β-actin in the growth cones, compartment-specific local translation of β-actin protein, general translational effects, and analyses of distribution and amount of actin isoform mRNAs and proteins. The third part comprises of the analysis whether Ighmbp2 influences translation caused by RNA binding. Furthermore, the fourth part deals with Insulin-like growth factor-2 mRNA- binding protein 1 (Imp1) and fibroblast growth factor receptor 1 (Fgfr1) as affected targets in primary Ighmbp2-deficient motoneurons. Finally, the fifth part is targeted at possible protein interaction partners of Ighmbp2 using immunocytochemical staining (ICC) and Co-immunoprecipitation (Co-IP).

2. Materials

2.1 Manufacturers

Table 1 - List of Manufacturers

Manufacturer	Location
Adobe	San José, CA, USA
AGFA	Mortsel, Belgium
Ambion	Waltham, MA, USA
Amersham Bioscience	Freiburg, Germany
Antikörper-Online	Aachen, Germany
AppliChem	Darmstadt, Germany
BD Bioscience	Heidelberg, Germany
Bemis	Neenah, WI, USA
Binder	Tuttlingen, Germany
Biometra	Göttingen, Germany
Bio-Rad	München, Germany
Biozym Scientific	Ohlendorf, Germany
Brand	Wertheim, Germany
Carl Roth GmbH	Karlsruhe, Germany
Carl Zeiss AG	Oberkochen, Germany
cp-Pharma	Burgdorf, Germany
Dianova	Hamburg, Germany
Dumont	Montignez, Switzerland
Elma	Singen, Germany
Endnote	Philadelphia, PA, USA
Eppendorf AG	Hamburg, Germany
Eurofins Scientific	Luxembourg, Luxemburg
Exiquon	Vedbaek, Denmark
Fresenius Kabi	Bad Homburg vor der Höhe, Germany
GE Health Care Life Sciences	Freiburg, Germany
GeneOn	Ludwigshafen, Germany
Gibco	Karlsruhe, Germany
Gilson	Middleton, WI, USA
GLW	Würzburg, Germany
GraphPad Software, Inc.	La Jolla, CA, USA
Greiner Bio One	Frickenhausen, Germany
Hartenstein	Würzburg, Germany

Hartmann	Heidenheim
Hartmann Analytic GmbH	Braunschweig, Germany
Heraeus Instruments	Langenselbold, Germany
Hettich	Tuttlingen, Germany
Hoffmann La-Roche	Basel, Switzerland
Holten	Allerød, Dänemark
Ibidi	Martinsried, Germany
Intas Science Imaging	Göttingen, Germany
Invitrogen	Karlsruhe, Germany
Kern PCB	Balingen, Germany
Keyence	Osaka, Japan
KNF Neuberger	Freiburg im Breisgau, Germany
Leica Microsystems	Wetzlar, Germany
Lexogen	Vienna, Austria
LG electronics	Seoul, South Korea
LI-COR Bioscience	Lincoln, NE, USA
Linaris	Mannheim, Germany
Macherey und Nagel	Düren, Germany
Memmert	Schwabach, Germany
Merck Millipore	Billerica, MA, USA
Microsoft	Redmond, WA, USA
Mirus	Köln, Germany
Neolab	Heidelberg, Germany
Nikon	Tokio, Japan
Olympus	Tokyo, Japan
Peprotech	Rocky Hill, NJ, USA
Peqlab Biotech. Gmbh	Erlangen, Germany
Pfizer	Berlin, Germany
Philips	Amsterdam, Nederland
Polysciences	Warrington, PA, USA
Promega	Maddison, WI, USA
Qiagen	Hilden, Germany
Qimaging	Surrey, BC, Canada
R. Langenbrinck	Emmendingen, Germany
Roche Diagnostics	Rotkreuz, Switzerland
Sarstedt AG and Co.	Nümbrecht, Germany
SchuettPhoenix	Dublin, Irland

Schülke	Zürich, Switzerland
Scotsman	Berlin, Germany
SensiCare Ice	Kleve, Germany
Sigma-Aldrich GmbH	München, Germany
StarLab	Hamburg, Germany
System Bioscience	Palo Alto, CA, USA
Th. Geyer	Renningen, Germany
Thermo Fisher Scientific	Waltham, MA, USA
VWR Int.	Darmstadt, Germany
Wayne Rasband (NIH)	Bethesda, MD, USA
Worthington	Lakewood, NJ, USA
ZVG	Troisdorf, Germany

2.2 Appliances

Table 2 - List of Appliances

Appliance	Manufacturer
Accujet pro	Brand
Centrifuge	
5417R	Eppendorf AG
5415D	Eppendorf AG
5804R	Eppendorf AG
Mini Spin	Eppendorf AG
Mini Centrifuge MC-6400	Hartenstein
Rotofix 32A	Hettich
Clean Bench	
Hera Safe (HS 18/2)	Heraeus Instruments
LaminAir (HV PCR)	Holten
Confocal Laser Scanning Microscope	
Olympus Fluo View FV1000 (IX81)	Olympus
Olympus BX51WI with	Olympus
40x Objective LUMPlanFI/IR and	Olympus
Rolera-XR	Qimaging
Cunx60 developer	AGFA
Fluorescence microscope	
Biozero (BZ8000K)	Keyence
Leitz DMRBE	Leica Microsystems

Gel chamber (Mini Protean Tetra Cell)	Bio-Rad
Gas jet	SchuettPhoenix
Heating block	
Thermomixer comfort (1.5 ml/2 ml)	Eppendorf AG
Ice machine	Scotsman
Incubator	
BD23 E2	Binder
CB210 E3	Binder
Light Cycler	
Light Cycler 1.5	Roche Diagnostics
Light Cycler 96	Roche Diagnostics
Light optical microscope	
Nikon Eclipse TS100 with	Nikon
Philips Projection lamp (5761)	Philips
Microwave	LG electronics
Nanodrop 1000 Spectrophotometer	Peqlab Biotech. GmbH
Neubauer Cell Counter Chamber	Brand, Wertheim
PCR Cycler Mastercycler Nexus X2 flexlid	Eppendorf AG
Photometer	Eppendorf AG
Pipettes	
Pipetman (20 µl, 200 µl, 1000 µl)	Gilson
ErgoOne (2.5 µl, 10 µl, 20 µl, 200 µl, 1000 µl)	StarLab
Power Supply	
Power Pack HC	Bio-Rad
Power Pack P25 T	Biometra
Scale	Kern PCB
Stereo Microscope	
Leica S8AP0 with Leica L2	Leica Microsystems
Zeiss Stemi 2000 with KL200LED	Carl Zeiss AG
Suction pump	Neolab
UV transluminator	Peqlab Biotech. GmbH
Ultrasonic bath	Elma
Vacuum pump	
ECOM-P 4153	Eppendorf AG
N010 KN-18	KNF Neuberger
Vortex Mixer GLW L46	GLW
Water Bath	Memmert

2.3 Consumables

Table 3 - List of Consumables

Consumable	Manufacturer
µ-dish$^{35mm, high}$ glass bottom	Ibidi
4-12% NuPAGE Bis-Tris gel	Bio-Rag
Capillaries	Roche
Cell Culture Well Plates (12 Well, 24 Well)	Sarstedt
Cellstar 4-Wells	Greiner BioOne
Centricon	Millipore
Centrifugation tube (15 ml, 50 ml)	Greiner BioOne
Cuvettes	Hartenstein
Filter Paper (Mini Trans-Blot)	Bio-Rad
Filter Tips	Sarstedt
Forceps, Dumoxel n°5	Dumont
Glass Capillaries	Roche Diagnostics
Glass Pasteur Pipettes	Hartenstein
Glasspipetts 5ml, 10ml, 25ml, 50ml	Hartenstein
Gloves	SensiCare Ice
Glutathione sepharose transferase beads	Amersham Bioscience
LightCycler 8-Tubes Stripes (white)	Roche
Microscope cover glasses (Ø 10 mm)	Hartenstein
Microscope slides (ca. 76x26 mm)	R. Langenbrinck
Mini Trans Blot Cell	Bio-Rad
Ni-NTA agarose beads	Qiagen
Nunc Cryotubes	Thermo Scientific
Parafilm	Bemis
PCR tubes	Sarstedt
Peha Soft nitrile gloves	Hartmann
Petri dishes (6 cm, 8 cm, 15 cm)	Greiner BioOne
Pipette Tips	Sarstedt
Precast Protein Gel (4-20% gradient Mini-Protean polyacrylamide gel)	Bio-Rad
PVDF membrane (Immun Blot)	Bio-Rad
Reaction tubes (1.5 ml, 2 ml)	Sarstedt
T75 cell culture flask	Sarstedt
Terralin	Schülke
X-ray films (Fujifilm Super RX)	Hartenstein

ZetMedica Laboratory and hygiene tissue	ZVG, Troisdorf

2.4 Chemicals

Table 4 - List of Chemicals

Chemical	Manufacturer
16% formaldehyde solution	Sigma -Aldrich
20xSSC	Ambion
Agarose	Biozym Scientific
Acrylamid 40%	Biorad
Ampuwa	Fresenius Kabi
Aqua Poly/Mount	Polysciences
Bacto-tryptone	BD Bioscience
Bacto-yeast extract	BD Bioscience
Betaine monohydrate	Sigma -Aldrich
Boric acid	Sigma -Aldrich
Bromophenol blue	Sigma -Aldrich
Chelex	Bio-Rad
Chloramphenicol	Sigma -Aldrich
$CuSO_4$	Sigma -Aldrich
Dimethyl-Pimelimidate (DMP)	Sigma -Aldrich
Disodium phosphate (Na_2HPO_4)	Sigma -Aldrich
Disodium tetraborate	Sigma -Aldrich
DNA ladder (GeneRuler)	Thermo Fisher Scientific
Dynabeads Protein A	Thermo Fisher Scientific
EDTA (Ethylenediaminetetraacetic acid)	Sigma -Aldrich
Ethanol	Sigma -Aldrich
Ethanolamine	Sigma -Aldrich
Formaldehyde solution (16%)	Thermo Fisher Scientific
Glucose	Sigma -Aldrich
Glycerol	Sigma -Aldrich
HEPES	Sigma -Aldrich
Hybridisation solution	Sigma -Aldrich
Igepal CA-630	Sigma
Immersion Oil (Immoil F30CC)	Olympus
Isopropyl-β-D-thiogalactopyranoside (IPTG)	Sigma -Aldrich

K_2HPO_4	Sigma -Aldrich
Ketavet	Pfizer
KH_2PO_4	Sigma -Aldrich
Methanol	Th. Geyer
Midori Green	Intas Science Imaging
Monopotassium phosphate (KH_2PO_4)	Sigma -Aldrich
Monosodium diphosphate (NaH_2PO_4)	Sigma -Aldrich
Paraformaldehyde (pH 7.6)	Merck Millipore
Poly-DL-ornithine-hydrobromide (PORN-H 100x)	Sigma -Aldrich
Potassium chloride	Sigma -Aldrich
Powdered Milk	Carl Roth
Protein Ladder	Thermo Fisher Scientific
RIPA buffer	Sigma -Aldrich
Saline sodium citrate	Thermo Fisher Scientific
Salmon Sperm DNA Sodium Salt	AppliChem
Sarkosyl (N-Lauroylsarcosine)	Sigma -Aldrich
Sodium acetate	Sigma -Aldrich
Sodium chloride	Sigma -Aldrich
Sodium dodecyl sulfate	AppliChem
Sodium metaperiodate	Sigma -Aldrich
Tango Buffer (10x)	Thermo Fisher Scientific
TBTA	Sigma
TCEP	Sigma
Terralin	Schülke
Tris base	Sigma -Aldrich
Triton X100	Sigma -Aldrich
Tween 20	Sigma -Aldrich
Xylavet	cp-Pharma
β-Mercaptoethanol	Carl Roth
γ-^{32}P-ATP	Hartmann Analytic GmbH

2.5 Media, Supplements and Enzymes

Table 5 – List of Media, Supplements and Enzymes

Media, Supplements and Enzymes	Manufacturer
Ampicillin	Sigma -Aldrich
Anisomycin	Sigma -Aldrich
Arginine	Sigma
B27 Supplement	Thermo Fisher Scientific
BamII	Thermo Fisher Scientific
bFGF (murine)	Peprotech
Bovine Serum Albumin/BSA	Sigma
Brain-derived neurotrophic factor (BDNF)	Affinity Purification
Ciliary neurotrophic factor (CNTF)	Affinity Purification
Dulbecco´s Modified Eagle Medium (DMEM)	Gibco
DMEM, methionine-free	Gibco
DMSO	Sigma
EcoRI	Thermo Fisher Scientific
Fetal Calf Serum/FCS	Linaris
Geneticin	Thermo Fisher Scientific
GlutaMAX Supplement (100x)	Thermo Fisher Scientific
GoTaq G2 Hot Start Green Master Mix	Promega
Hank's Balanced Salt Solution (HBSS)	Gibco
Horse Serum	Gibco
Horse Serum, dialyzed	Gibco
HpyF3I DdeI (10 U/µl)	Thermo Fisher Scientific
Laminin-111	Invitrogen
Laminin-211/221	Millipore
L-azidohomoalanine (AHA)	Thermo Fisher Scientific
Lipofectamine 2000	Invitrogen
Lysin	Sigma
Neurobasal	Gibco
Neurobasal, amino acid-free	Gibco
NuPAGE MOPS SDS Running Buffer	Invitrogen
Opti-MEM	Gibco
Oregon Green 488 BAPTA-1, AM-Ester (OGB)	Thermo Fisher Scientific
Penicillin/Streptomycin (P/S)	Thermo Scientific
Phosphatase Inhibitor „PhosSTOP“	Roche

Pluronic F-27	Thermo Fisher Scientific
Proline	Sigma
Protease Inhibitor cOmplete mini	Roche
Proteinase K	Roche
RIPA buffer	Sigma
RNasin RNase Inhibitor	Promega
T4 ligase	Thermo Fisher Scientific
Trans-IT	Mirus
Trypsin	Worthington
Trypsin-Inhibitor	Sigma -Aldrich
T-DNAse	Invitrogen

2.6 Kits and Detection Systems

Table 6 – List of Kits and Detection Systems

Kit or Detection System	Manufacturer
Amersham ECL Normal/ Prime/ Select Western Blotting Detection Reagent	GE Health Care Life Sciences
C2 Mouse Growth Factor Antibody Array	Antikörper-Online
Luminaris HiGreen qPCR Master Mix	Thermo Fisher Scientific
mRNA-Seq Library Prep Kit V2	Lexogen
NucleoBond Xtra Midi/Maxi EF	Machery und Nagel
NucleoSpin RNA Kit	Machery und Nagel
Pierce BCA Protein Assay Kit	Thermo Fisher Scientific
Plasmid mini-prep kit	Machery und Nagel
QIAEX II – Gel Extraction Kit	Qiagen
SuperScript III Kit	Invitrogen
TOPO TA cloning kit	Invitrogen
TRIzol Reagent	Ambion
TURBO DNA-*free* Kit	Invitrogen

2.7 Primary Antibodies

Table 7 – List of Primary Antibodies

Antigen	Host	Clonality	Manufacturer	Dilution	Experiment
Ago2	rat	polyclonal	Self-made, Lab Gunter Meister	1:10	WB
Calnexin	goat	polyclonal	Acris	1:1000	WB
CPSF73	rabbit	polyclonal	Bethyl	1:1000	WB
Digoxigenin	mouse (IgG_1)	monoclonal	Abcam	1:1000	ISH
FGFR-1	mouse	monoclonal	Novus Biologicals	1:200	ICC
				1:500	WB
GFP	chicken	polyclonal	Abcam	1:2000	ICC
GluTub	mouse (IgG)	monoclonal	Synaptic system	1:1000	ICC
Histone H3	rabbit	polyclonal	Abcam	1:3000	WB
hnRNPR	rabbit	polyclonal	Abcam	1:2000	WB
Ighmbp2	rabbit	polyclonal	Affinity Purification	1:2000	ICC
IMP1	rabbit	polyclonal	Cell Signaling	1:1000	WB
LSM4	chicken	polyclonal	Sigma	1:10000	WB
Map-2	mouse	monoclonal	Sigma-Aldrich	1:1000	ICC
Mov10	rabbit	polyclonal	Bethyl	1:1000	WB
p75	mouse	monoclonal	Biosensis	1:10000	Cell culture (panning-plate)
Puromycin	mouse	monoclonal	Millipore	1:5000	WB
Sars2	rabbit	polyclonal	GeneTex	1:1000	WB
SMN	mouse	monoclonal	BD Biosciences	1:1000	WB
Tau	rabbit	polyclonal	Sigma-Aldrich	1:800	ICC
TDP43	rabbit	polyclonal	Proteintech	1:1500	WB
Top1	rabbit	polyclonal	GeneTex	1:500	WB
UPF1	rabbit	polyclonal	Abcam	1:10000	WB
α-actin	mouse (IgM)	monoclonal	Invitrogen	1:500	ICC
α-Tubulin	mouse	monoclonal	Sigma	1:3000	WB
β-actin	mouse (IgG)	monoclonal	GeneTex	1:1000	ICC
βIII Tubulin	mouse	monoclonal	Sigma-Aldrich	1:500	ICC
				1:4000	WB

2.8 Secondary Antibodies

Table 8 – List of Secondary Antibodies

Antigen	Host	Clonality	Manufacturer	Dilution	Experiment
Alexa488 α mouse IgM	goat	polyclonal	Invitrogen	1:1000	ICC
Alexa488 α mouse IgG	goat	polyclonal	Invitrogen	1:800	ICC
				1:1000	ISH
Alexa488 α chicken	goat	polyclonal	Invitrogen	1:800	ICC
Cy3 α mouse IgG	goat	polyclonal	Jackson	1:300	ICC
Cy3 α rabbit	donkey	polyclonal	Jackson	1:600	ICC
Cy5 α rabbit	donkey	polyclonal	Jackson	1:800	ICC
HRP α mouse	goat	polyclonal	Jackson	1:10000	WB
HRP α rabbit	goat	polyclonal	Jackson	1:10000	WB
HRP α goat	donkey	polyclonal	Jackson	1:10000	WB
HRP α rat	goat	polyclonal	Jackson	1:10000	WB
HRP α chicken	rabbit	polyclonal	Jackson	1:10000	WB

2.9 LNA mRNA Detection-probes for FISH

Table 9 – List of LNA mRNA Detection-probes for FISH

Target mRNA	Sequence 5'-3'	Manufacturer
Actα1	/5DigN/AGTCAATCTATGTACACGTCAA/3Dig_N/	Exiquon
Actβ	/5DigN/ACGCGACCATCCTCCTCTTA/3Dig_N/	Exiquon
Actγ1	/5DigN/AGTGACCGAGCCACATGAACT/3Dig_N/	Exiquon

2.10 Primer Sequences and Program settings for genotyping

Table 10 – List of Primer Sequences for genotyping

Target		Primer Sequence	Manufacturer
Nmd^{2J}	forward	5' TCA CAG AGC ACT GAT GAC AC 3'	Eurofins Scientific
	reverse	5' TCT CTC TCT CAC ACA CAC ACA 3'	Eurofins Scientific

2.11 Bacterial Cell Lines

Table 11 - List of Bacterial Cell Lines

Bacterial Cell Lines	Manufacturer/Source
E. coli Top10	Thermo Fisher Scientific
E. coli Rosetta DE3 pLys	Thermo Fisher Scientific

2.12 Plasmid vectors

Table 12 – List of Plasmid Vectors

Plasmid vectors	Inserts with N/C terminal	Manufacturer/Source
pGex6p1	GST-IGHMBP2-6xHis	Amersham Bioscience
pSIH1-H1-Puro shRNA	sh RNA targeting Ighmbp2	System Bioscience
FU-Valentine ubiquitin promotor	LCK-Myr-eGFP+3'UTR β-actin	(Rathod et al., 2012)
pCMV-VSVG	Lentiviral packaging helper	(Dull et al., 1998;
pCMVΔR8.91	plasmids	Zufferey et al., 1998)

2.13 Primer Sequences and Program settings for quantitative RT-PCR

Table 13 – List of Primer Sequences for qRT-PCR

Target mRNA		Primer Sequence
Gapdh, murine	forward	5' AAC TCC CAC TCT TCC ACC TTC 3'
	reverse	5' GGT CCA GGG TTT CTT ACT CCT T 3'
α-actin, murine	forward	5' TAG ACA CCA TGT GCG ACG AAG A 3'
	reverse	5' ACC TAC CAT GAC ACC CTG GTG A 3'
β-actin, murine	forward	5' GAT GAC CCA GAT CAT GTT T 3'
	reverse	5' CGT GAG GGA GAG CAT AG 3'
Ighmbp2, murine	forward	5' AGC ACT GAT GAC ACT GAA GAA G 3'
	reverse	5' GCC TTG CTT CAC AGC TTG AAG G 3'
Imp1, murine	forward	5' CTC CAT CAA GAT TGC ACC AC 3'
	reverse	5' CTT TAC TTC CTC CTT GGG AC 3'
Fgfr1, murine	forward	5' GAG CGA TGT GTG GTC TTT TG 3'
	reverse	5' CTG GGC TTG TCC ATT CGA TG 3'
GAPDH, human	forward	5' GCA AAT TCC ATG GCA CC 3'
	reverse	5' CGC CAG TGG ACT CCA CGA C 3'
β-Actin, human	forward	5' CGA AAC TAC CTT CAA CTC CAT CAT G 3'
	reverse	5' GCA ATG ATC TTG ATC TTC ATT GTG 3'

IMP1, human	forward	5’ CAT CAC TCT GGT GGG TGT AGA TC 3’
	reverse	5’ CAG CTG CCG TCA AAT TCT GC 3’
FGFR1, human	forward	5’ CTC CAA GAA GTG CAT ACA CCG AG 3’
	reverse	5’ CAT CAC TCT GGT GGG TGT AGA TC 3’

Table 14 – qRT-PCR Cycle Program for mouse *Gapdh* mRNA

***Gapdh*, murine**	**Denaturation 1 Cycle**		**Amplification 40 Cycles**				**Melting Curve 1 Cycle**			**Cooling 1 Cycle**
Target Temperature	50	95	95	59	72	78	95	65	95	40
Incubation Time	2	10	15	30	30	5	0	15	0	40
Temp. Trans. Rate	20	20	20	20	20	20	20	20	0.1	20
2nd Target Temp.	0	0	0	0	0	0	0	0	0	0
Step Size	0	0	0	0	0	0	0	0	0	0
Step Delay (Cycles)	0	0	0	0	0	0	0	0	0	0
Acquisition Mode	None	None	None	None	None	None	None	None	Cont.	None
Analysis Mode	Quantification		Quantification				Melting Curve			None

Temp. = Temperature; Trans. = Transition; Cont. = continuous

Table 15 – qRT-PCR Cycle Program for mouse *α-actin* mRNA

***α-actin*, murine**	**Denaturation 1 Cycle**		**Amplification 50 Cycles**				**Melting Curve 1 Cycle**			**Cooling 1 Cycle**
Target Temperature	50	95	95	63	72	84	95	65	95	40
Incubation Time	2	10	15	30	30	5	0	15	0	40
Temp. Trans. Rate	20	20	20	20	20	20	20	20	0.1	20
2nd Target Temp.	0	0	0	0	0	0	0	0	0	0
Step Size	0	0	0	0	0	0	0	0	0	0
Step Delay (Cycles)	0	0	0	0	0	0	0	0	0	0
Acquisition Mode	None	None	None	None	None	None	None	None	Cont.	None
Analysis Mode	Quantification		Quantification				Melting Curve			None

Temp. = Temperature; Trans. = Transition; Cont. = continuous

Table 16 – qRT-PCR Cycle Program for mouse *β-actin* mRNA

***β-actin*, murine**	**Denaturation 1 Cycle**		**Amplification 50 Cycles**				**Melting Curve 1 Cycle**			**Cooling 1 Cycle**
Target Temperature	50	95	95	59	72	83	95	65	95	40
Incubation Time	2	10	15	30	30	5	0	15	0	40
Temp. Trans. Rate	20	20	20	20	20	20	20	20	0.1	20
2nd Target Temp.	0	0	0	0	0	0	0	0	0	0
Step Size	0	0	0	0	0	0	0	0	0	0
Step Delay (Cycles)	0	0	0	0	0	0	0	0	0	0
Acquisition Mode	None	None	None	None	None	None	None	None	Cont.	None
Analysis Mode	Quantification		Quantification				Melting Curve			None

Temp. = Temperature; Trans. = Transition; Cont. = continuous

Table 17 – qRT-PCR Cycle Program for mouse *Ighmbp2* mRNA

***Ighmbp2*, murine**	**Denaturation**		**Amplification**				**Melting Curve**			**Cooling**
	1 Cycle		**50 Cycles**				**1 Cycle**			**1 Cycle**
Target Temperature	50	95	95	57	72	75	95	65	95	40
Incubation Time	2	10	15	30	30	5	0	15	0	40
Temp. Trans. Rate	20	20	20	20	20	20	20	20	0.1	20
2nd Target Temp.	0	0	0	0	0	0	0	0	0	0
Step Size	0	0	0	0	0	0	0	0	0	0
Step Delay (Cycles)	0	0	0	0	0	0	0	0	0	0
Acquisition Mode	None	None	None	None	None	None	None	None	Cont.	None
Analysis Mode	Quantification		Quantification				Melting Curve			None

Temp. = Temperature; Trans. = Transition; Cont. = continuous

Table 18 – qRT-PCR Cycle Program for mouse *Imp1* mRNA

***Imp1*, murine**	**Denaturation**		**Amplification**				**Melting Curve**			**Cooling**
	1 Cycle		**50 Cycles**				**1 Cycle**			**1 Cycle**
Target Temperature	50	95	95	58	72	78	95	65	95	40
Incubation Time	2	10	15	30	30	5	0	15	0	40
Temp. Trans. Rate	20	20	20	20	20	20	20	20	0.1	20
2nd Target Temp.	0	0	0	0	0	0	0	0	0	0
Step Size	0	0	0	0	0	0	0	0	0	0
Step Delay (Cycles)	0	0	0	0	0	0	0	0	0	0
Acquisition Mode	None	None	None	None	None	None	None	None	Cont.	None
Analysis Mode	Quantification		Quantification				Melting Curve			None

Temp. = Temperature; Trans. = Transition; Cont. = continuous

Table 19 – qRT-PCR Cycle Program for mouse *Fgfr1* mRNA

***Fgfr1*, murine**	**Denaturation**		**Amplification**				**Melting Curve**			**Cooling**
	1 Cycle		**50 Cycles**				**1 Cycle**			**1 Cycle**
Target Temperature	50	95	95	58	72	80	95	65	95	40
Incubation Time	2	10	15	30	30	5	0	15	0	40
Temp. Trans. Rate	20	20	20	20	20	20	20	20	0.1	20
2nd Target Temp.	0	0	0	0	0	0	0	0	0	0
Step Size	0	0	0	0	0	0	0	0	0	0
Step Delay (Cycles)	0	0	0	0	0	0	0	0	0	0
Acquisition Mode	None	None	None	None	None	None	None	None	Cont.	None
Analysis Mode	Quantification		Quantification				Melting Curve			None

Temp. = Temperature; Trans. = Transition; Cont. = continuous

Table 20 – qRT-PCR Cycle Program for human *GAPDH* mRNA

***GAPDH*, human**	**Denaturation**		**Amplification**				**Melting Curve**			**Cooling**
	1 Cycle		**40 Cycles**				**1 Cycle**			**1 Cycle**
Target Temperature	50	95	95	60	72	80	95	65	95	40
Incubation Time	2	10	15	30	30	5	0	15	0	40
Temp. Trans. Rate	20	20	20	20	20	20	20	20	0.1	20
2nd Target Temp.	0	0	0	0	0	0	0	0	0	0
Step Size	0	0	0	0	0	0	0	0	0	0
Step Delay (Cycles)	0	0	0	0	0	0	0	0	0	0
Acquisition Mode	None	None	None	None	None	None	None	None	Cont.	None
Analysis Mode	Quantification		Quantification				Melting Curve			None

Temp. = Temperature; Trans. = Transition; Cont. = continuous

Table 21 – qRT-PCR Cycle Program for human *β-Actin* mRNA

***β-Actin*, human**	**Denaturation**		**Amplification**				**Melting Curve**			**Cooling**
	1 Cycle		**40 Cycles**				**1 Cycle**			**1 Cycle**
Target Temperature	50	95	95	59	72	83	95	65	95	40
Incubation Time	2	10	15	30	30	5	0	15	0	40
Temp. Trans. Rate	20	20	20	20	20	20	20	20	0.1	20
2nd Target Temp.	0	0	0	0	0	0	0	0	0	0
Step Size	0	0	0	0	0	0	0	0	0	0
Step Delay (Cycles)	0	0	0	0	0	0	0	0	0	0
Acquisition Mode	None	None	None	None	None	None	None	None	Cont.	None
Analysis Mode	Quantification		Quantification				Melting Curve			None

Temp. = Temperature; Trans. = Transition; Cont. = continuous

Table 22 – qRT-PCR Cycle Program for human *IMP1* mRNA

***IMP1*, human**	**Denaturation**		**Amplification**				**Melting Curve**			**Cooling**
	1 Cycle		**40 Cycles**				**1 Cycle**			**1 Cycle**
Target Temperature	50	95	95	59	72	79	95	65	95	40
Incubation Time	2	10	15	30	30	5	0	15	0	40
Temp. Trans. Rate	20	20	20	20	20	20	20	20	0.1	20
2nd Target Temp.	0	0	0	0	0	0	0	0	0	0
Step Size	0	0	0	0	0	0	0	0	0	0
Step Delay (Cycles)	0	0	0	0	0	0	0	0	0	0
Acquisition Mode	None	None	None	None	None	None	None	None	Cont.	None
Analysis Mode	Quantification		Quantification				Melting Curve			None

Temp. = Temperature; Trans. = Transition; Cont. = continuous

Table 23 – qRT-PCR Cycle Program for human *FGFR1* mRNA

***FGFR1*, human**	**Denaturation**		**Amplification**				**Melting Curve**			**Cooling**
	1 Cycle		**50 Cycles**				**1 Cycle**			**1 Cycle**
Target Temperature	50	95	95	60	72	80	95	78	95	40
Incubation Time	2	10	15	30	30	5	0	15	0	40
Temp. Trans. Rate	20	20	20	20	20	20	20	20	0.1	20
2nd Target Temp.	0	0	0	0	0	0	0	0	0	0
Step Size	0	0	0	0	0	0	0	0	0	0
Step Delay (Cycles)	0	0	0	0	0	0	0	0	0	0
Acquisition Mode	None	None	None	None	None	None	None	None	Cont.	None
Analysis Mode	Quantification		Quantification				Melting Curve			None

Temp. = Temperature; Trans. = Transition; Cont. = continuous

2.14 Bioinformatics Software

Table 24 – List of Bioinformatics Software

Software	**Manufacturer**
FIJI (Fiji is just ImageJ)	Wayne Rasband (NIH)
GraphPad Prism 5	GraphPad Software, Inc.
MS Office / Excel	Microsoft
Adobe Illustrator CC 2017	Adobe
Endnote X8.2	Endnote
Image Studio lite	LI-COR Bioscience

2.15 Solutions, Buffers, and Cell Culture Media

Table 25 – List of Solutions, Buffers and Cell Culture Media

Solutions, Buffers and Cell Culture Media	**Ingredients**
0.15M boric acid buffer, pH 8.3	9.27g boric acid
	Ad 1l H_2O (sterile)
1% Trypsin	1% Trypsin in HEPES (pH 7.4)
10% separating gel	10% Acrylamide/Bis Solution
	1x separating gel buffer
	10% APS1
	1% TEMED
	in H_2O
100x PORN-H	500mg Poly-DL-ornithine hydrobromide in
	10ml 0.15M boric acid buffer, pH 8.3
10mM TRIS, pH 9.5	121.14g TRIS
	Ad 1l H_2O (sterile)

10x ELPHO	60.6g Tris-Base (250mM) 288g glycine (2M) 20g SDS (1%) Ad 2l ddH_2O
10x Tris-borate-EDTA-buffer (TBE buffer)	890mM TRIS 890mM boric acid 20mM Na_2EDTA
10x Towbin Buffer	60.6g Tris-Base (250mM) 288g Glycine (2M) Ad 2l H_2O
1xPBS (Phosphate buffered saline)	8g NaCl 0.2g KCl 1.44g Na_2HPO_4 0.24g KH_2PO_4 Ad 1l H_2O
1x PORN-H	500µl PORN-H (100x) in 50 ml boric acid buffer, pH 8.3
1x TBS-T (Tris-buffered saline with TWEEN20), pH 7.6	2.24g Tris Base 8g NaCl 1ml TWEEN 20 Ad 1l H_2O
2% Agarose gel	100ml 1x TAE buffer 2g Agarose 5µl Midori Green
4% PFA RNase-free (for FISH)	7.5ml Lysine-phosphate buffer 2.5ml 16% formaldehyde solution + 0.135g glucose + 0.021g sodium metaperiodate
4% PFA, pH 7.4	40g PFA Ad 500ml H_2O 410ml Na_2HPO_4 x 2 H_2O 90ml NaH_2PO_4 x 2 H_2O
4x separating gel buffer	1.5M TRIS, pH 8.8 0.4% SDS
4x stacking gel buffer	0.5M TRIS, pH 6.8 0.4% SDS

5% stacking gel	5% Acrylamide/Bis Solution
	1x stacking gel buffer
	10% APS1
	1% TEMED
	in H_2O
50x Tris-acetate-EDTA-buffer (TAE buffer)	2M Tris Base
	25mM Sodium acetate
	50mM EDTA
	AdH_2O
5M Betaine	20.28g Betaine monohydrate
	Ad 30ml H_2O
5x Laemmli Buffer	250mM Tris-HCl (pH 6.8)
	25% β-Mercaptoethanol
	10% SDS
	50% glycerol
	0.2% bromophenol blue
6x loading buffer	30% glycerin solution in TAE
	0.15% bromophenol blue
	0.15% xylene cyanol
	Add 1× TAE to 50 ml
ACSF medium (for FRAP)	127mM NaCl
	3mM KCl
	1.25mM $NaH_2PO_4H_20$
	23mM $NaHCO_3$
	25mM Glucose
Agar plates	7.5g selective Agar
	10g LB
	Ad 500ml H2O
Buffer I (for immunoaffinity chromatography)	20mM HEPES, pH 7.5
	500mM NaCl
	5mM $MgCl_2$
	10mM imidazole
	10% glycerin
	5mM ß-mercaptoethanol
	1:1000 protease inhibitors AP, L/P, AEBSF and PMSF

Buffer II (for immunoaffinity chromatography)	20mM HEPES, pH 7.5 100mM NaCl 5mM $MgCl_2$ 10% glycerine 50mM arginine 5mM ß-mercaptoethanol 1:1000 protease inhibitors AP, L/P, AEBSF and PMSF
Culture medium (for HEK293)	DMEM 10% FCS 1% Geneticin
DAPI	0.4µg/ml in 1xPBS
Depolarization solution	4g NaCl 1.1184g KCl Ad 500ml H_2O (sterile)
Digitonin-Lysis Buffer	150mM NaCl 50mM HEPES, pH7.4 25µg/ml digitonin
Elution-buffer (for immunoaffinity chromatography)	20mM HEPES, pH 7.5 100mM NaCl 5mM $MgCl_2$ 10% glycerine 50mM arginine 5mM ß-mercaptoethanol 1:1000 protease inhibitors AP, L/P, AEBSF and PMSF
High-salt Wash Buffer	50 mM Tris-HCl, pH 7.4 1 M NaCl 1 mM EDTA 1% Igepal CA-630 0.1% SDS 0.5% sodium deoxycholate

immunoaffinity chromatography-Lysis buffer	20mM HEPES, pH 7.5 500mM NaCl 5mM $MgCl_2$ 10mM imidazole 10% glycerin 0.01% NP40 5mM ß-mercaptoethanol 1:1000 protease inhibitors AP, L/P, AEBSF and PMSF
IP-Lysis Buffer	50 mM Tris-HCl, pH 7.4 100 mM NaCl 1% Igepal CA-630 0.1% SDS 0.5% sodium deoxycholate
Laminin-111	2.5µg/ml Laminin in HBSS
Laminin-221/211	2.5µg/ml Laminin in HBSS
LB medium	20g LB in 1l H_2O
Lysis buffer (Quick and Dirty) for DNA extraction	2.5ml 10% Sarcosyl 1ml 5M NaCl 2.5g Chelex Ad 50ml H_2O
Motoneuron medium (MN medium)	Neurobasal 2% B27 2% Horse serum (heat-inactivated, 56°C, 45min)
Neurobasal medium	Neurobasal 1% Glutamax (100x)
p75 solution	0.5µg/ml p75 in 10mM TRIS, pH 9.5
PNK Buffer	20 mM Tris-HCl, pH 7.4 10 mM $MgCl_2$ 0.2% Tween-20
RIP-Lysis buffer	50mM TRIS, pH 7.4 150mM NaCl 1mM $MgCl_2$ 0.1% NP-40 100U/ml RNasin RNase Inhibitor

Terrific Broth (TB) Medium	12g Bacto-tryptone
	24g Bacto-yeast extract
	4ml glycerol
	2.31g KH_2PO_4
	12.54g K_2HPO_4
	Ad 1l H_2O
Transfer Buffer	200ml Methanol
	100ml 10x Towbin Buffer
	Ad 1l H_2O
Trypsin inhibitor	500mg Trypsin inhibitor
	49ml HBSS
	1ml 1M HEPES (pH 7.4)

2.16 Experimental Animals and Animal Facility

For the following experiments controlled bred mice of the wild typical C57BL/6 or CD1 strain and the B6.BKS-$^{Ighmbp2nmd\text{-}2J/+}$ (*Nmd*^{2J}) strain of the institute's own animal facility were used. The animals were killed by cervical dislocation. After opening the abdominal cavity, the embryos were removed and transferred to HBSS. Subsequently, the age of the embryos was determined using a binocular according to Theiler's criteria (Bleyl, 1975). All following experiments took place in accordance with the German Animal Protection Act (§ 1, 4, 17 TierSchG).

3. Methods

3.1 Cell Culture

The following cell culture methods were performed at a sterile bench under sterile conditions. All required media, buffers or solutions were sterile filtered or autoclaved before use in order to create a clean experimental condition. This also included the decontamination of all equipment, materials and the workplace for disinfection with terralin or 70% technical ethanol.

The horse serum contained in the culture medium was inactivated at 56°C for 45min and sterile filtered before use.

To ensure a gentle cultivation of the cells without stress factors by too cool medium, all used media and solutions were heated to 37°C in a water bath.

In general, all cells were cultivated at 37°C with a humidity of 100% and 5% CO_2 concentration.

3.1.1 Isolation and Enrichment of Primary Embryonic Motoneurons

Isolation and enrichment of primary mouse motoneurons (MNs) were performed as previously described (Wiese et al., 2010). For the preparation of MNs, head and tail were separated from the embryo with the help of tweezers and the embryo was placed in a ventral position. Then, the skin was carefully detached, and the central canal of the spinal cord on the dorsal side was opened. The spinal cord was removed from the embryo and meninges including dorsal root ganglia were removed. The lumbar part of the prepared spinal cord was transferred to a 1.5ml reaction tube filled with HBSS. All further steps were carried out at the sterile bench. All spinal cords were separately incubated with 0.025% trypsin for 10min at 37°C. Next, the tissues were transferred separately into new reaction tubes with neurobasal and 0.1% Trypsin inhibitor to stop the digestion. To get single cell suspensions of each, digested spinal cords were dissociated by carefully pipetting up and down. All single cell suspensions were added to a 24-well cell culture plate coated with p75-antibody for 45min at RT, which had previously been washed three times with warm NB medium. The plate was kept vibration-free to select p75-receptor positive MNs. Additionally, the plate was carefully washed three times with warm NB medium and depolarization solution was added for 2min at room temperature (RT). Detached MNs were separately collected into 15ml centrifugation tubes with motoneuron medium (MN medium).

For single cell cultures, MNs were plated at a density of 2000 cells/cm^2 on glass coverslips pre-coated with poly-D/L-ornithine hydrobromide (PORN-H) along with either laminin-111 or laminin-211/221 and cultured for three (DIV3), five (DIV5) or seven days (DIV7) *in vitro*. Cells were cultured in neurobasal medium supplied with 2% B27 (Invitrogen), 2% heat-inactivated horse serum (Linaris), 500µM Glutamax (Invitrogen), 10ng/ml BDNF

(brain-derived neurotrophic factor) and 10ng/ml CNTF (ciliary neurotrophic factor). The medium was exchanged 24h after plating as well as at DIV3 and DIV5.

3.1.2 HEK293 Cell Cultivation

HEK293 cells were used from stocks frozen and stored in liquid nitrogen. This cell line was frozen with culture medium and 10% DMSO in cryotubes. After removing the cryotubes from the nitrogen tank, the cell suspension was gently thawed in a water bath at 37°C and was then transferred into a 15ml centrifugation tube provided with culture medium. The resulting cell suspension was centrifuged for 5min at 800rpm and 24°C in the centrifuge, the cell pellet was resuspended in culture medium and transferred to a culture flask with preheated culture medium. The cell medium was exchanged every three days.

To split the cells, the culture medium was aspirated, and the cells were washed twice with 1xPBS. Then the cells were removed from the bottom of the tissue culture flask by incubating with 0.25% trypsin/EDTA for 5min. Afterward, the enzyme reaction was stopped with culture medium and the resulting cell suspension was transferred into a 15ml centrifugation tube following by centrifugation for 5min at 800rpm at RT. The resulting supernatant was removed from the cell pellet, resuspended in culture medium and transferred to a new tissue culture flask with culture medium in the desired dilution. The cells were split approximately every 5-7 days.

3.1.2.1 Transient Plasmid Transfection using Lipofectamine 2000 Reagent

DNA plasmid and lipofectamine 2000 were separately added into two 1.5ml reaction tubes containing Opti-MEM medium and incubated for 10min at RT. Then, both solutions were mixed, incubated for 20min at RT and added dropwise to the HEK293 cells. Afterward, DNA lipid complex was supplied to seeded 10^6 cells per 6-Well plates cultured in DMEM medium without Penicillin/Streptomycin (P/S) for 6 hours (h) at 37°C. Next, the medium was aspirated and DMEM medium supplied with P/S was added. Cells were harvest after 36h of transfection.

3.1.2.2 Lentivirus Production

Lentiviral particles were packaged in HEK293 cells with pCMV-VSVG and pCMVΔR8.91 helper plasmids as described by (Rehberg et al., 2008).

Cells were transfected with lipofectamine 2000 containing Opti-MEM medium with 10% fetal calf serum for 12-14h and the virus was harvested after 72h of transfection by ultracentrifugation. This technique was carried out by my colleague Hilde Troll.

3.2 Immunoaffinity chromatography

3.2.1 Overexpression of Recombinant Full Length Human IGHMBP2 Protein

1µg pGex6p1 expression vector containing the full-length IGHMBP2 flanked by an N-terminal GST tag and a C-terminal 6xhis tag (wt) was added in 100µl heat shock competent Rosetta DE3 pLys Escherichia coli (*E. coli*) and incubated on ice for 20min. This was followed by a heat shock phase at 42°C for 45sec and cooling on ice for 2min. The cell suspension was put on a shaker for 1h at 37°C and 1400rpm and then centrifuged for 3min at 5000rpm. The supernatant was discarded up to a volume of 100µl so that the remaining cell suspension could be plated completely onto an LB plate mixed with chloramphenicol and ampicillin and cultured overnight at 37°C in an incubator.

The colonies grown on the LB plate were completely washed off and transferred to 800ml TB medium including 2g glucose and all antibiotics and then cultivated at 180rpm and 37°C to an optical density (OD) 600 is equal to 1.

Afterward, the culture was split into 6 cultures and used up to an OD600=0.8. At this time, the temperature was reduced to 25°C and the cultures were mixed with 2% EtOH, absolute (gel sample before induction). At OD600=1, the expression of recombinant full length human IGHMBP2 protein could be induced with 1M Isopropyl-β-D-thiogalactopyranoside (IPTG) at 14°C overnight (gel sample after induction).

3.2.2 Purification of 6xHis-IGHMBP2 with the help of Ni-NTA (nitrilotriacetic acid agarose) Beads

Next, the bacteria cultures were centrifuged for 15min at 4000rpm and 4°C. The supernatants were discarded, and all pellets were lysed with 25ml 4°C cold Lysis buffer and then sonicated on ice (output 5, duty cycle 50, 4x3min with 3min break).

Subsequently, the lysates were centrifuged for 1h at 25000rpm and 4°C (gel sample from supernatant and pellet). The supernatant was incubated with 3ml equilibrated Ni-NTA beads for 2h at 4°C on a head-over-tail rotator (gel sample of the supernatant after binding to Ni-NTA beads). For equilibration of Ni-NTA beads, beads were washed three times with lysis buffer.

Then, the 6xHis-IGHMBP2-loaded beads were treated with 150ml lysis buffer and then with 200ml buffer I. The elution was carried out in 10 fractions with 1ml elution buffer each fraction (gel sample of beads before the elution and after the elution). Protein concentrations were quantified with the Bradford protein assay.

3.2.3 Purification of GST-IGHMBP2 with the help of Glutathione Sepharose Transferase Beads

Next, all fractions were pooled depending on the protein concentration (gel sample of pooled fractions). The pooled fractions were incubated with 4 ml equilibrated glutathione-sepharose transferase (GST) beads for 2h at 4°C on an head-over-tail rotator (gel sample of the supernatant after binding to GST beads). For equilibration of GST beads, beads were washed three times with buffer I. Subsequently, GST-IGHMBP2-loaded-beads were treated with 200ml buffer I and then with 100ml buffer II.

3.2.4 Cross-linking of GST-IGHMBP2 to Glutathione Sepharose Transferase Beads

Cross-linking of GST-IGHMBP2 to GST beads was performed with Dimethyl-pimelimidate (DMP) to create a specific matrix for the Ighmbp2 antibody purification. For this purpose, GST beads were washed twice with 10ml 1xPBS + 0,01% NP40 and three times with 10ml disodium tetraborate (gel sample of beads before binding). Afterward, the IGHMBP2 proteins were covalently cross-linked to GST beads by incubating them with 10ml disodium tetraborate + 0.04g DMP for 30min at RT on a head-over-tail rotator (gel sample of beads after binding). Then, beads were washed three times with 10ml 0.2M ethanolamine (pH 8.0).

To saturate the still coupling active groups of the crosslinker, the beads were incubated with 10ml 0.2M ethanolamine (pH 8.0) overnight at 4°C on a head-over-tail rotator (gel sample of beads after saturation). Finally, beads were washed three times with 1xPBS.

3.2.5 Purification of the Ighmbp2 Antibody using an IGHMBP2-crosslinked Glutathione Sepharose Transferase Matrix

The polyclonal Ighmbp2 antibody of rabbit antiserum was purified with the help of IGHMBP2-cross-linked GST matrix. For this purpose, the IGHMBP2- crosslinked GST matrix was washed twice with 10ml 1xPBS+0,01% NP40. Previously, a poly prep column was incubated once with 10ml 1xPBS+0.01% NP40. Then, the matrix was washed once with 10ml 0.1M glycine (pH 2.7) and then neutralized with 10ml 1.5M Tris (pH 8.8) and washed twice again with 10ml 1xPBS+0.01% NP40.

Next, the filtered rabbit antiserum (0.4 µm filter) was incubated with the matrix for 90min at 4°C on the head-over-tail rotator (gel sample of beads). The matrix was washed twice again with 10ml 1xPBS + 0.01% NP40 and the elution was carried out in ten fractions with the help of a pH drop by 1ml 0.1M glycine (pH 2.7). All collected fractions were immediately neutralized with 200µl 1.5M Tris (pH 8.8) (gel samples of the respective fractions).

For long-term storage of IGHMBP2-cross-linked GST matrix, beads were neutralized with 10ml 1.5M Tris (pH 8.8) and then washed twice with 1xPBS + 0.01% NP40. It can be

stored in 1xPBS with 0.02% sodium azide (w/v) at 4°C for several weeks. The schematic diagram is depicted in Fig. 5.

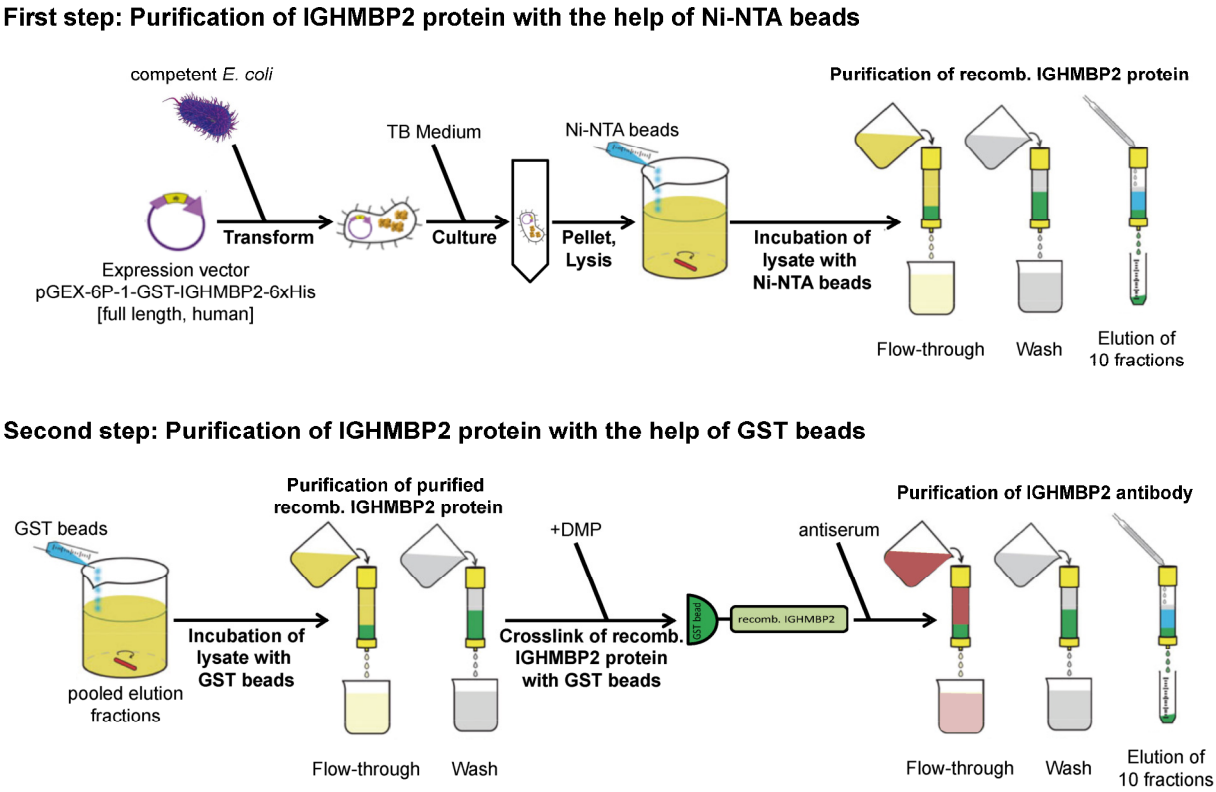

Figure 5 – Schematic diagram of immunoaffinity chromatography: the first step of recombinant GST-IGHMBP2-6xHis IGHMBP2 protein purification using Ni-NTA beads. The second step of recombinant GST-IGHMBP2-6xHis IGHMBP2 protein purification using GST beads. GST=glutathione sepharose transferase; Ni-NTA=nickel nitrilotriacetic acid; DMP=Dimethyl-Pimelimidate; recomb.=recombinant.

3.2.6 Enhancement of Eluted Ighmbp2 Antibody Solution using a Centricon

The gel samples and elution fractions were evaluated using SDS page and Coomassie staining. The pooled elution fractions were completely transferred into Centricon tubes and centrifuged at 5000rpm and 4°C for 1h to 1ml reservoir, refilled with 1xPBS and centrifuged to 1ml reservoir. This process was repeated once, and the filtrate was always discarded. Thereby a 5fold concentration of the antibody solution was achieved.

The antibody solution was mixed with 25% glycerin and 0.01% sodium azide, aliquoted into 100µl samples and stored at -20°C.

3.3 Immunocytochemistry

All steps were carried out at RT if not otherwise mentioned. At DIV5 or DIV7 MNs were fixed with 4% paraformaldehyde (PFA) for 10min, then washed three times with 1xPBS and permeabilized with 0.3% Triton in 1xPBS for 15min. After blocking with 10% BSA in 1xTBS-T for 1h the cells were incubated overnight at 4°C with primary antibodies diluted in 1% BSA in 1xTBS-T. Afterward, cells were washed three times with 1xTBS-T for 2min and

incubated for 1h with secondary antibodies diluted in 1% BSA in 1xTBS-T and nuclei were counterstained with DAPI. Subsequently, cells were washed three times with 1xTBS-T and mounted with Polymount.

For staining against α-, β- and γ-actin the staining protocol varied from the protocol described above. For staining of α-actin, the cells were incubated with 0.1% Triton-X in 1xPBS for 15min and the primary antibody was added on day two of staining and incubated for 3h before washing and incubating with secondary antibody. Cells stained with antibodies against β- and γ-actin were incubated with ice-cold methanol for 5min before permeabilization with 0.3% Triton in 1xPBS for 10min at RT.

The quantification of dendrite length, soma size, axon length and branching of Ighmbp2-deficient and control / wildtype MNs was performed on laminin-111 at DIV7. The longest axon per motoneuron was included into the statistical analysis and each primary branch of the longest axon was counted. The quantification of growth cone size and signal intensity of target proteins of Ighmbp2-deficient and control / wildtype MNs was performed on laminin-111 or laminin-211/221 at DIV5.

3.4 Fluorescence *in situ* Hybridization (FISH)

Fluorescence *in situ* hybridization (FISH) was performed according to the manufacturer's instructions (Panomics) with brief variances. All steps were carried out at RT if not otherwise mentioned and were performed under RNase-free conditions. MNs cultured on 10mm glass coverslips were fixed at DIV5 with 4% RNAse-free PFA for 15min. Next, cells were washed three times with newly prepared RNase-free 1xPBS for 5min. Thereafter, cells were incubated with hybridization solution supplied with 100µg/ml tRNA (salmon salt DNA) for 3min at 63°C and put on ice. The cells were incubated with hybridization solution supplied with 100µg/ml tRNA for 45min at 40°C. Next, 40nM Digoxigenin (DIG)-labelled LNA (locked nucleic acid) probes were added overnight at 40°C. Then, cells were washed five times with 2xSSC / 0.1% TWEEN20 for 1min at 45°C and three times with 1xSSC for 1min. Hybridized probes were detected by primary mouse anti-DIG antibody in 1% bovine serum albumin (BSA) in 1xPBS for 3h. Next, cells were washed five times with 2xSSC / 0.1% TWEEN20 for 1min and three times with 1xSSC for 1min. Fluorescent-labeled secondary antibody in 1% BSA in 1xPBS was added for 1h and the cells were washed again five times with 2xSSC / 0.1% TWEEN20 for 1min and three times with 1xSSC for 1min. Finally, MNs were mounted with Polymount.

3.5 Biochemical Methods

3.5.1 Extraction of Tissue and Cell Lysates

Ighmbp2-deficient and control / wildtype mice were killed by cervical dislocation. The target tissues were removed and immediately frozen in liquid nitrogen. The tissues were stored at -80°C until use. The frozen tissues were dispersed with 300µl RIPA buffer in glass ground homogenizers. After a centrifugation step of 5min at 4°C, the supernatant was removed and transferred to a new reaction tube. 2µl of the lysate was used to determine the protein concentration (Bradford test), the residues were stored at -20°C until use.

All acquired MNs from Ighmbp2-deficient and control / wildtype mouse embryos were cultured on PORN-H- and laminin-111-coated 24-well cell culture dishes for DIV7. Cells were directly lysed in 5x Laemmli buffer. Protein lysates were heated for 5min at 99°C and then centrifuged at 4°C and stored at -20°C until use.

3.5.2 Determination of Protein Concentration

In order to determine the protein concentration in tissue lysates, the BioRad protein assay was performed. This assay is based on the Bradford method, in which the color change of Coomassie Brilliant Blue G-250 dye from brown to blue after protein binding in acid solution is used. After an incubation time of 5min at RT, the optical density with the help of a photometer at 600nm was determined, a calibration line was calculated, and the concentration of the individual lysates was calculated.

Cell lysates were quantified by a BCA assay. Bivalent copper ions bind to the peptide bond and are reduced to monovalent copper ions at alkaline pH. In the presence of BCA, the copper ions build a blue-violet dye complex with BCA. The optical density with the help of a photometer at 562nm was determined, a calibration line was measured, and the concentration of the individual cell lysates was calculated.

3.5.3 SDS-Polyacrylamide Gel Electrophoresis (SDS-PAGE)

The protein samples were separated by polyacrylamide gel electrophoresis under denaturing conditions. First, the protein tissue samples were mixed with Laemmli buffer, heated to 99°C for 5min and then centrifuged at 4°C. SDS and mercaptoethanol contained in the Laemmli buffer denature the proteins and reduce all disulfide bridges. The tissue and cell protein samples were loaded into the pockets of a 1mm thick polyacrylamide gel consisting of a 5% stacking gel and a 10% separating gel. The negatively charged proteins migrate in the gel towards the positive pole and the rate of migration depends on their molecular weight.

3.5.4 Western Blot

A Polyvinylidene fluoride (PVDF) membrane was activated in methanol, then stored together with the blotting paper in transfer buffer. A layer of blotting paper, the PVDF membrane, the SDS gel and again a blotting paper were placed one after the other on the anode of the blotting apparatus. Protein samples separated on SDS-Page gels were transferred onto a PVDF membrane using the wet/tank blotting system for 1h at constant 150V and 4°C.

3.5.5 Immunodetection of Proteins on PVDF Membranes

The PVDF membrane was blocked with 5% milk powder in 1xTBS-T for at least 2h at RT to reduce unspecific binding of the antibody. The membrane was probed with the primary antibodies in 1xTBS-T at 4°C overnight. The membrane was then washed three times for 10min with 1xTBS-T and a corresponding HRP-coupled secondary antibody was applied for 2h in 5% milk powder in 1xTBS-T at RT. Afterward, the membrane was washed four times for 10min with 1xTBS-T and the immunodetection was performed using ECL Western Blotting systems according to the manufacturer´s instructions.

The light emitted by the oxidation of the Luminol substrate was detected using X-ray films with different exposure times. The development was done in a Curix 60 developer of AGFA.

3.5.6 Fractionation-Assay

Fractionation-assay was performed according to the EMC Research Notes instructions (Holden and Horton, 2009) with brief variances. HEK293 cells were cultured in 10cm dishes to 100% confluency. Cells were lysed with Digitonin-lysis buffer containing protease inhibitors (taking out sample / whole lysate). The lysates were centrifuged at 4°C for 5min at 3.000rcf and the supernatants were obtained. Pellet and supernatant were used to produce the nuclear and cytosol fraction.

Cytosolic fraction

The supernatant was centrifuged again at 4°C for 10min at 10.000rcf and its supernatant was collected and then sonicated on ice (0.5 amplitude and 100% cycles 2x10sec with 10sec break). The supernatant was centrifuged again at 4°C for 5min at 20.000rcf and its supernatant was collected as cytosolic fraction. The cytosolic fraction was directly diluted in Laemmli buffer and was heated to 99°C for 5min and then centrifuged at 4°C and stored at -20°C until use.

Nuclear fraction

The pellet was washed with Digitonin-lysis buffer and centrifuged at 4°C for 1min at 3.000rcf. The supernatant was discarded, RIPA buffer was added and the lysate was sonicated on ice (0.5 amplitude and 100% cycles 2x10sec with 10sec break). 4µl T-DNAse

and 2µl RNase were added to the lysate and incubated for 5min at 37°C. Next, the lysate was centrifuged again at 4°C for 5min at 20.000rcf and the supernatant was discarded. The pellet/nuclear fraction was diluted in Laemmli buffer and was heated to 99°C for 5min and then centrifuged at 4°C and stored at -20°C until use.

3.5.7 Co-Immunoprecipitation (Co-IP)

All steps were carried out at RT if not indicated otherwise. Dynabeads Protein A was equilibrated and washed two times with IP-Lysis buffer. Next, beads were loaded with 5µg target antibody by rotating for at least 1h and then antibody-bound beads were washed three times with IP-Lysis buffer.

HEK293 cells were cultured in 10cm dishes to 100% confluency and UV-crosslinked with 254nm with 0.15 Joules/cm^2 to covalently bind proteins and RNA molecules. Next, cells were incubated with IP-Lysis buffer on ice for 10min and then sonicated on ice (0.5 amplitude and 80% cycles 10x10sec with 2min break). Afterward, lysates were cooled down on ice for 3min and centrifuged for 10min at 10.000rpm and 4°C. The supernatant was collected into a new reaction tube (taking out sample / input). IP-Lysis buffer was removed from the beads, lysates were added to the beads and were incubated by rotating overnight at 4°C. The supernatant was discarded (taking out sample / flow-through). The beads were washed two times with high-salt wash buffer and then two times with PNK buffer. Beads were directly lysed in Laemmli buffer and subjected to Western Blot assay or stored at -20°C until use.

3.5.8 Radioactive Labeling of Crosslinked Protein-RNA Complexes

All steps were carried out at RT if not indicated otherwise. Dynabeads Protein A was equilibrated and washed two times with IP-Lysis buffer. Next, beads were loaded with the target antibody by rotating for at least 1h and then antibody-bound beads were washed three times with IP-Lysis buffer. HEK293 cells were cultured in 10cm dishes to 100% confluency and UV-crosslinked with 254nm with 0.15 Joules/cm^2 to covalently bind proteins and RNA molecules. Next, cells were incubated with IP-Lysis buffer on ice for 10min, followed by mild water bath sonication at 4°C (7x15sec with 15sec break). Then, lysates were treated in two conditions with a low and high concentration of RNase I for 3min at 1100rpm and 37°C in a heating block. Afterward, lysates were cooled down on ice for 3min and centrifuged for 10min at 10.000rpm and 4°C. The supernatant was collected into a new reaction tube (taking out of sample probe / input). IP-Lysis buffer was removed from the beads, lysates were added to the beads and were incubated on a 3D-shaker overnight at 4°C.

The supernatant was discarded (taking out of sample probe / flow-through). Beads were washed two times with high-salt wash buffer and then two times with PNK buffer. PNK buffer was removed and 4µl PNK mix was added to the beads for 5min at 1100rpm and 37°C in a heating block. Then, the beads were washed once with PNK buffer, absorbed with

NuPAGE loading buffer and incubated for 5min at 70°C. Samples were separated on a 4-12% NuPAGE Bis-Tris gel using MOPS running buffer. Novex wet transfer apparatus was used to transfer protein-RNA complexes onto a Nitrocellulose membrane. Protein-RNA complexes were detected using X-ray films at -80°C.

3.5.9 Immunoprecipitation of mRNA-Protein Complexes (RIP)

Immunoprecipitation of mRNA-protein complexes (RIP) was performed according to the Nature protocol instructions (Peritz et al., 2006) with brief variances. All steps were carried out at RT if not indicated otherwise. HEK293 cells were cultured in T75 flasks to 100% confluency and incubated with RIP-Lysis buffer on ice for 15min, followed by mild water bath sonication at 4°C (7x15sec with 15sec break). Then, the lysates were centrifuged for 15min at 208217rcf and 4°C. Dynabeads Protein A was equilibrated and washed two times with RIP-Lysis buffer. Afterward, supernatants of all lysates were precleared twice with equilibrated beads by shaking for 1h at 4°C (taking out sample / input) and in parallel beads were loaded with 2µg target antibody, control antibody and without antibody by rotating for at least 1h. Then, antibody-bound beads were washed three times with RIP-Lysis buffer and added to precleared lysates to incubate overnight at 4°C. Next, beads were washed five times with RIP-Lysis buffer (taking out sample / flow-through) and incubated with RIP-Lysis buffer supplied with 0.1% SDS and 0.3µg/µl proteinase K for 30min at 56°C in a heating block.

RNA isolation, DNase digestion, RNA isolation, and cDNA synthesis were performed with TRIzol Reagent, TURBO DNA-*free* Kit, TRIzol Reagent and the High-Capacity cDNA Reverse Transcription Kit according to the manufacturer's instructions.

For quantitative RT-PCR, absolute copy numbers of target mRNA from IGHMBP2- and IMP1-IP samples were normalized to absolute copy numbers of target mRNA from Input and IgG control condition.

3.5.10 Protein Synthesis Efficiency (SUnSET experiments)

All acquired MNs from Ighmbp2-deficient and control / wildtype mouse embryos were cultured on PORN-H- and laminin-111-coated 24-well cell culture dishes for DIV7. Cells were incubated with MN medium supplied with 10µg/ml puromycin and all neurotrophic growth factors for 1h at 37°C (Schmidt et al., 2009). Then, MNs were lysed directly in Laemmli buffer and were heated for 5min at 99°C, centrifuged at 4°C and subjected to Western Blot assay or stored at -20°C until use.

3.5.11 Label Newly Synthesized Proteins with L-Azidohomoalanine (AHA)

MNs from Ighmbp2-deficient and control / wildtype mouse embryos were cultured on PORN-H- and laminin-111-coated 10mm glass coverslips for DIV5. L-Azidohomoalanine

(AHA) labeling was performed according to Tom Dieck et al. 2012, with brief variances (Tom Dieck et al., 2012) at DIV5. The medium was aspirated and methionine-free DMEM supplied with 2% B27 and 10ng/ml BDNF/CNTF was added for 30min at 37°C. Next, cells were incubated for 1h with methionine-free DMEM supplied with 4mM AHA, 2% B27 and 10ng/ml BDNF/CNTF, which started the labeling process. As a control experiment, cells were incubated with 50ng/µl anisomycin in methionine-free DMEM supplied with 2% B27 and 10ng/ml BDNF/CNTF for 3h to inhibit protein synthesis before and during AHA-labeling. Then, cells were washed two times with pre-warmed PBS-MC and fixed with PFA-Sucrose for 20min. All following steps were carried out at RT if not indicated otherwise. Subsequently, cells were washed three times with 1xPBS, pH 7.4 for 2min and permeabilized with PBS-Tx for 15min. After blocking with B-Block for 1.5h, the cells were washed three times with 1xPBS for 10min and incubated overnight with FUNCAT reaction mix. Next, cells were washed three times with FUNCAT wash buffer for 10min and two times with 1xPBS for 10min. Finally, MNs were mounted with Polymount.

3.6 Molecular Biological Methods

3.6.1 Extraction of Genomic DNA

Tissue samples, e.g. tails from an E12.5 embryo, were digested in Quick and Dirty Lysis buffer with 2mg/ml Proteinase K for at least 30min at 55°C and 850rpm in a heating block. The samples were then heated to 99°C for 8min and centrifuged at 14000rpm. The isolated DNA was stored at 4°C.

3.6.2 Polymerase Chain Reaction (PCR)

3.6.2.1 Standard-PCR

This method was used to amplify specific DNA sequences. The DNA between the two primers is multiplied exponentially within several cycles (20-40) of denaturation, annealing, and elongation. The used primers were oligonucleotide primers with a length of about 20 nucleotides and a GC content of about 50%. In addition, the primer pair should not have any longer complementary sections. In the initial denaturation step, the double-stranded DNA is separated into single strands at high temperature to enable primer hybridization. The optimum annealing temperature (50-65°C) depends on the GC content and thus on the melting temperature of the primers. The next step is elongation at 72°C. Using a Taq polymerase, a new DNA strand is synthesized by attaching complementary deoxyribonucleotides (200µM) to the template in the 5'-3' direction. A buffer is added to keep the magnesium chloride concentration at approx. 1.5mM so that the Taq polymerase can

work correctly. In order to optimize the PCR reaction, betaine was also added to the sample. Betaine prevents the formation of secondary structures in GC-rich regions and thus improves DNA amplification.

3.6.2.2 Quantitative Reverse Transcriptase PCR (qRT-PCR)

Quantitative reverse transcriptase PCR (qRT-PCR) was performed to analyze the mRNA expression level of primary mouse MNs or human HEK293 cells. cDNA was quantified with LightCycler 96. Used primers and all program settings are shown in chapter 2.13. For qRT-PCR, absolute copy numbers of target mRNA were normalized to absolute copy numbers of Gapdh.

3.6.3 Genotyping

Genotyping was performed to determine the genotype of a mouse. This method is based on the purification of tissue DNA and its amplification by PCR followed by agarose gel electrophoresis. All gel electrophoreses were performed with 2% agarose gels at 120V for 45min.

3.6.3.1 *Nmd*^{2J} Mouse Line

The *Nmd*^{2J} mouse strain was obtained from the Jackson Laboratory and backcrossed to the genetic C57BL/6 background. The *Nmd*^{2J} (Ighmbp2-deficient) mouse line and the wildtype mouse line on the CD1 background were sheltered in the central animal facility of the University Hospital Wuerzburg. The animal care and ethics committees endorsed all described procedures and experiments. Genotyping of the Ighmbp2-deficient mouse line was performed as previously described (Cox et al., 1998).

The isolated DNA was amplified using the following PCR Reaction Mix (Table 26) and the cycle program is depicted in table 27.

Table 26 - PCR Reaction Mix

PCR Reaction Mix	Final Concentration
GoTaq MM (2x)	1x
DNA template	100-250ng
Forward Primer F15	0.6µM
Reverse Primer R14	0.6µM
Betaine	1M
Nuclease-Free Water to	25µl

Table 27 - PCR Cycle Program

PCR Cycle Program

	Temperature [°C]	Duration [min:sec]	Number of cycles
Initial Denaturation	94	03:00	1
Denaturation	94	00:30	
Primer Annealing	60	00:30	35
Elongation	72	01:00	
Terminal Elongation	72	05:00	1
Hold	4	∞	1

The point mutation in Intron 4 in *Nmd*^{2J} mice causes a new DdeI restriction interface, which is missing in wildtype animals. For this reason, a DdeI digestion was performed after PCR. The enzymatic restriction digestion of DNA was performed using DdeI and Tango Buffer (10x) according to the manufacturer's instructions. The complete PCR batch was incubated together with Tango Buffer and DdeI enzyme for 2.5h at 37°C. The DNA fragments were finally separated and analyzed by horizontal gel electrophoresis. In wildtypes, a band can be detected at 180bp and in mutants at 120bp. In heterozygous animals, both bands appear.

3.6.4 Horizontal Gel Electrophoresis

Horizontal gel electrophoresis was used to investigate the size of DNA fragments. The DNA samples were mixed with a 6x sample buffer and then pipetted into the pockets of a 2% agarose gel. Depending on their size, the negatively charged DNA fragments migrated towards the anode according to the applied voltage, whereby the small fragments ran fastest, and the highest bands represented the largest DNA fragments. The agarose gels were mixed with ethidiumbromide, which intercalates with DNA and was detected with a UV transilluminator. A 100bp DNA ladder was used as the size standard.

3.6.5 RNA Isolation and cDNA Synthesis

RNA isolation and cDNA synthesis were performed using the Nucleo Spin RNA Kit and SuperScript III First-Strand Synthesis Kit or High-Capacity cDNA Reverse Transcription Kit according to the manufacturer´s instructions. cDNA was diluted 1:5 with nuclease-free water.

3.6.6 RNA Sequencing

MNs from Ighmbp2-deficient and control / wildtype mouse embryos were cultured on PORN-H- and laminin 111-coated 24-well plate for DIV7. RNA isolation was performed using the Nucleo Spin RNA Kit according to the manufacturer´s instructions. RNA was pre-machined for RNA-Seq library generation using the mRNA-Seq Library Prep Kit V2. Pooled

libraries were sequenced on the Illumina NextSeq 500 with the High Output Kit v2 (75 cycles). Adapters and low-quality reads were designed with TrimGalore, v0.4.0 (http://www.bioinformatics.babraham.ac.uk/projects/trim_galore/) powered by Cutadapt, v1.8 (https://cutadapt.readthedocs.io/en/stable/) (Martin, 2011). As described in the Lexogen user manual, the first nine nucleotides from the 5' end of reading 1 were removed. Next, all reads were mapped with the help of STAR v2.5.0a (Dobin et al., 2013) and differentially expressed transcripts were defined using the Cufflinks package v2.2.1 (Trapnell et al., 2012) as previously described (Briese et al., 2016). The sequencing files have been recorded in NCBI's Gene Expression Omnibus (Edgar et al., 2002) and are available through GEO Series accession number GSE111224.

3.6.7 Molecular Cloning

1µg pSIH-H1 vector was incubated with 0.1U/µl EcoR1 and 0.1U/µl of the BamH1 enzyme in Tango Yellow Buffer for 1h at 37°C. Then, the cut vector was purified using QIAEX II – Gel Extraction Kit according to the manufacturer's manual. 20µM sense and antisense oligonucleotides in Tango Yellow Buffer were incubated for 5min at 95°C and annealed for 1h at 37°C. Next, 1µM annealed oligonucleotides and the 25ng linear pSIH-H1 vector was ligated with the help of 40 U/µl T4 ligase in ligase buffer for 1h at RT. The ligation product was used for plasmid transformation in competent Top10 *E. coli*. For this purpose, cells were incubated on ice for 15min following by a heat shock of 50sec in a 42°C water bath. Then, LB medium was added and incubated for 1h at 800rpm at 37°C in a heating block. The cell suspension was centrifuged for 5min at 1400rpm, 80% of the supernatant was discarded. Last 20% of the supernatant including the pellet was plated on an agar plate supplied with 1.5mg/ml ampicillin and incubated overnight at 37°C. Picked colonies were transferred into LB medium supplied with 4.5µg ampicillin and incubated for 8h at 800rpm and 37°C. The cell suspension was used for plasmid purification using the NucleoBond Xtra Mini/Midi/Maxi EF kit. Plasmid sequencing was done by LGC Genomics GmbH.

3.7 Life Cell Imaging

3.7.1 Calcium Imaging

MNs from Ighmbp2-deficient and control / wildtype mouse embryos were cultured on PORN-H- and laminin-111-coated 10mm glass coverslips for DIV5. Calcium indicator Oregon Green 488 BAPTA-1 AM was mixed with Pluronic F-27 / DMSO in an ultrasound sonifier for 2min.

For labeling intracellular calcium, MNs were treated with calcium imaging buffer supplied with the calcium indicator for 13min at 37°C. Next, recordings were performed in a heated chamber with calcium imaging buffer using a confocal microscope with a 40x

objective. Time-lapse images with a frequency of 2.5Hz and an exposure time of 400ms were acquired. Real-time images were displayed by StreamPix (Norpix) software and MNs were irradiated with a LED light source (Visitron Systems) using the following filter settings: excitation 482±35nm, dichroitic filter 506nm, emission filter 536±40nm. The analysis was performed with ImageJ software with the help of two plugins *Intensity vs Time Monitor* and *Time Series Analyzer V2.0,* which allowed the determination of activity events by measuring calcium influx in defined regions of interest (ROIs).

3.7.2 Fluorescence Recovery after Photobleaching (FRAP)

Manufacturing of the lentiviral eGFP^{myr} reporter construct was described previously (Rathod et al., 2012). Stop codon of myristoylated-eGFP in a FUValentin lentivirus vector under control of the ubiquitin promoter was directly linked to the complete 3'UTR of β-actin. MNs from Ighmbp2-deficient and control / wildtype mouse embryos were cultured on PORN-H- and laminin-111-coated µ-dishes for DIV5 in presence of 10ng/µl BDNF and 10ng/µl CNTF and transduced with eGFP^{myr}-β-actin 3'UTR lentivirus. Recordings were performed with an inverted SP5 confocal microscope using a 60x1.35-NA oil objective as previously described (Moradi et al., 2017). First, the axon terminal with an area of approximately 100µm was recorded every 30sec for 4min at 19% laser power followed by bleaching using 80% laser power. Fluorescence recovery was observed for 1h every 30sec. Post-bleach time-lapse images were analyzed as the mean intensity grey values per pixel in ROIs of growth cone and soma. Upcoming recovery was calculated using Leica LAS lite software. Starting signal intensity F0 was defined as the mean intensity average of 8 pre-bleach images. Post-bleach signal intensity was defined as the average of signal intensities of 10 immediate post-bleach images. This was done to eliminate the initial postbleach signal. Post-bleach signal intensity was then normalized to starting signal intensity to calculate the percentage recovery.

As a control experiment, cells were incubated with 50ng/µl anisomycin for 2h to inhibit protein synthesis before recording.

3.8 Mouse Growth Factor Array

Blood from P28 Ighmbp2-deficient and control/wildtype mice was collected after intraperitoneal injection with Ketamin (120mg/kg in 0.9% NaCl) and Xylazine (16mg/kg in 0.9% NaCl). It was kept for 20min at RT and centrifuged for 30min at 12000rpm. Blood serum was diluted with blocking buffer 1:10 supplied with protease inhibitors. Meanwhile, the membrane was blocked with blocking buffer for at least 30min at RT. C2 Growth Factor Array was carried out according to manufacturer's manual with the following incubation times: sample incubation 5h at RT, biotinylated antibody solution overnight at 4°C and streptavidin

antibody solution 2h at RT. Signal intensity quantifications were determined according to the manual using Image Studio Lite software.

3.9 Proteomics

3.9.1 Pulsed SILAC

The complete acquired Ighmbp2-deficient and control / wildtype MNs per E12.5 embryo were seeded on PORN-H/laminin-111-coated on 24-well plates with MN medium and neurotrophic growth factors for 24h. Then, the medium was exchanged to light media condition for the next 24h. Cells were washed twice with pre-warm amino acid-free Neurobasal supplied with 500µm Glutamax to wash out the light media and then heavy (H, for control MNs) or medium heavy (M, for Ighmbp2-deficient MNs) media condition was added to the cells for 20h. Next, cells were washed twice with 1xPBS and RIPA lysis buffer was added on ice for 10min. Lysates were centrifuged for 30sec at 208217rcf and 4°C followed by mild water bath sonication at 4°C (7x15sec with 15sec break). Then, lysates were centrifuged again for 2min at 208217rcf and 4°C and quantified by BCA assay. Incorporated heavy or medium-heavy amino acids in newly synthesized proteins of control and Ighmbp2-deficient MNs were analyzed by mass spectrometry of resulting mass differences. The schematic diagram is depicted in Fig. 6.

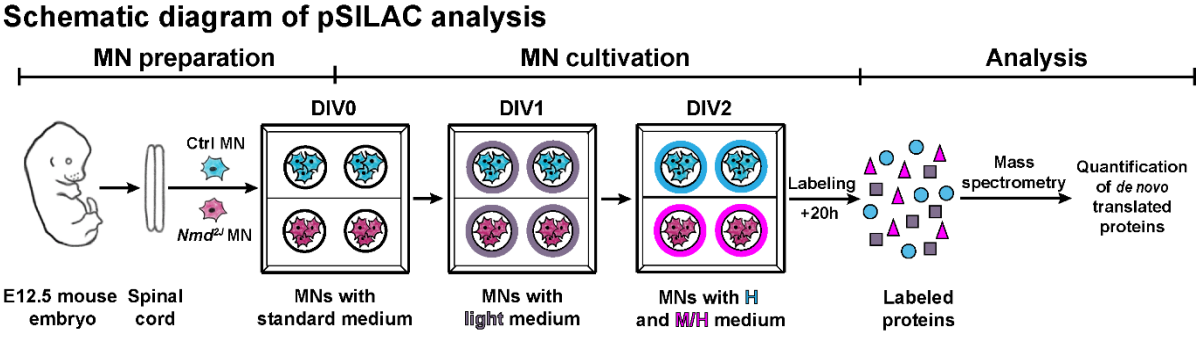

Figure 6 - Schematic diagram of pSILAC analysis: motoneuron preparation and labeling of *de novo* translated proteins in control and *Nmd*^{2J} (Ighmbp2-deficient) motoneurons. Ctrl=control, MN=motoneuron, H=heavy amino acids; M/H=medium heavy amino acids. Modified according to (Surrey et al., 2018).

3.10 Statistics

The depicted results were obtained from at least three independent experiments and were shown as mean±standard error of the mean (SEM) or mean±standard deviation (SD). Biological and technical replicates were indicated with "n" and the total number of evaluated test cases (e.g. axons, growth cones, cell bodies) represents "N". The statistical analyses were performed with GraphPad Prism 5 software. In datasets of two groups, the statistical analysis was quantified using the Mann-Whitney U-test (no Gaussian distribution; Ca^{2+}

imaging, Western blot, qRT-PCR, axon length, cell body size, dendrite number, mean dendrite length, total dendrite length, growth cone size, signal intensities, FPKM RNA-Seq). For datasets with more than two groups, two-way ANOVA with Bonferroni post-hoc test (Gaussian distribution, FRAP analysis) or a one-way ANOVA with Tukey's multiple comparison test (Gaussian distribution, axonal branching and RIP analysis) and a one-way ANOVA/Kruskal-Wallis test with Dunn's multiple comparison test (no Gaussian distribution, Western blot of Ighmbp2 KD or bFGF long-term treatment FGFR and AHA-labeling) or repeated measures test with Dunnett's Multiple Comparison Test (C2 Mouse Growth Factor Array) was used.

Significance levels are consistently reported as n.s. not significant and $p^{*}<0.05$, $p^{**}<0.01$ and $p^{***}<0.001$. The images were generated and quantified using the confocal microscope SP2 (Leica) / Leica LAS LITE and the confocal laser scanning microscope Olympus Fluo View FV1000 (IX81) / FIJI software. The signal intensity was measured as arbitrary unit per area based on quantum levels (QL) per pixel. All images were processed with FIJI and Adobe Illustrator CS5 and the linear contrast enhancement was applied, and all individual images were treated equally.

4. Results

Spinal muscular atrophy with respiratory distress type 1 (SMARD1) is a motoneuron disease in children with fatal outcome and unknown pathomechanism. The mutant IGHMBP2 gene encoding a superfamily 1 (SF1) RNA/DNA helicase causes the onset of this disorder. The neuromuscular disorder *(Nmd^{2J})* mouse model is indispensable for the investigation of the disease mechanism under SMARD1. Nevertheless, the function and the affected cellular processes are almost unknown. With the help of primary motoneuron cultures, a detailed knowledge of the spinal muscular atrophy (SMA) disease mechanism has already been obtained. Therefore, the present Ph.D. thesis aims to gain a broader understanding of the SMARD1 disease mechanism using primary cultured Ighmbp2-deficient motoneurons to elucidate the function of the ribosomal RNA/DNA helicase Ighmbp2.

4.1 Ighmbp2 Antibody Validation

Most of the results from section 4.1 are published in (Surrey and Jablonka, 2018; Surrey et al., 2018).

Numerous assays and approaches can be used to analyze the function of a protein or molecule. However, independent from the chosen experiment, it is essential to tag or mark the protein of interest. Since there is no anti-Ighmbp2 antibody available for purchase, it was necessary to produce an antibody against the helicase for the following experiments. Antibodies against the Ighmbp2 protein were obtained by immunizing rabbits with an antigen against the full-length recombinant human IGHMBP2, a polyclonal antibody was formed, which differ in their epitope specificities. All antibodies have the same antigen specificity - but they are directed at different epitopes of this antigen (Luttmann et al., 2009). Immunoaffinity chromatography was performed to purify the rabbit antiserum.

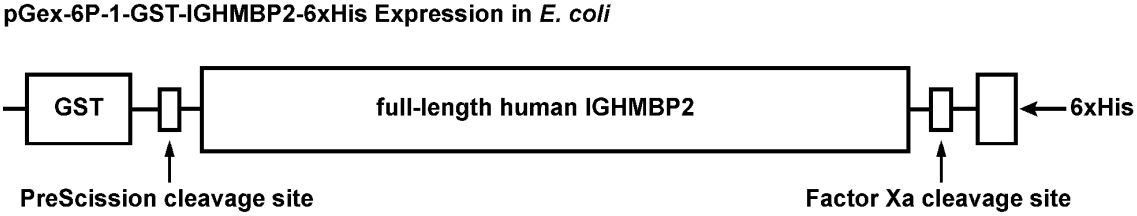

Figure 7 - Overexpression of recombinant human IGHMBP2 in *E. coli*. The protein with an N-terminal GST- and a C-terminal 6xHis-fusion tag was overexpressed in *E. coli* Rosetta cells (Guenther et al., 2009a).

For this purpose, a derivative of the pGex-6P-1 expression plasmid vector containing the full length of human IGHMBP2 was used, which enables overexpression of the IGHMBP2 protein in *E. coli* Rosetta cells (Fig. 7). The construct of recombinant IGHMBP2 was described in the publication (Guenther et al., 2009a) and the purification was supervised by the group of Prof. Dr. Utz Fischer at the Institute of Biochemistry of the Julius-Maximilians-University Würzburg.

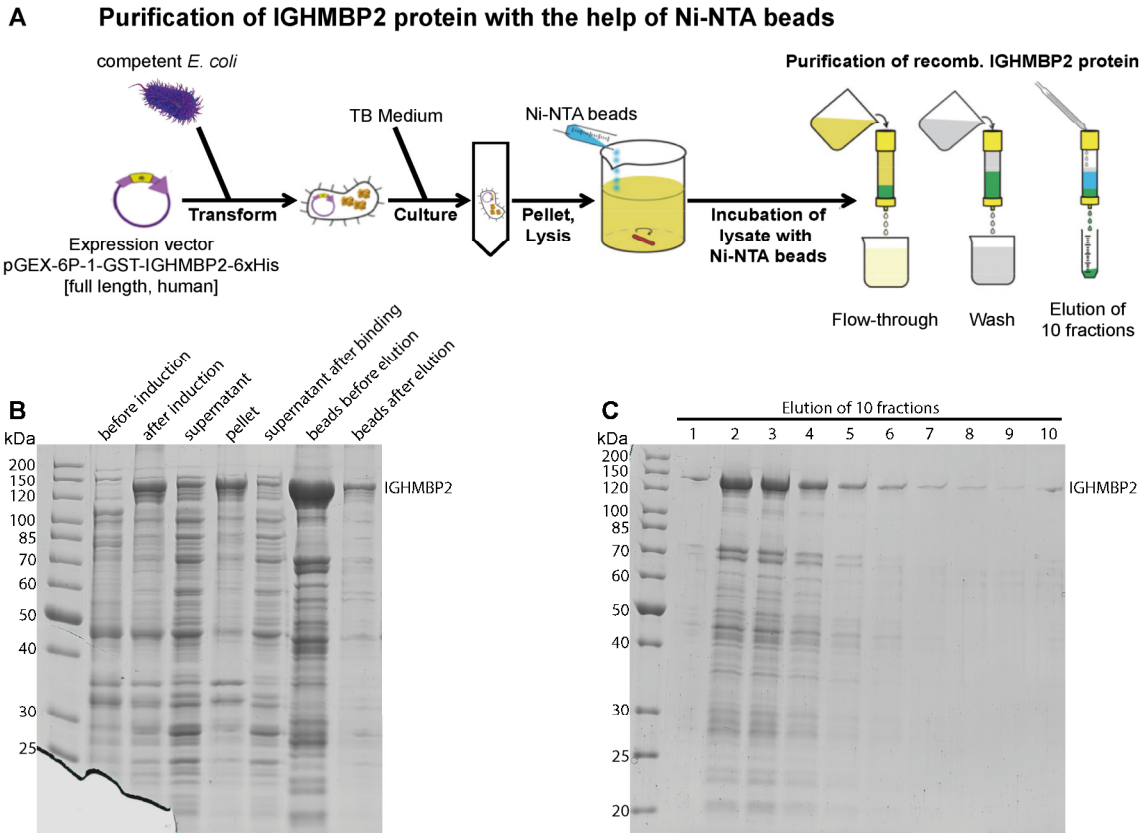

Figure 8 – Purification of IGHMBP2 protein with the help of Ni-NTA beads. (A) Schematic diagram of experimental design: the first step of recombinant GST-IGHMBP2-6xHis protein purification using Ni-NTA beads. Ni-NTA=nickel nitrilotriacetic acid; recomb.=recombinant. (B) Sample examination of the different experimental sections using SDS-PAGE and Coomassie blue staining. (C) Verification of the IGHMBP2 protein expression in all 10 eluted fractions using SDS-PAGE and Coomassie blue staining.

First, the pGEX-6P-1-GST-IGHMBP2-6xHis plasmid was overexpressed in competent *E. coli* Rosetta cells. Significantly increased protein was observed after induction compared to before (Fig. 8B, before and after induction). The protein lysate was produced by centrifugation followed by lysis. After centrifugation, most of the proteins were detectable in the pellet and only a small amount remained in the supernatant (Fig. 8B, pellet and supernatant).

In the first purification step, the protein lysate was eluted into 10 fractions using Ni-NTA beads (Fig. 8A). The lysate was incubated with Ni-NTA beads so that the GST-IGHMBP2-6xHis protein could be bound to the beads and removed from the supernatant of the lysate. The successful elution of the purified GST-IGHMBP2-6xHis protein was confirmed by a beads sample after the elution in which the IGHMBP2 protein was only weakly detectable compared to a beads sample before elution (Fig. 8B, supernatant after binding and beads before elution). The IGHMBP2 level of the 10 eluted fractions was also checked (Fig. 8C). The varied fractions contained a different amount of GST-IGHMBP2-6xHis protein. In the fractions 2 to 5 the largest amount of protein could be determined (Fig. 8C). Since each fraction contained protein, all fractions were pooled for the second purification step.

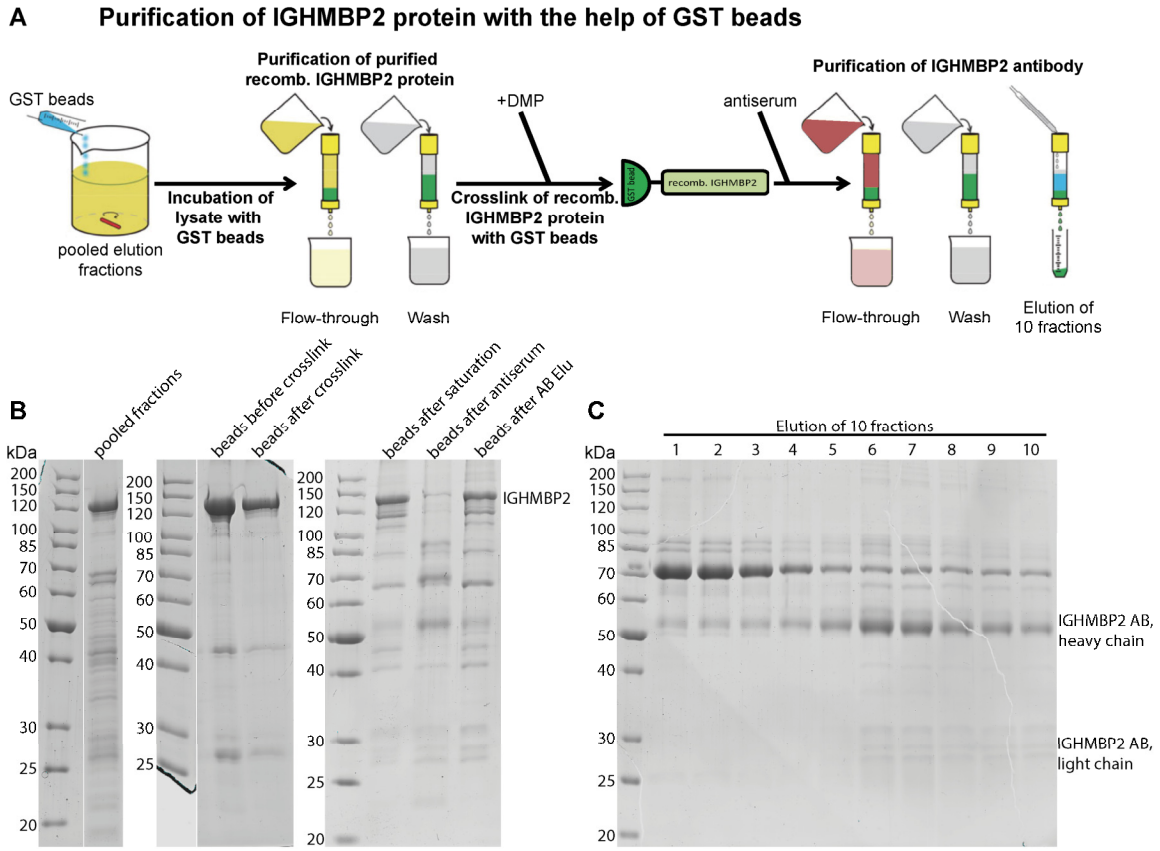

Figure 9 - Purification of IGHMBP2 protein with the help of GST beads followed by antibody purification. (A) Schematic diagram of experimental design: the second step of recombinant GST-IGHMBP2-6xHis IGHMBP2 protein purification using GST beads. GST=glutathione sepharose transferase; recomb.=recombinant. (B) Sample examination of the different experimental sections using SDS-PAGE and Coomassie blue staining. (C) Verification of the Ighmbp2 antibody concentration in all 10 eluted fractions using SDS-PAGE and Coomassie blue staining. AB means antibody and DMP means Dimethyl-pimelimidate.

In the second purification step, the pooled fractions were incubated with GST beads and the bound GST-IGHMBP2-6xHis proteins were covalently bound to the beads using Dimethyl-pimelimidate (DMP). This created a specific matrix to purify the antiserum into 10 fractions by immunoaffinity chromatography (Fig. 9A). This second purification step was performed to increase the purity of recombinant IGHMBP2 protein to produce a specific antibody.

The IGHMBP2 level of all pooled fractions was checked (Fig. 9B, pooled fractions), the lysate was incubated with GST beads for the GST-IGHMBP2-6xHis protein to bind (Fig. 9B, beads before crosslink). The bound proteins were covalently linked to the beads by DMP (Fig. 9B, beads after crosslink). After crosslinking, the active coupling groups of the crosslinker were saturated (Fig. 9B, beads after saturation). The specific matrix for immunoaffinity chromatography was prepared and used to purify the antiserum.

These beads were finally incubated with the antiserum in order to purify the specific antibodies against IGHMBP2 using the produced matrix. The successful binding of the antibody to the matrix was demonstrated by a small detected amount of protein (Fig. 9B, beads after antiserum). The successful elution of the 10 fractions was confirmed by the detection of GST-IGHMBP2-6xHis protein of the beads (Fig. 9B, beads after AB Elu). The

Ighmbp2 antibody level of all eluted fractions was checked (Fig. 9C). The varied fractions contained a different amount of antibody. In fractions 6 to 10, both the heavy chain and the light chain of the eluted Ighmbp2 antibody could be detected (Fig. 9C), so that only these fractions were pooled and concentrated using Centricon.

In order to test the specificity of this antibody, a number of different validation tests was carried out. As already described in (Grohmann et al., 2004), Ighmbp2 is predominantly localized in the cytoplasm. Therefore, cytoplasmic and nuclear fraction lysates of HEK293 cells were prepared to confirm the localization of IGHMBP2.

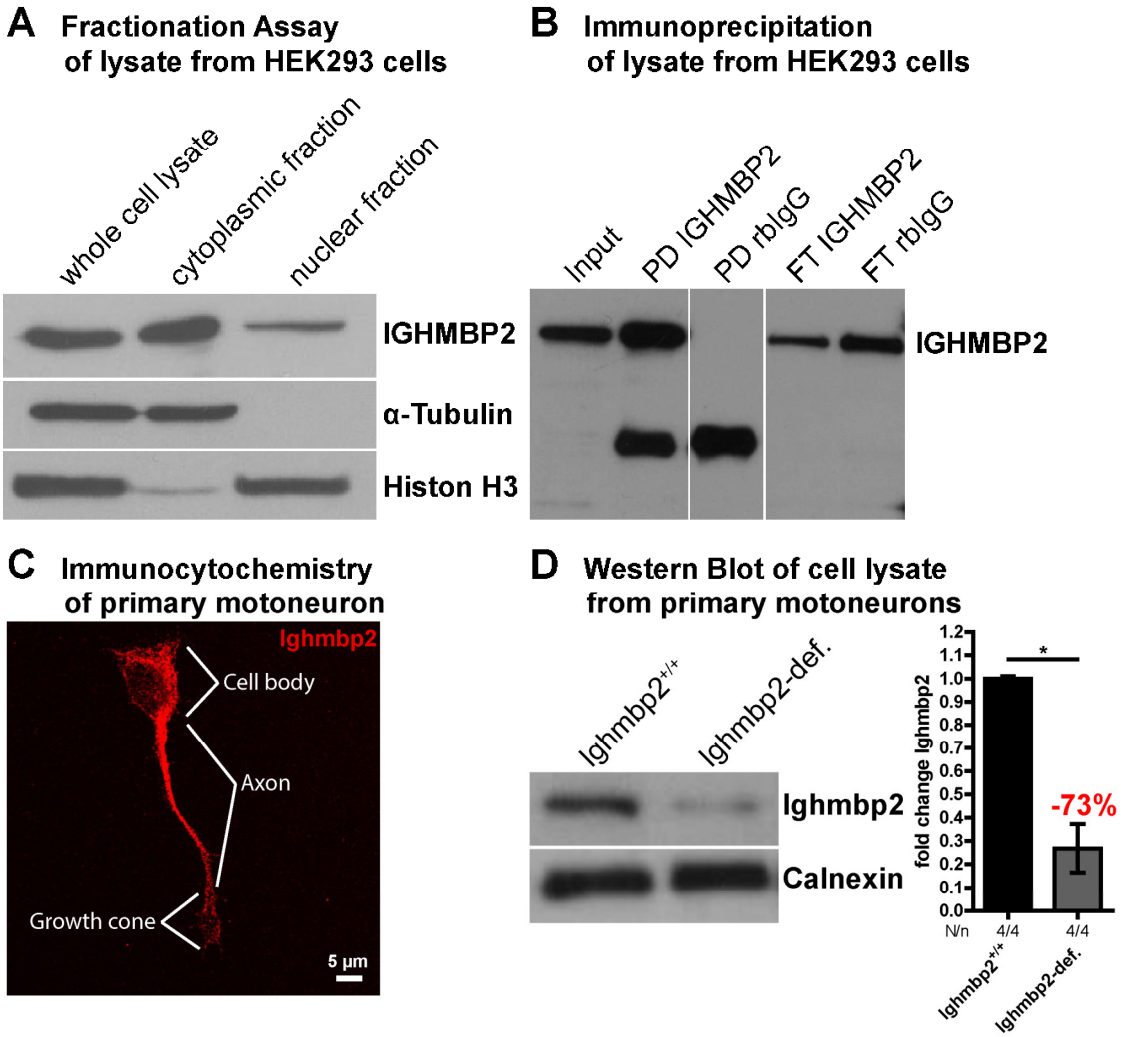

Figure 10 - Validation of Ighmbp2 Antibody. (A) Representative Western Blot for the cytoplasmic and nuclear fraction of lysate from HEK293 cells. IGHMBP2 protein is predominantly localized in the cytoplasmic fraction. α-Tubulin and Histone H3 are used to check the purity of the two fractions as a marker for the cytosolic and nuclear fraction. (B) Representative Western Blot for immunoprecipitated IGHMBP2 protein. Successful pulldown (PD) of IGHMBP2 and the PD with rabbit IgG control antibody is free of the target protein. The flow-through of IGHMBP2 PD shows decreased IGHMBP2 protein compared to the flow-through of rbIgG PD. (C) Intracellular distribution of Ighmbp2 protein in primary wildtype motoneurons. It is observed predominantly in the cytoplasm of the cell body and the axon, but only weakly expressed in the growth cone. (D) Representative Western Blot of Ighmbp2-deficient (Ighmbp2-def.) and Ighmbp2$^{+/+}$ motoneuron lysate (left panel). Quantification of the Ighmbp2 protein level in Ighmbp2-def. and Ighmbp2$^{+/+}$ motoneurons (right panel). Ighmbp2-def. motoneurons show a significant Ighmbp2 protein reduction of 73%. In D, data are shown as mean±SD. N defines the number of embryos; n indicates the number of experiments. Each experiment was repeated at least 3 times, if not mentioned otherwise. Modified according to (Surrey and Jablonka, 2018) and (Surrey et al., 2018).

The detection of IGHMBP2 protein in the respective fractions clearly showed that IGHMBP2 is predominantly localized in the cytoplasm and only a small amount can be found in the nucleus (Fig. 10A). Immunoprecipitation of HEK293 lysates using the Ighmbp2 antibody showed a successful pulldown of IGHMBP2 protein (Fig. 10B). Subsequently, the purified antibody was tested in an immunocytochemical staining. The intracellular distribution of Ighmbp2 protein in primary motoneurons also showed a predominant localization in the cytoplasm of cell bodies and axons, but it was only weakly represented in the growth cones (Fig. 10C). To perform further detailed morphological and functional analyses of Ighmbp2-deficient (Ighmbp2-def.) motoneurons, the protein level of Ighmbp2 was quantified in primary motoneurons. Ighmbp2-deficient motoneurons showed a significant Ighmbp2 reduction of 73% compared to Ighmbp2$^{+/+}$ (Fig. 10D). Based on these results, the purified Ighmbp2 antibody could be used in the following experiments.

4.2 Morphological and Functional Analyses of isolated Motoneurons from the Neuromuscular Disorder Mice (Nmd^{2J}) and wildtype Mice

Most of the results from section 4.2 are published in (Surrey et al., 2018). To address the question whether the SMARD1 phenotype results from de-regulation of protein biosynthesis, we performed morphological and functional analyses of isolated Ighmbp2-defcient motoneurons from the neuromuscular disorder mouse (*Nmd^{2J})* (Surrey et al., 2018).

4.2.1 Ighmbp2 deficiency causes reduced β-actin protein levels in growth cones of isolated motoneurons

Since the number of generated motoneurons per *Nmd^{2J}* embryo is limited and genotype-dependent, it was first tested whether a lentiviral knockdown (KD) of Ighmbp2 in primary embryonic motoneurons isolated from wildtype (CD1) mice could circumvent these barriers.

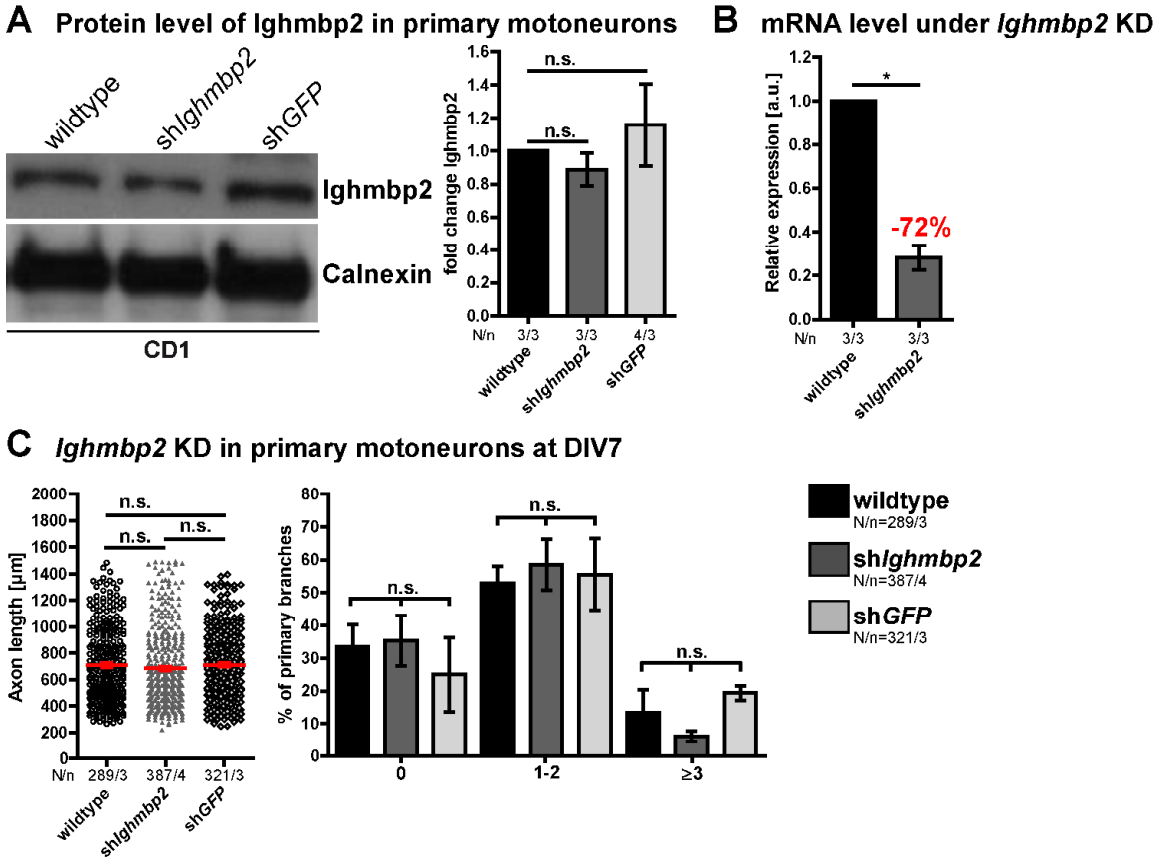

Figure 11 - Protein and mRNA level in primary cultured wildtype (CD1) motoneurons under *Ighmbp2* KD. (A) Representative Western Blot of wildtype, sh*Ighmbp2* and sh*GFP* motoneuron lysates (left panel). Quantification of the Ighmbp2 protein level in all motoneuron lysates (right panel). Motoneurons with lentiviral gene transfer for sh*Ighmbp2* (sh*Ighmbp2*) exhibit no reduced amount of Ighmbp2 protein compared to both control conditions (wildtype and lentiviral gene transfer for control sh*GFP*). (B) However, a significant reduction of 72% *Ighmbp2* mRNA is observed in motoneurons with lentiviral gene transfer of sh*Ighmbp2* compared to the wildtype. (C) Neither the sh*Ighmbp2*, nor sh*GFP* motoneurons show altered axonal outgrowth (in each case left panels) or affected axon branching behavior (in each case right panels) in comparison to the wildtype. In A (right panel), B and C (right panel), data are shown as mean±SD. In C (left panel), data are shown as mean±SEM. N defines number of embryos (A, B) or number of analyzed cells (C); n indicates the number of experiments. % means percentage. Modified according to (Surrey et al., 2018).

Lentiviral KD of *Ighmbp2* gene (sh*Ighmb2*) in primary cultured wildtype (CD1) motoneurons showed a significant reduction of 72% *Ighmbp2* mRNA (Fig. 11B) but no alteration at the protein level was observed after 7 days *in vitro* (DIV7) (Fig. 11A, left and right panel). In addition, we performed morphological analyses of the axonal outgrowth and the branching behavior of isolated motoneurons under *Ighmbp2* KD at DIV7. In this case, no significant alteration of axonal elongation (Fig. 11C, left panel) or branching capacity (Fig. 11C, right panel) was observed between wildtype, lentiviral KD of *Ighmbp2* gene (sh*Ighmbp2*) and lentiviral control KD of *GFP* gene (sh*GFP*) in primary motoneurons (Fig. 11C).

For these reasons, all following experiments were executed with Ighmbp2-defcient motoneurons of the *Nmd*^{2J} mouse model cultured on either a Schwann cell-specific laminin isoform (laminin-111) or synapse-specific laminin isoform (laminin-211/221) for three (DIV3), five (DIV5) and/or seven (DIV7) days according to the scientific issue.

The functional study started with the analysis of spontaneous Calcium (Ca^{2+}) transients at the distal axon. This is an important parameter for the correct cellular differentiation and function of primary motoneurons.

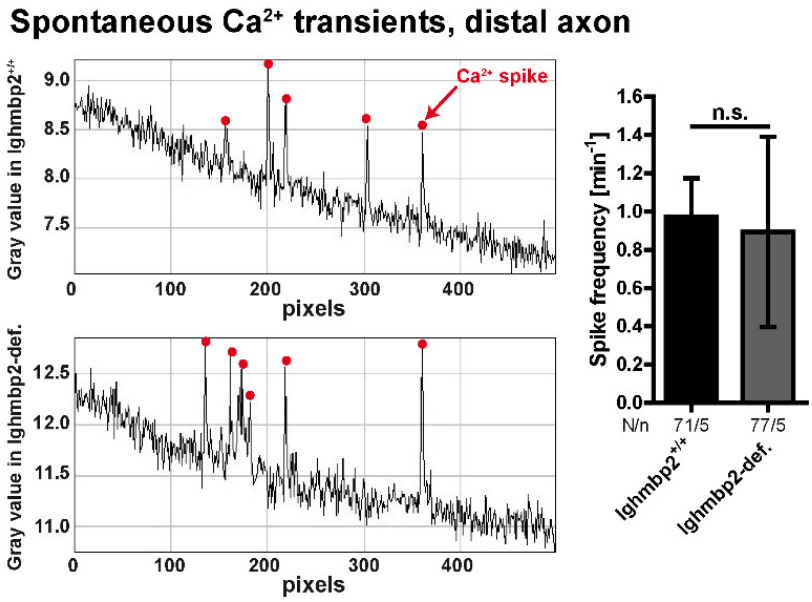

Figure 12 - Spontaneous Ca^{2+} transients in Ighmbp2-def. motoneurons. Representative live-cell recordings of spontaneous spike-like Calcium (Ca^{2+}) transients of Ighmbp2-def. and Ighmbp2$^{+/+}$ motoneurons at DIV5 (left panel). Ighmbp2-def. motoneurons show no affected frequency of spontaneous Ca^{2+} spikes, indicated by red dots, in their corresponding growth cones (right panel). Data are shown as mean±SD. N defines number of analyzed cells; n indicates the number of experiments. Modified according to (Surrey et al., 2018).

Analysis of spontaneous Ca^{2+} transients at the distal axon showed no changes in the frequency of spontaneous spike-like Ca^{2+} transients in Ighmbp2-deficient motoneurons compared to Ighmbp2$^{+/+}$ at DIV5 (Fig. 12). This observation corresponded to the axonal outgrowth of Ighmbp2-deficient motoneurons at DIV3, DIV5, and DIV7.

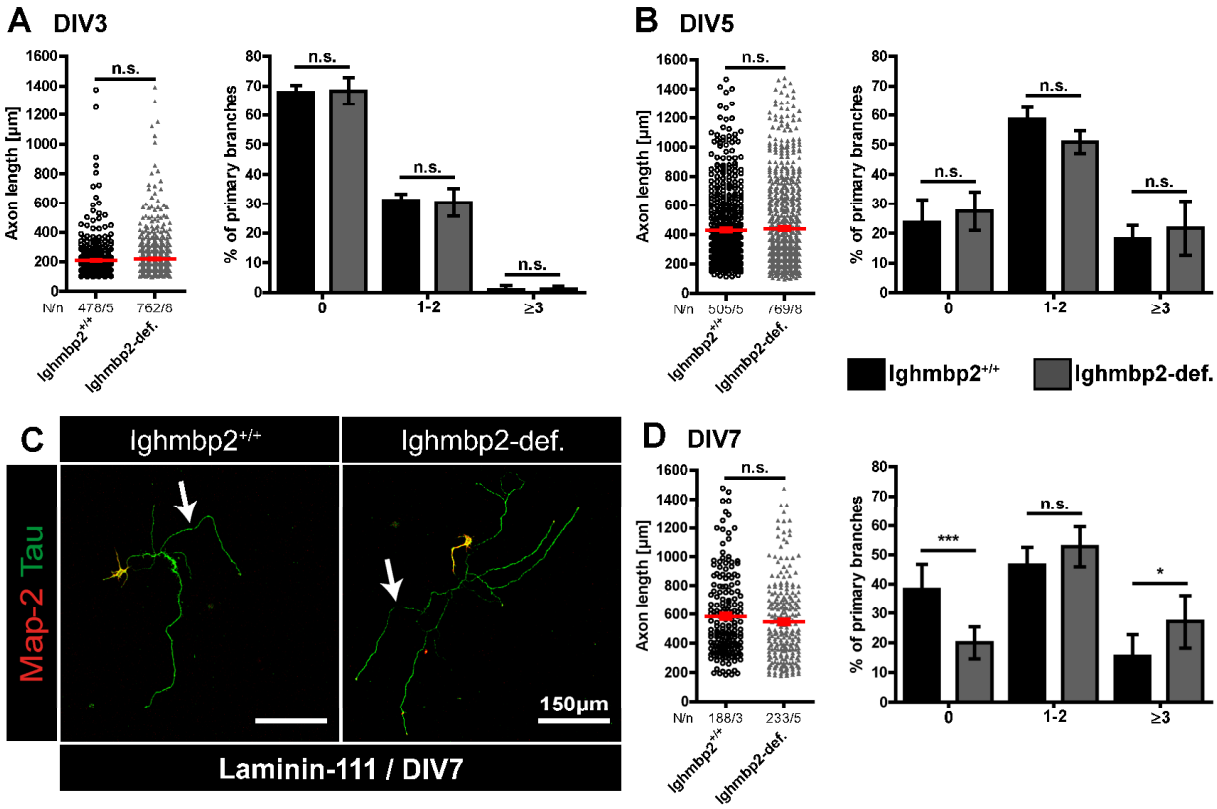

Figure 13 - Analyses of axonal outgrowth and branching behavior at DIV3, DIV5, and DIV7. (A, B) Neither at DIV3 (A) nor at DIV5 (B), Ighmbp2-def. motoneurons show altered axonal outgrowth (in each case left panels) or affected axon branching behavior (in each case right panels). In (C) representative images of Ighmbp2$^{+/+}$ and Ighmbp2-def. motoneurons at DIV7 are depicted. (D) Ighmbp2-def. motoneurons display no altered axonal elongation (left panel), however an increased branching capacity of Ighmbp2-def. motoneurons can be observed at DIV7. In A, B, and D, axon elongation data are shown as mean±SEM and axon branching data are shown as mean±SD. N defines the number of analyzed cells; n indicates the number of experiments. % means percentage. Modified according to (Surrey et al., 2018).

No alteration in axonal elongation was observed at all three differentiation stages (Fig. 13A-D). Indeed, Ighmbp2-deficient motoneurons exhibited slight but significantly enhanced formation of axon collaterals only observed at DIV7 (Fig. 13C-D), stated by axons with more than three axonal collateral branches and a decreased number of axons without collateral primary branches (Fig. 13C, white arrows and D). At DIV3 and DIV5, no difference of branching behavior was determined (Fig. 13A-B).

As a next step, we focused on the growth cone compartment of Ighmbp2-deficient motoneurons. At DIV5, growth cones of Ighmbp2$^{+/+}$ and Ighmbp2-deficient motoneurons were quantified in size and signal intensity of β-actin protein cultured on laminin-111 (Fig. 14A-C).

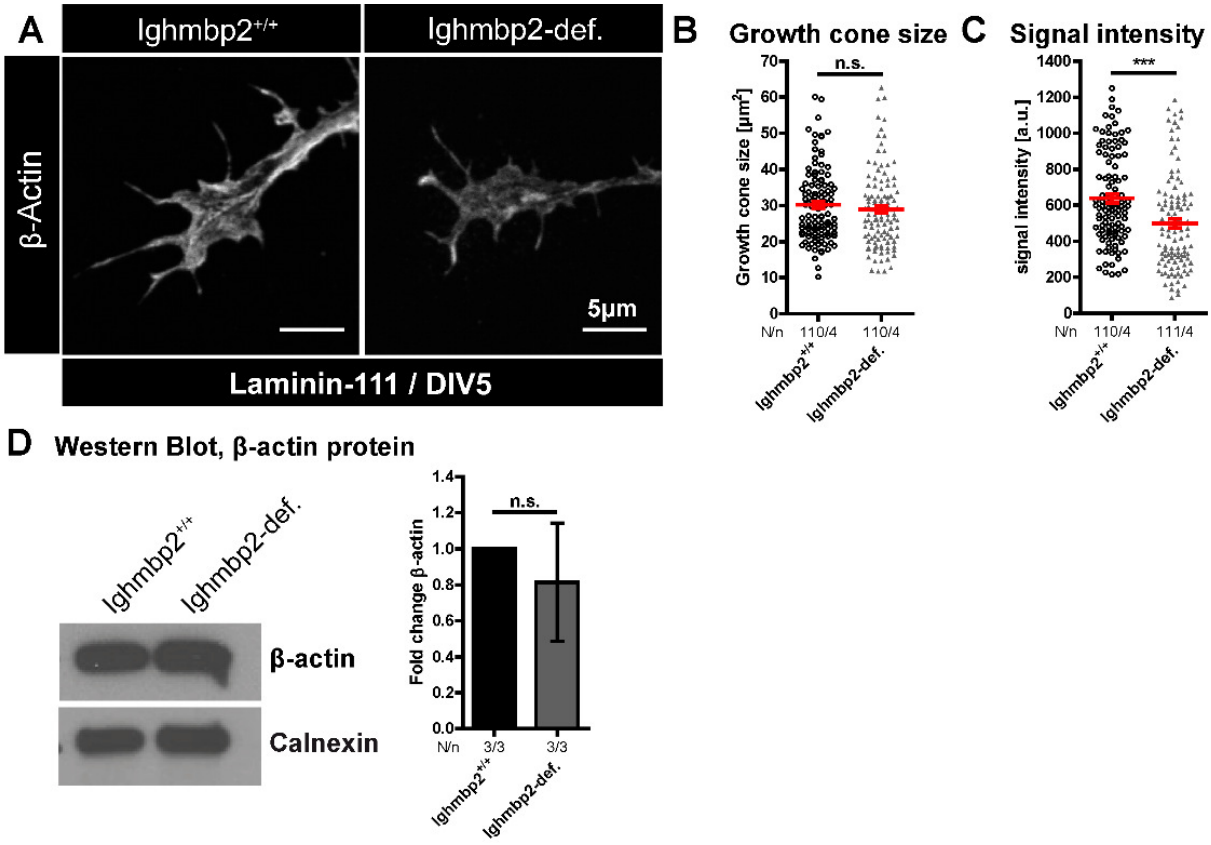

Figure 14 – Growth cones of Ighmbp2-def. motoneurons display reduced β-actin protein intensity cultured on laminin-111 at DIV5. (A) Representative images of β-actin protein in Ighmbp2-def. and Ighmbp2$^{+/+}$ growth cones at DIV5. Quantification of (B) growth cone size and (C) β-actin signal intensity. Ighmbp2-def. motoneurons show no alteration in growth cone size but display a significant reduced β-actin protein signal intensity compared to Ighmbp2$^{+/+}$. (D) Representative Western Blot of β-actin protein in Ighmbp2-def. and Ighmbp2$^{+/+}$ motoneuron lysates (left panel). Quantification of β-actin protein level (right panel). The total amount of β-actin protein of Ighmbp2-def. motoneurons is not affected compared to Ighmbp2$^{+/+}$. In B and C, data are shown as mean±SEM. In D, data are shown as mean±SD. N defines number of analyzed cells (B and C) or number of embryos (D); n indicates the number of experiments. Modified according to (Surrey et al., 2018).

Growth cone size of Ighmbp2-deficient motoneurons showed no alteration (Fig. 14A, B), but the signal intensity exhibited a significant reduction of β-actin protein (Fig. 14A, C) compared to the Ighmbp2$^{+/+}$. Nonetheless, the total β-actin protein amount in whole cell lysates of Ighmbp2-deficient motoneurons was not changed in comparison to the Ighmbp2$^{+/+}$ (Fig. 14D).

Furthermore, growth cones of Ighmbp2$^{+/+}$ and Ighmbp2-deficient motoneurons were quantified in size and signal intensity of α-actin protein at DIV5 (Fig. 15A-C).

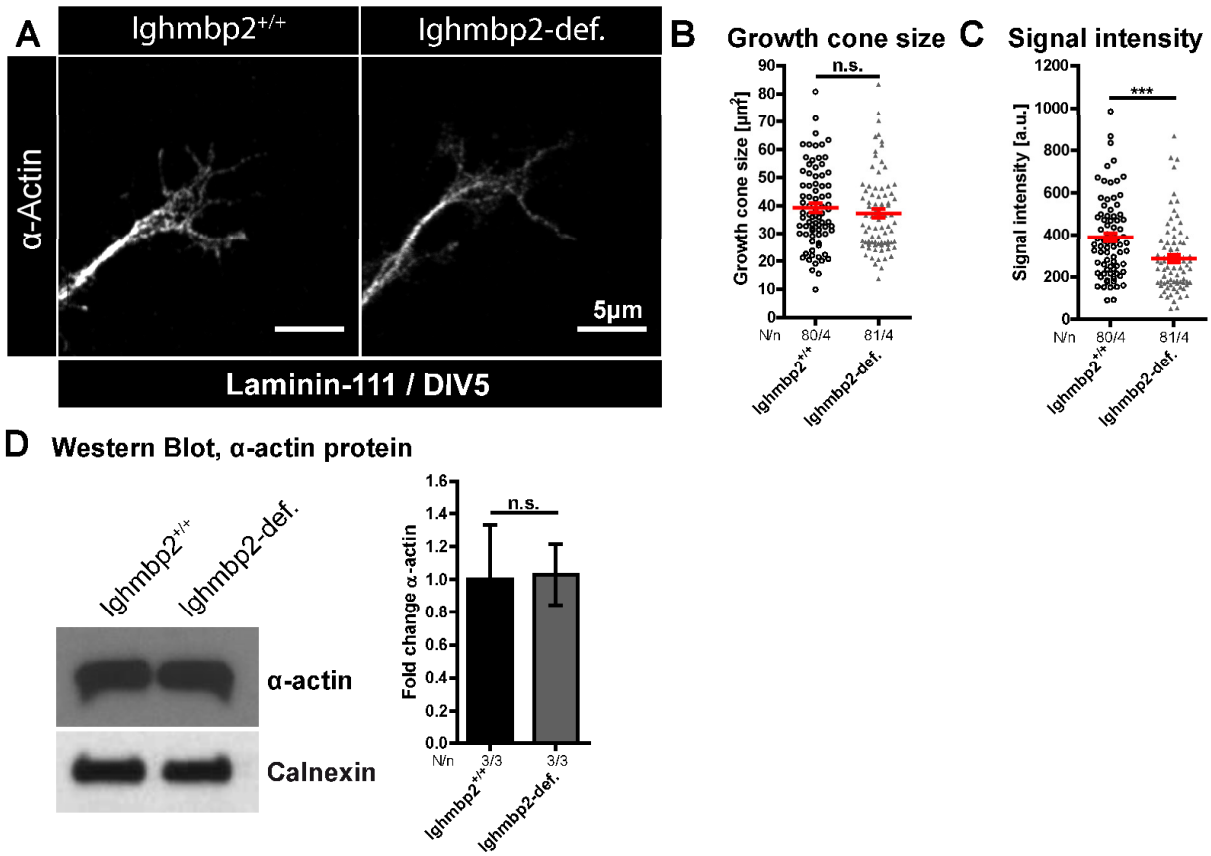

Figure 15 - Growth cones of Ighmbp2-def. motoneurons display reduced α-actin protein intensity cultured on laminin-111 at DIV5. (A) Representative images of α-actin protein in Ighmbp2-def. and Ighmbp2$^{+/+}$ growth cones at DIV5. Quantification of (B) growth cone size and (C) α-actin signal intensity. Ighmbp2-def. motoneurons show no alteration in growth cone size but display a significant reduced α-actin protein signal intensity compared to Ighmbp2$^{+/+}$. (D) Representative Western Blot of α-actin protein in Ighmbp2-def. and Ighmbp2$^{+/+}$ motoneuron lysates (left panel). Quantification of α-actin protein level (right panel). The total amount of α-actin protein of Ighmbp2-def. motoneurons is not affected compared to Ighmbp2$^{+/+}$. In B and C, data are shown as mean±SEM. In D, data are shown as mean±SD. N defines the number of analyzed cells (B and C) or the number of embryos (D); n indicated the number of experiments.

In accordance with β-actin protein quantifications, growth cone size of Ighmbp2-deficient motoneurons showed no alteration (Fig. 15A-B), but the signal intensity exhibited a significant reduction of α-actin protein (Fig. 15A, C) compared to the Ighmbp2$^{+/+}$. Likewise, the total α-actin protein amount in whole cell lysates of Ighmbp2-deficient motoneurons was not changed in comparison to the Ighmbp2$^{+/+}$ (Fig. 15D).

Finally, we performed morphological analyses of the cell body compartment of isolated motoneurons at DIV7 regarding the cell body size, the number of dendrites per cell body, mean dendrite length and total dendrite length (Fig. 16A-E).

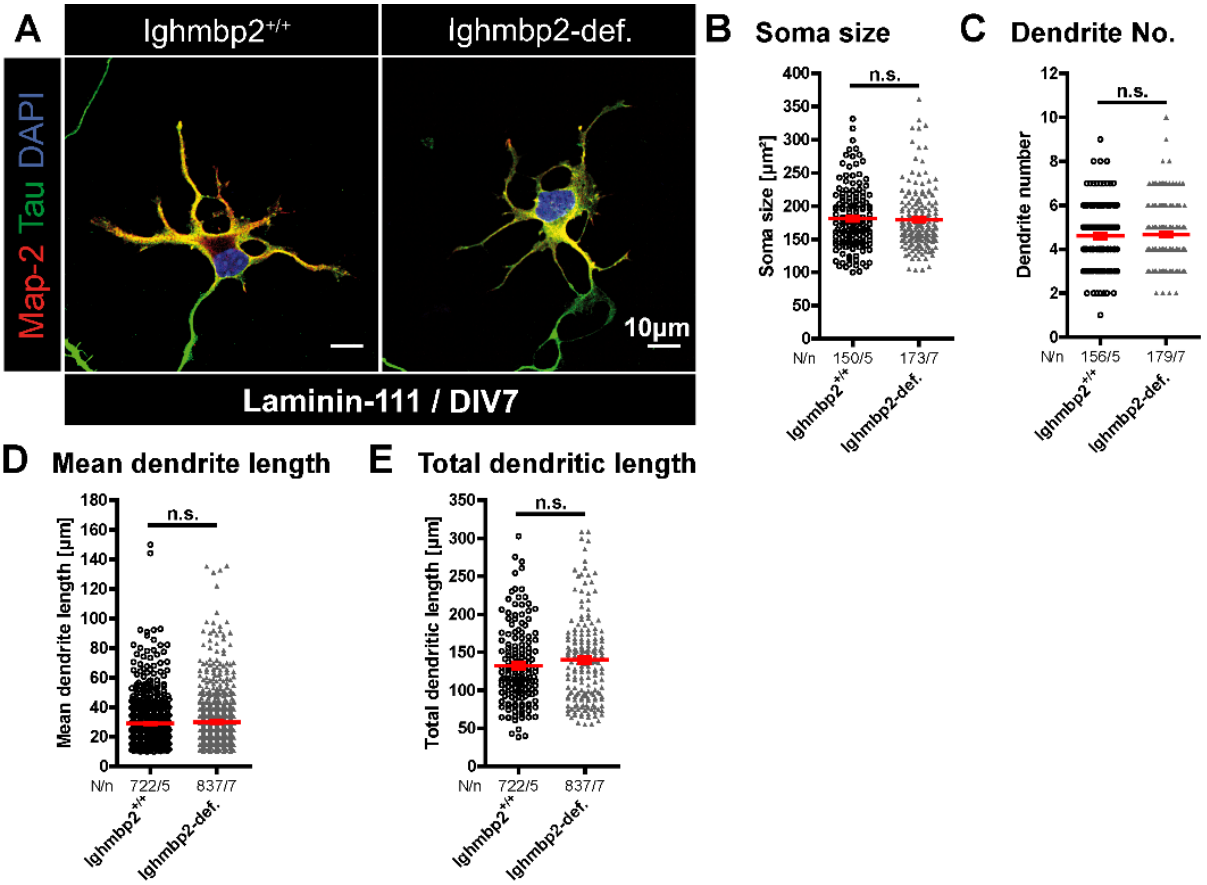

Figure 16 – Morphological analyses of the cell body compartment cultured on laminin-111 at DIV7. (A) Representative images of Ighmbp2-def. and Ighmbp2$^{+/+}$ cell bodies. (B) Cell body size of Ighmbp2-def. and Ighmbp2$^{+/+}$ motoneurons displays no alteration at DIV7. (C) Neither the dendrite number nor (D) the mean dendrite length nor (E) the total dendritic length shows significant differences in Ighmbp2-def. motoneurons compared to Ighmbp2$^{+/+}$. In B-E, data are shown as mean±SEM. N defines number of analyzed cells; n indicates the number of experiments. Modified according to (Surrey et al., 2018).

In this case, no significant alteration was observed between Ighmbp2-deficient and Ighmbp2$^{+/+}$ cell bodies (Fig. 16A-E).

4.2.2 α-/β-actin and Ighmbp2 protein in wildtype (CD1) motoneurons

Studies have already shown that the growth cones in Ighmbp2-deficient motoneurons are smaller and the β-actin protein is underrepresented in this cell compartment (Krieger et al., 2014b). This might have an effect on the biosynthesis of cytoskeletal proteins, such as α- and β-actin, influencing neurite growth and maturation. Therefore, the distribution pattern of α- and β-actin proteins compared to Ighmbp2 protein localization was investigated using immunocytochemical staining. The Co-staining of Ighmbp2 proteins and one of both actin isoforms may give possible hints for physical interaction (Fig. 17).

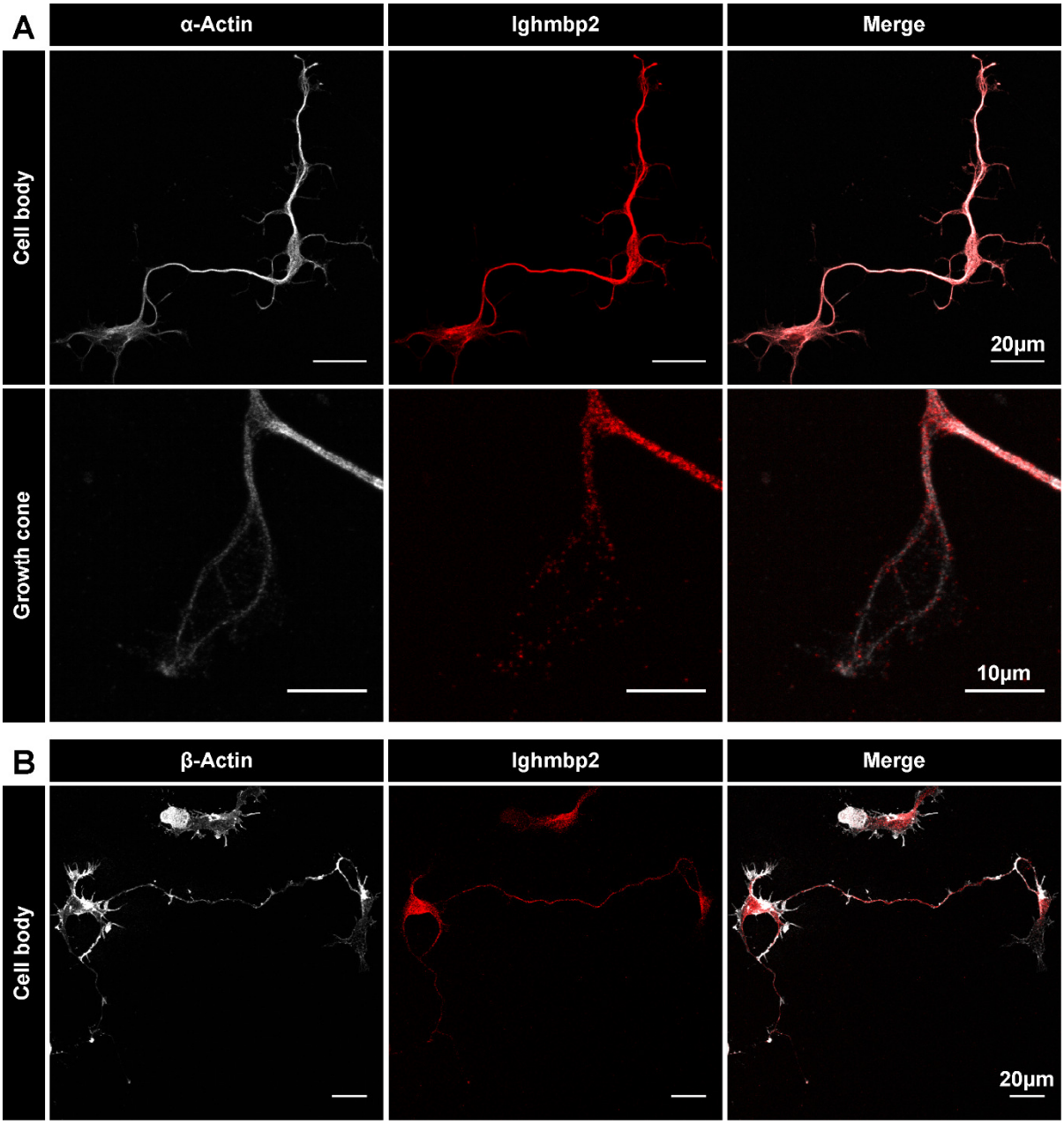

Figure 17 - Localization of α-/β-actin and Ighmbp2 in wildtype motoneurons. Representative images of (A) α-actin and (B) β-actin distribution pattern compared to Ighmbp2 protein localization. (A) α-Actin is evenly distributed, whereas (B) β-actin is predominantly localized in protrusions. Images are made by my former M.Sc. student Caren Zöller. Each experiment was repeated at least 3 times, if not mentioned otherwise.

α-Actin protein was more evenly distributed throughout the cytoplasm of the cell body and localized in the neurites, alongside the axon and axonal branches of motoneurons, but it was higher concentrated in the axon and branch points than in the cell body and growth cones (Fig. 17A). β-Actin protein was predominantly expressed in the protrusions, including the growth cones and axonal branches. It was highly concentrated in the dendritic protrusions. A faint expression of β-actin was found alongside the neurites and in the soma of motoneurons (Fig. 17B). As previously described, Ighmbp2 was predominantly localized in the cytoplasm and in the axons of motoneurons, whereas its expression in the growth cone

was omitted (Fig. 17A). α-Actin and Ighmbp2 proteins were very similar distributed and suggest a co-localization, especially in the distal axon and axonal branches (Fig. 17A).

4.2.3 *β-actin* mRNA level and distribution are not modified in soma and growth cones of Ighmbp2-deficient motoneurons

Because of reduced α- and β-actin protein levels in Ighmbp2-deficient growth cones, we wanted to figure out how Ighmbp2 deficiency impacts the RNA level. For this purpose, we first performed RNA-Sequencing (RNA-Seq) analysis of Ighmbp2-deficient and Ighmbp2$^{+/+}$ motoneurons at DIV7 (Fig. 18A).

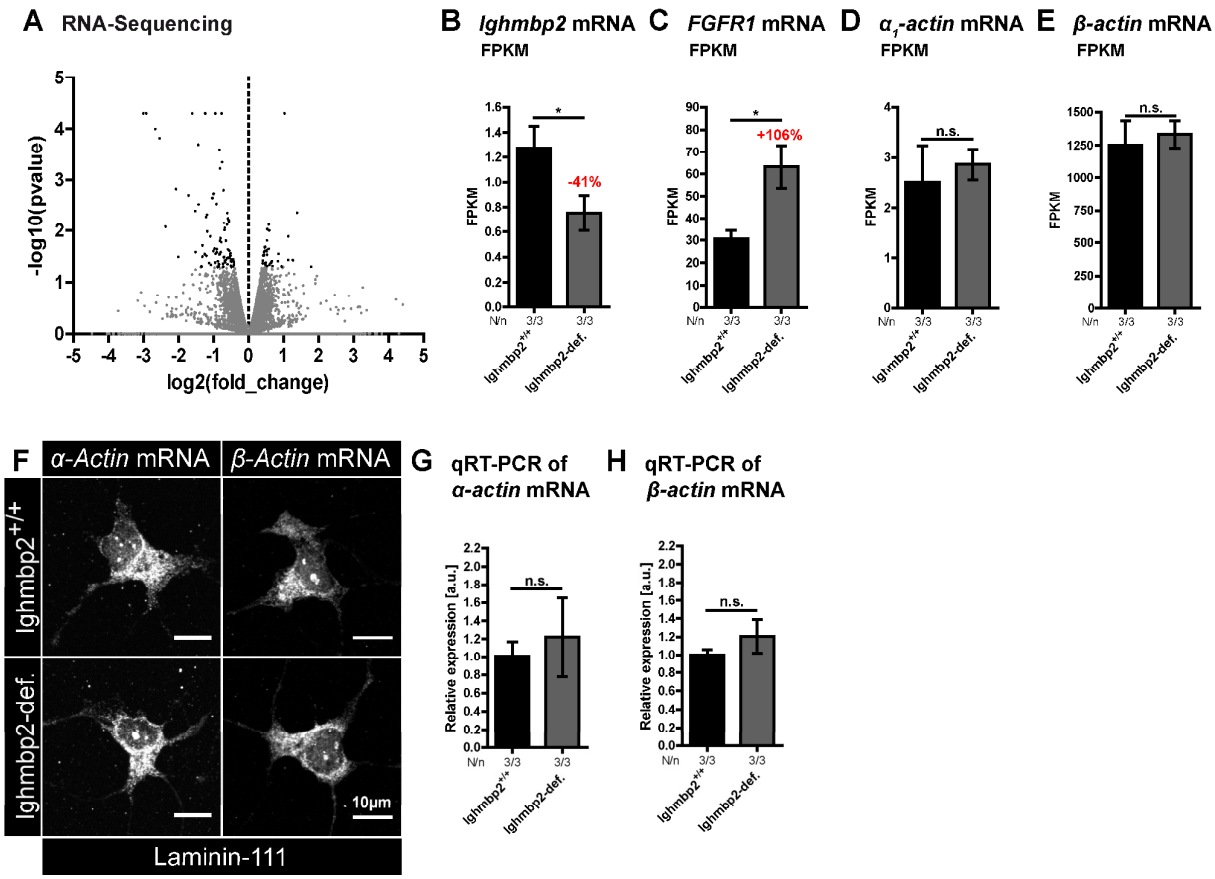

Figure 18 – Ighmbp2-def. motoneurons show significant upregulation of *Fgfr1* but wildtype amount and distribution of *α-* and *β-actin* mRNA. (A) Transcriptome-wide detection of differentially expressed transcripts in Ighmbp2-def. compared to Ighmbp2$^{+/+}$ motoneurons using RNA-Sequencing. The volcano plot displays the significance of change [-log10(pvalue)] vs. the magnitude of change [log2(fold_change)] for each. For better illustration, data points of transcripts with log2(fold_change)<-5 or >5 (all of which were not significantly altered) were left out. FPKM values for (B) *Ighmbp2*, (C) *Fgfr1*, (D) *α-* and (E) *β-actin* mRNA in the Ighmbp2-def. and Ighmbp2$^{+/+}$ datasets. (B) Ighmbp2-def. motoneurons show significant reduction of 41% of *Ighmbp2* mRNA, whereas the *Fgfr1* mRNA is significantly upregulated by 106%. Neither (D) *α-,* nor (E) *β-actin* display an altered mRNA level in Ighmbp2-def. motoneurons compared to Ighmbp2$^{+/+}$ using RNA-Sequencing. RNA-Seq transcript levels are measured as FPKM values (fragments per kilobase transcript per million mapped reads) which are calculated for each given gene by normalizing the number of gene-specific reads to the length of the gene and to the total number of reads mapped. (F) Representative images of *α-* and *β-actin* mRNA in Ighmbp2-def. and Ighmbp2$^{+/+}$ cell bodies cultured on laminin-111 at DIV7 using FISH. Neither (G) *α-,* nor (H) *β-actin* show an altered mRNA level in Ighmbp2-def. motoneurons compared to Ighmbp2$^{+/+}$ using qRT-PCR. In B, C, D, E, G and H, data are shown as mean±SD. N defines the number of embryos; n indicates the number of experiments. Each experiment was repeated at least 3 times, if not mentioned otherwise. Modified according to (Surrey et al., 2018).

No transcripts with a q-value<0.05, but only 123 transcripts with p-value<0,05 were found (Fig. 18A, dark spots). RNA-Seq dataset displayed a significant reduction of 41% Ighmbp2 mRNA, whereas *Fgfr1* transcripts showed significant upregulation of 106% (Fig. 18C). In addition, *α₁*- and *β-actin* transcripts exhibited no alteration in Ighmbp2-deficient motoneurons compared to Ighmbp2$^{+/+}$ (Fig. 18D-E).

FISH also confirmed that *α*- and *β-actin* mRNA in Ighmbp2-deficient motoneurons demonstrated no alterations in distribution pattern or amount (Fig. 18F). On top of that, *α*- and *β-actin* mRNA showed no changes in Ighmbp2-deficient motoneurons compared to the Ighmbp2$^{+/+}$ using qRT PCR quantifications (Fig. 18G, H).

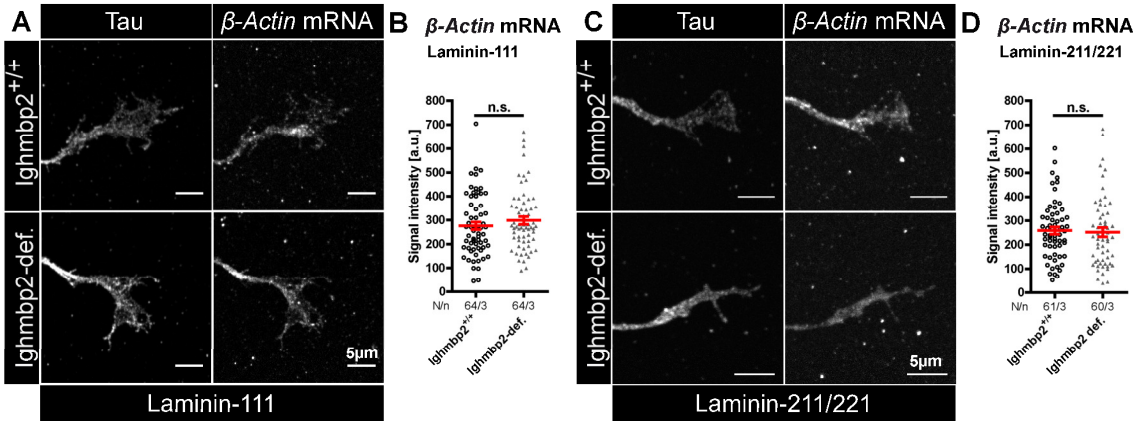

Figure 19 - Ighmbp2-def. motoneurons show wildtype distribution and signal intensity of β-actin mRNA. (A) Representative images of β-actin mRNA in Ighmbp2-def. and Ighmbp2$^{+/+}$ growth cones cultured on laminin-111 at DIV5 using FISH. (B) Quantification of β-actin mRNA signal intensity in growth cones cultured on laminin-111. Ighmbp2-def. motoneurons show no alteration in β-actin mRNA signal intensity compared to Ighmbp2$^{+/+}$. (C) Representative images of β-actin mRNA in Ighmbp2-def. and Ighmbp2$^{+/+}$ growth cones cultured on laminin-211/221 at DIV5 using FISH. (D) Quantification of β-actin mRNA signal intensity in growth cones cultured on laminin-211/221. Ighmbp2-def. motoneurons display no changed β-actin mRNA signal intensity compared to Ighmbp2$^{+/+}$. In B and D, data are shown as mean±SEM. N defines the number of analyzed cells; n indicates the number of experiments. Modified according to (Surrey et al., 2018).

In addition, we analyzed the signal intensity of *β-actin* mRNA in growth cones of Ighmbp2-deficient motoneurons cultured on laminin-111 and laminin-211/221 using fluorescence *in situ* hybridization (FISH) at DIV5. Neither on laminin-111 (Fig. 19A-B) nor on laminin-211/221 (Fig. 19C-D), Ighmbp2-deficient motoneurons exhibited differences in *β-actin* mRNA level compared to Ighmbp2$^{+/+}$ (Fig. 19B, D). Thus, no strong global effect at mRNA level in Ighmbp2-deficient motoneurons was detectable.

4.2.4 Local translation of eGFP^{myr}-β-actin 3'UTR reporter is delayed in Ighmbp2-deficient motoneurons

Despite *β-actin* mRNA not being affected, we wanted to figure out whether the local translation of β-actin is changed upon Ighmbp2 deficiency. For this purpose, we performed Fluorescence Recovery after Photobleaching (FRAP) experiments to analyze the local translation of β-actin in growth cones (Fig. 20A-D) and cell bodies (Fig. 21A-B) of Ighmbp2-deficient and Ighmbp2$^{+/+}$ motoneurons at DIV5.

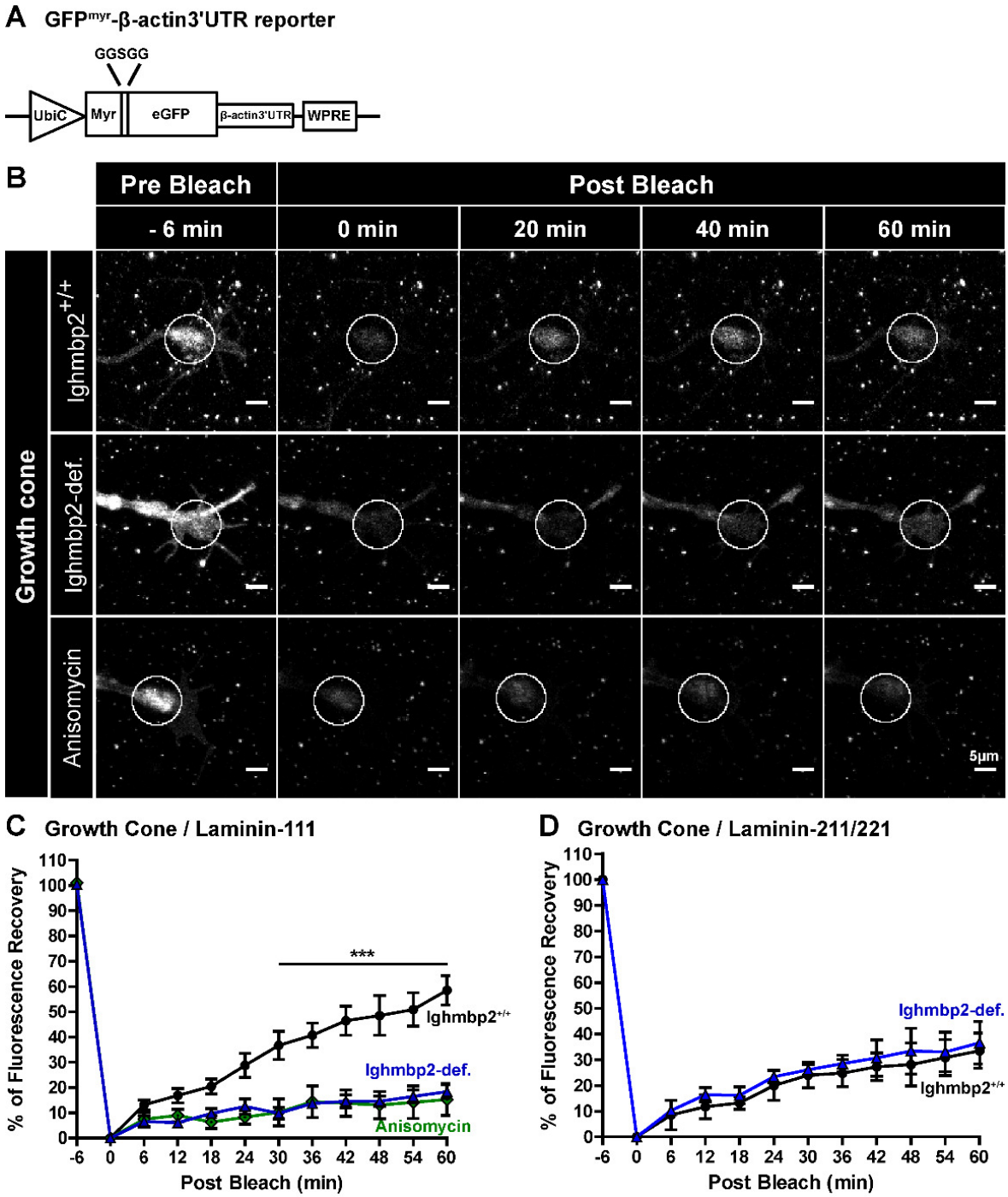

Figure 20 - Delayed synthesis of β-actin reporter in the growth cones of Ighmbp2-def. motoneurons cultured on laminin-111, but no effect in synthesis cultured on laminin-211/221. (A) Scheme of eGFP^{myr}-β-actin 3'UTR. (B) Representative time-lapse images from fluorescence recovery after photobleaching (FRAP) in growth cones of eGFP^{myr}-β-actin 3'UTR-expressing Ighmbp2$^{+/+}$ and Ighmbp2-def. motoneurons at DIV5. eGFP^{myr} was bleached and fluorescence recovery was recorded in a specific region of interest (indicated with white circles) within the growth cones. (C) Quantification of FRAP shows a significant reduction in growth cones cultured on laminin-111 (n=6 Ighmbp2$^{+/+}$ and n=7 Ighmbp2-def. motoneurons) but shows no effect in the translation of eGFP^{myr}-β-actin 3'UTR reporter of Ighmbp2-def. motoneurons cultured on laminin-211/221 (n=4 Ighmbp2$^{+/+}$ and n=3 Ighmbp2-def. motoneurons). (B-C) In control experiments, translation of eGFP^{myr}-β-actin 3'UTR reporter is inhibited using anisomycin indicating that the recovery is due to the *de novo* synthesized proteins. In B and C, data are shown as mean±SEM. % means percentage. Modified according to (Surrey et al., 2018).

After 5 days *in vitro,* eGFP^{myr} lentiviral reporter construct (Fig. 20A) transfected Ighmbp2-deficient and Ighmbp2$^{+/+}$ motoneurons were bleached and increasing eGFP^{myr} fluorescence recovery was monitored in growth cones for 1h after photobleaching (Fig. 20B).

Quantifications of FRAP analyses in defined regions of interest (ROI; indicated with white circles) exhibited a significant reduction in fluorescence recovery in growth cones (Fig. 20B, C) of Ighmbp2-deficient motoneurons compared to the Ighmbp2$^{+/+}$ cultured on laminin-111, whereas the translation of eGFP^{myr}- β-actin 3'UTR reporter in Ighmbp2-deficient motoneurons cultured on laminin-211/221 was not affected (Fig. 20D). Essentially, it was observed that the local translation in the growth cones cultured on Laminin-211/221 was reduced compared to Laminin-111 (Fig. 20C-D). As a control experiment, eGFP^{myr} lentiviral reporter construct (Fig. 20A) transfected motoneurons were pre-treated with the translation blocker anisomycin which induced blocked recovery of eGFP^{myr}- β-actin 3'UTR reporter and proved increasing fluorescence recovery is due to the synthesis of newly synthesized protein and not caused by its diffusion (Fig. 20B-C).

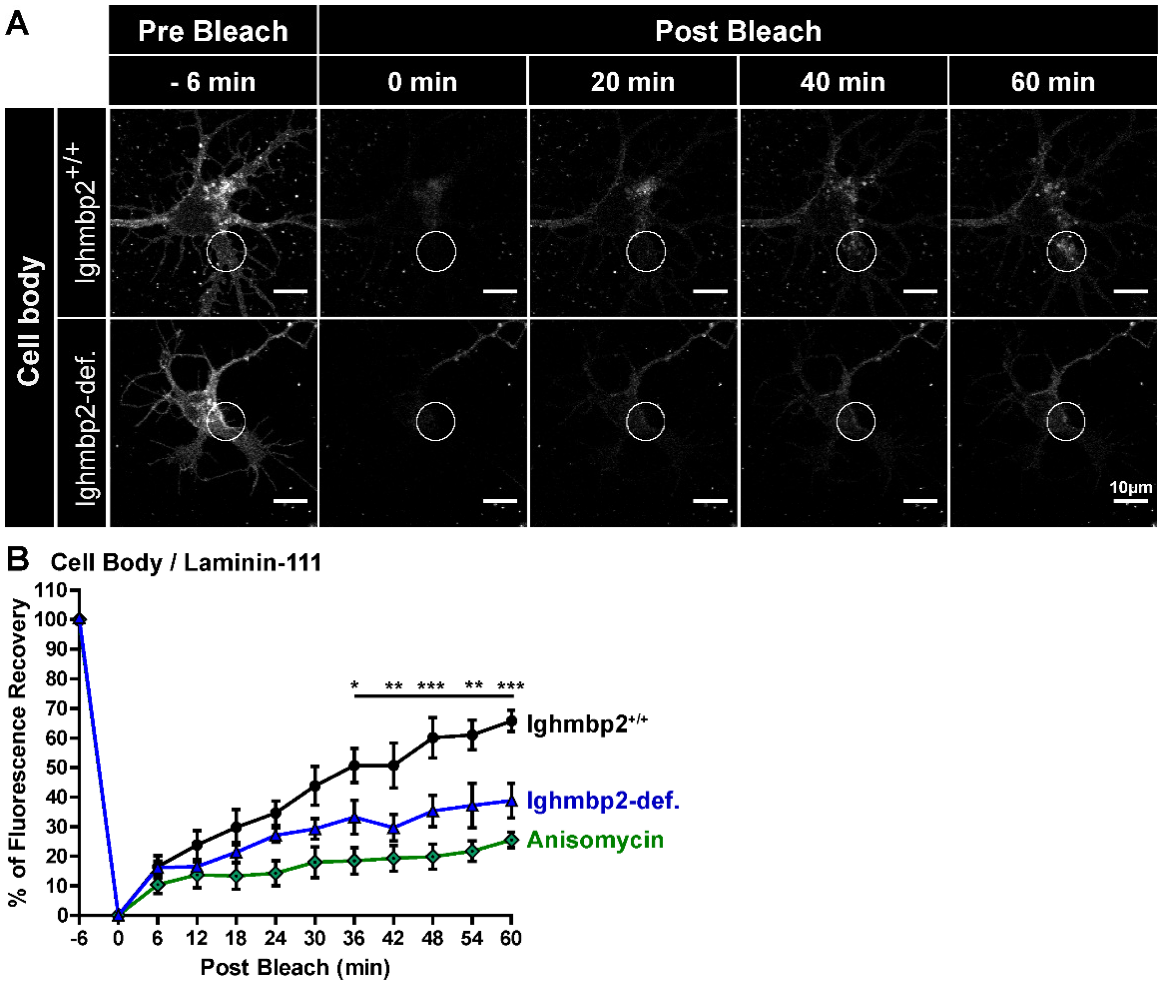

Figure 21 - Delayed synthesis of β-actin reporter in the cell body of Ighmbp2-def. motoneurons cultured on laminin-111. (A) Representative time-lapse images from fluorescence recovery after photobleaching (FRAP) in cell body of eGFP^{myr}-β-actin 3'UTR-expressing Ighmbp2$^{+/+}$ and Ighmbp2-def. motoneurons at DIV5. eGFP^{myr} was bleached and fluorescence recovery was recorded in a specific region of interest (indicated with white circles) within the cell bodies. (C) Quantification of FRAP shows significant reduction of the translated eGFP^{myr}-β-actin 3'UTR reporter in cell body cultured on laminin-111 (n=4 Ighmbp2$^{+/+}$ and n=7 Ighmbp2-def. motoneurons). In control experiments, translation of eGFP^{myr}-β-actin 3'UTR reporter is inhibited using anisomycin indicating that the recovery is due to the *de novo* synthesized proteins. In B, data are shown as mean±SEM. % means percentage. Modified according to (Surrey et al., 2018).

In addition, Ighmbp2-deficient and Ighmbp2$^{+/+}$ cell bodies were bleached and increasing eGFP^{myr} fluorescence recovery was monitored for 1h after photobleaching (Fig. 21A). Likewise, quantifications of FRAP analyses in defined regions of interest (ROI; indicated by white circles) showed a significant reduction in fluorescence recovery in cell bodies of Ighmbp2-deficient motoneurons compared to the Ighmbp2$^{+/+}$ cultured on laminin-111 (Fig. 21B).

4.2.5 Minor quantitative differences of *de novo* synthesized proteins in Ighmbp2-deficient motoneurons

Time-lapse imaging study via fluorescence recovery after photobleaching (FRAP) visualized a local translation delay of an eGFP^{myr}- β-actin 3'UTR mRNA in growth cones and cell bodies from Ighmbp2-deficient motoneurons cultured on laminin-111. This observation raised the question whether Ighmbp2 deficiency leads to a general alteration of *de novo* synthesized proteins. To investigate newly synthesized proteins, we established a pSILAC protocol in Ighmbp2-deficient motoneurons compared to Ighmbp2$^{+/+}$. Since the generated amount of motoneurons per embryo is deeply limited and the mortality rate is significantly increased during cultivation, the pSILAC analysis was performed at DIV3. Incorporated heavy and medium-heavy amino acids in *de novo* translated proteins of Ighmbp2-deficient and Ighmbp2$^{+/+}$ motoneurons were analyzed by mass spectrometry of resulting mass differences.

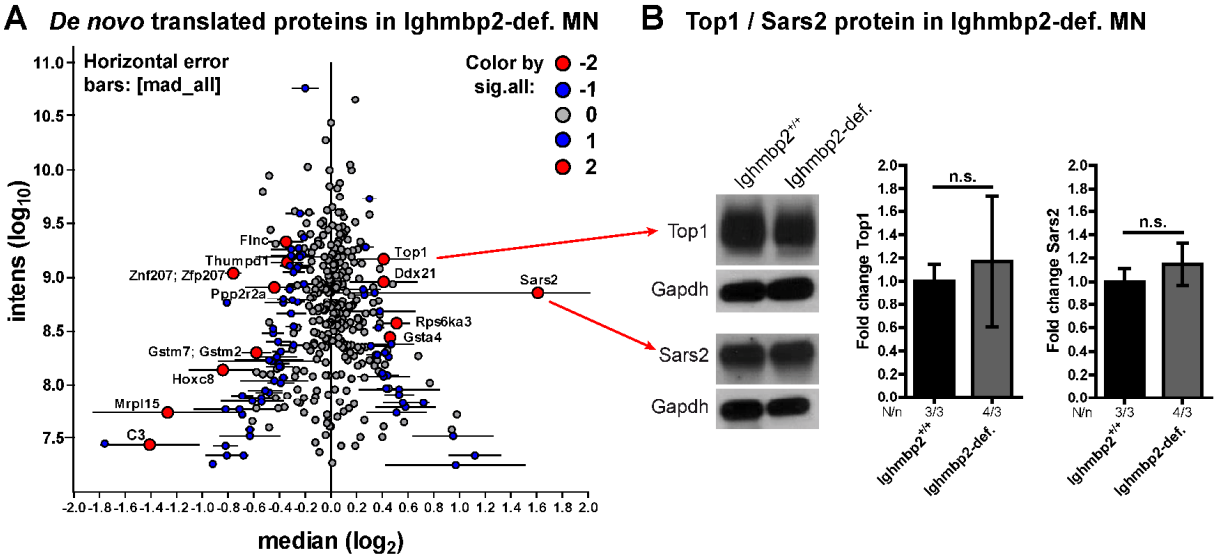

C Up-or down-regulation of labeled pSILAC-proteins in Ighmbp2-def. MN

Gene names	p-values	median (FC/log_2)	mad_all	intens (log_{10})	sig.all
Sars2	0,84	1,61	1,80	8,86	2 (down)
Rps6ka3	0,84	0,51	0,10	8,57	2 (down)
Gsta4	0,81	0,46	0,01	8,44	2 (down)
Top1	0,84	0,41	0,20	9,17	2 (down)
Ddx21	0,81	0,41	0,26	8,96	2 (down)
Thumpd1	0,81	-0,34	0,12	9,14	-2 (up)
Flnc	0,87	-0,35	0,13	9,33	-2 (up)
Ppp2r2a	0,81	-0,44	0,22	8,91	-2 (up)
Gstm7; Gstm2	0,81	-0,58	0,11	8,30	-2 (up)
Znf207; Zfp207	0,65	-0,76	0,06	9,04	-2 (up)
Hoxc8	0,81	-0,84	0,26	8,14	-2 (up)
Mrpl15	0,81	-1,27	0,58	7,74	-2 (up)
C3	0,81	-1,41	0,38	7,44	-2 (up)

Figure 22 – Minor quantitative differences of *de novo* synthesized proteins in Ighmbp2-def. motoneurons using pSILAC. (A) Quantification of *de novo* translated proteins of Ighmbp2-def. motoneurons compared to Ighmbp2$^{+/+}$. Ighmbp2 deficiency causes only few up- or down-regulated proteins in comparison with Ighmbp2$^{+/+}$ at DIV3 (highlighted in red and blue). (B) Representative Western Blot of Top1 and Sars2 in Ighmbp2-def. and Ighmbp2$^{+/+}$ motoneuron lysates (left panel). Quantifications of Top1 (middle panel) and Sars2 (right panel) protein level. The total amount of both proteins in Ighmbp2-def. motoneurons is not altered compared to Ighmbp2$^{+/+}$. (C) List of up- or down-regulated labeled pSILAC proteins in Ighmbp2-def. motoneurons compared to Ighmbp2$^{+/+}$ (in A, highlighted in red). *De novo* synthesized proteins display no significant up- or down-regulation ($p>0.05$) in two out of three independent experiments (2/-2). In A, data are shown as median±horizontal error bars. In B, data are shown as mean±SD. N defines the number of embryos; n indicates the number of experiments. Each experiment was repeated at least 3 times, if not mentioned otherwise. MN means motoneurons and FC means fold change. Modified according to (Surrey et al., 2018).

Quantification of pSILAC approach displayed only slight alteration by up- and down-regulation of newly synthesized proteins in Ighmbp2-deficient motoneurons (MN) (Fig. 22A, highlighted in blue and red dots). Verification of two down-regulated proteins was performed using Western blot analysis at DIV7. No alterations of DNA topoisomerase 1 (Top1) and mitochondrial Serine-tRNA ligase (Sars2) in Ighmbp2-deficient motoneurons were detectable (Fig. 22B). Up- and down-regulated proteins in two out of three independent experiments were listed in Fig. 22C and highlighted in Fig. 22A in red.

For further investigation regarding protein synthesis, we performed two translation technologies, AHA-Labeling (Fig. 23A-C) and SUnSET (Fig. 23D).

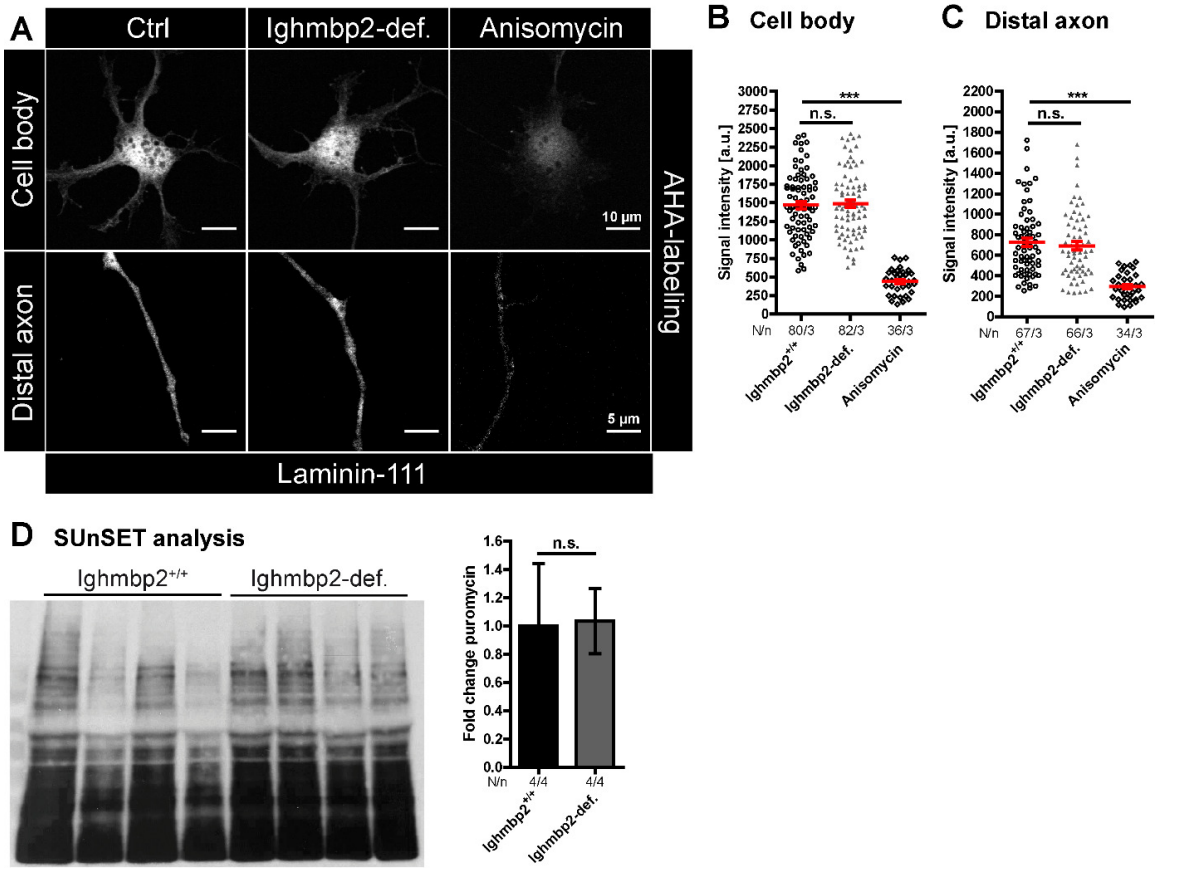

Figure 23 – No alteration of newly translated protein in Ighmbp2-def. motoneurons using AHA labeling and SUnSET analysis. (A) Representative images of *de novo* synthesized proteins 20h labeled with L-azidohomoalanine (AHA) in Ighmbp2-def. and Ighmbp2$^{+/+}$ cell bodies and distal axons. Quantifications of AHA signal intensity in (B) cell bodies and (C) distal axons of Ighmbp2-def. and Ighmbp2$^{+/+}$ motoneurons. (B) Neither the cell body nor (C) the distal axon shows significant differences in *de novo* synthesized AHA-labelled proteins of Ighmbp2-def. motoneurons compared to Ighmbp2$^{+/+}$. (D) Representative Western Blot of surface sensing of translation technology (SUnSET) in Ighmbp2-def. and Ighmbp2$^{+/+}$ motoneurons at DIV7. Puromycin incorporation during 1h of incubation shows no alteration in both conditions. In B-C, data are shown as mean±SEM. In D, data are shown as mean±SD. N defines the number of analyzed cells (B-C) or the number of embryos (D); n indicates the number of experiments. Ctrl means control. Modified according to (Surrey et al., 2018).

After 20h of AHA-labeling, the distribution and amount of newly synthesized proteins in the cell bodies and distal axons were quantified in Ighmbp2-deficient and Ighmbp2$^{+/+}$. In both cell compartments, no alterations in protein synthesis and distribution pattern were detectable (Fig. 23A-C). SUnSET analysis was performed to measure the efficiency of protein synthesis in whole cell lysates. Neither Ighmbp2-deficient nor Ighmbp2$^{+/+}$ motoneurons showed reduced puromycin incorporation during 1h incubation (Fig. 23D). Ighmbp2 deficiency showed no global changes in protein synthesis using both approaches (Fig. 23A-D) and caused only marginal impairment of *de novo* synthesis in primary cultured motoneurons.

4.3 RNA binding Capacity of Ighmbp2 Protein

Most of the results from section 4.3 are published in (Surrey et al., 2018). As previously described, Ighmbp2 is an RNA/DNA helicase which can unwind RNA duplices (Guenther et al., 2009a). Based on sequence homology, IGHMBP2 has been classified as a member of the UPF1-like group within the helicase superfamily 1. Ighmbp2 seems to be functionally linked to pre-mRNA splicing/translation, DNA replication and tRNA processing (Jankowsky, 2011).

4.3.1 Ighmbp2 binds only few RNAs

To test whether Ighmbp2 influences translation caused by RNA binding, we performed a radioactive labeling of cross-linked protein-RNA complexes in HEK293 cells. With the help of this approach, we were able to visualize the general binding of Ighmbp2 to RNAs.

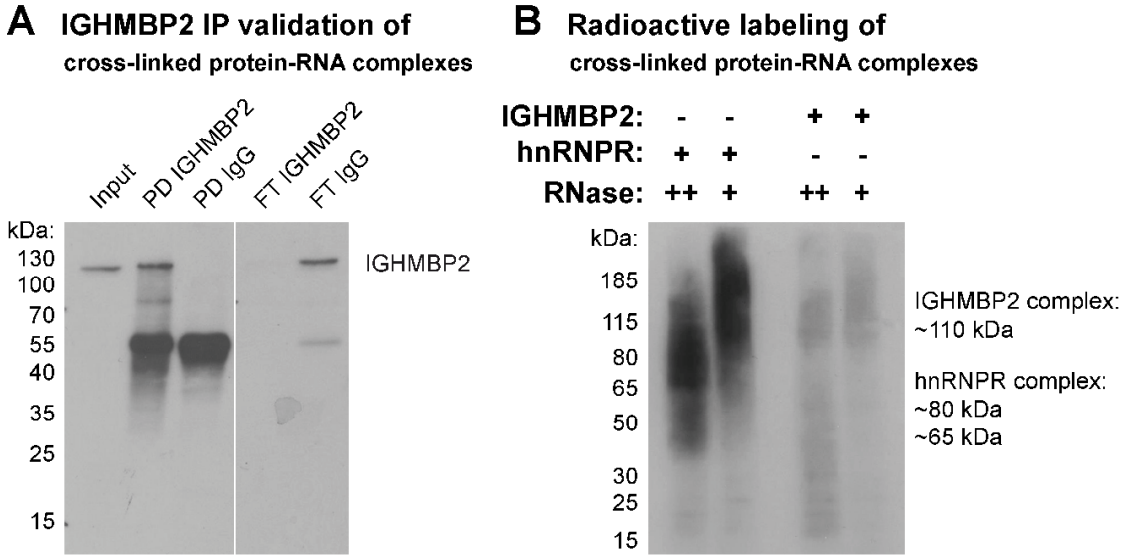

Figure 24 – IGHMBP2 binds only few RNAs. (A) Representative Western Blot of IGHMBP2 immunoprecipitation (IP) to verify the successful pulldown (PD) of IGHMBP2. Rabbit IgG antibody IP is free of target protein, only the heavy chain of rabbit IgG antibodies are detectable. Pulldown efficiency is almost 100%, flow-through (FT) shows no IGHMBP2 protein (fourth panel/FT IGHMBP2). (B) Radioactive labeling of cross-linked IGHMBP2- and hnRNPR-RNA complexes. As a positive control, hnRNPR was used. hnRNPR complex is detectable at 65 and 80kDa (first panel) and RNA binding is observed above (second panel). Ighmbp2 complex is weakly expressed at 110kDa (third panel) followed by a faint RNA binding capacity (fourth panel). Each experiment was repeated at least 3 times, if not mentioned otherwise. FT means flow-through.

IGHMBP2 pulldown (PD) validation was done by Western blot analysis (Fig. 24A). The positive control hnRNPR was used to confirm the radioactive labeling. With a high concentration of RNase enzyme, the hnRNPR complex was visible at 80 and 65kDa (Fig. 24B, first panel). Above these bands and at low RNase concentration, the smear confirmed RNA binding to the hnRNPR protein (Fig. 24B, second panel). In contrast to the positive control, IGHMBP2 complex with high RNase concentration was only weakly visible at 110kDa (Fig. 24B, third panel). RNA binding to IGHMBP2 was found very faintly because

the smear was only poorly detectable (Fig. 24B, fourth panel). These data suggested that IGHMBP2 binds only few RNAs.

4.3.2 Ighmbp2 does not directly bind to *β-actin* mRNA

To verify whether the delay of local translation of β-actin protein in Ighmbp2-deficient cell bodies and growth cones is caused by a direct interaction of *β-actin* mRNA to Ighmbp2 protein, we performed immunoprecipitation (IP) of mRNA-protein complexes (RIP) analyses. It is already known that Insulin-like growth factor-2 mRNA- binding protein 1 (IMP1) is directly associated with *β-actin* mRNA (Farina et al., 2003; Huttelmaier et al., 2005). On this account, RIP analysis was performed with IMP1 as a positive pulldown (PD) control in comparison to IgG as a negative PD control in HEK293 cells.

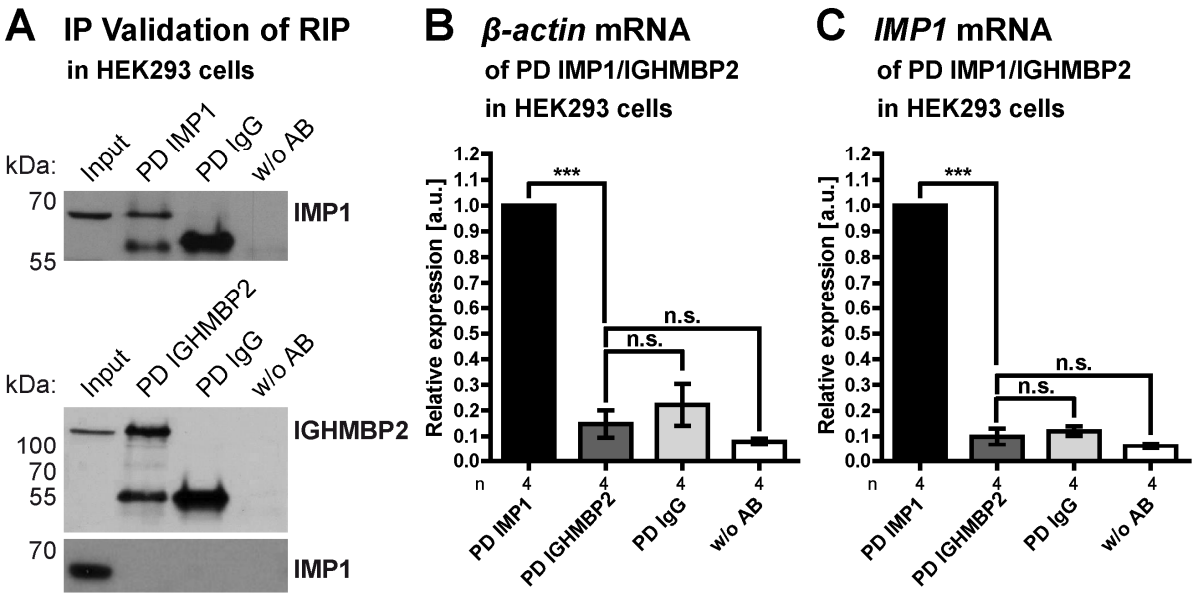

Figure 25 – IGHMBP2 does not directly bind to *β-actin* mRNA but IMP1 interacts with its own mRNA. (A) Representative Western Blot of IMP1- and IGHMBP2-immunoprecipitation (IP) of RIP to verify the successful pulldown (PD) of IMP1 and IGHMBP2. Rabbit IgG antibody IP is free of both target proteins, only the heavy chain of rabbit IgG antibodies is detectable. No protein is visible when antibodies are omitted (w/o AB). Co-IP of IGHMBP2 and IMP1 (lower panel) shows no direct protein-protein interaction of both proteins. qRT-PCR for (B) *β-actin*, and (C) *IMP1* mRNA of immunoprecipitated IMP1 and IGHMBP2 were performed. (B) Relative *β-actin* mRNA expression of IGHMBP2 in comparison to IMP1 shows that IGHMBP2 does not directly bind to *β-actin* mRNA. (C) Relative *IMP1* mRNA expression of IGHMBP2 in comparison to IMP1 shows that IGHMBP2 does not directly bind to *IMP1* mRNA, whereas IMP1 protein binds its own mRNA. Absolute copy numbers of target mRNA of *IMP1* and *β-actin* are normalized to absolute copy numbers of target mRNA of input and IgG control condition. In B and C, IMP1 as positive control is normalized to 1. In B-C, data are shown as mean±SD. n indicates the number of experiments. w/o AB means without antibody. Modified according to (Surrey et al., 2018).

IGHMBP2 and IMP1 PD validation of RIP was done by Western blot analyses (Fig. 25A, upper and middle panel). In addition, a Co-IP of IGHMBP2 and IMP1 showed that both proteins did not directly interact with each other (Fig. 25A, lower panel). Possible *β-actin* mRNA interaction with immunoprecipitated IMP1 and IGHMBP2 was quantified by quantitative Realtime-PCR (qRT-PCR) (Fig. 25B). These data showed no direct binding of *β-actin* mRNA to IGHMBP2 protein, whereas IMP1 protein has bound to *β-actin* mRNA (Fig. 25B).

Furthermore, a possible interaction of *IMP1* mRNA with the immunoprecipitated IMP1 and IGHMBP2 was conducted by qRT-PCR (Fig. 25C). A direct interaction between *IMP1* mRNA and its protein was observed whereas Ighmbp2 protein showed no direct binding to *IMP1* mRNA (Fig. 25C).

4.4 Imp1 and Fgfr1 as affected Target Proteins in Ighmbp2-deficient Motoneurons

Some of the results from section 4.4 are published in (Surrey et al., 2018). Based on previously described results, two affected target proteins, Insulin-like growth factor-2 mRNA- binding protein 1 (Imp1) and fibroblast growth factor receptor 1 (Fgfr1) could be discovered in Ighmbp2-deficient motoneurons and are investigated below.

4.4.1 Ighmbp2 deficiency causes reduced Insulin-like growth factor-2 mRNA- binding protein 1 (Imp1) level in isolated motoneurons

To determine whether *β-actin* mRNA transport is disturbed by its primary RNA-binding partner Imp1, we quantified Imp1 mRNA and protein level in Ighmp2-deficient motoneurons (Fig. 26).

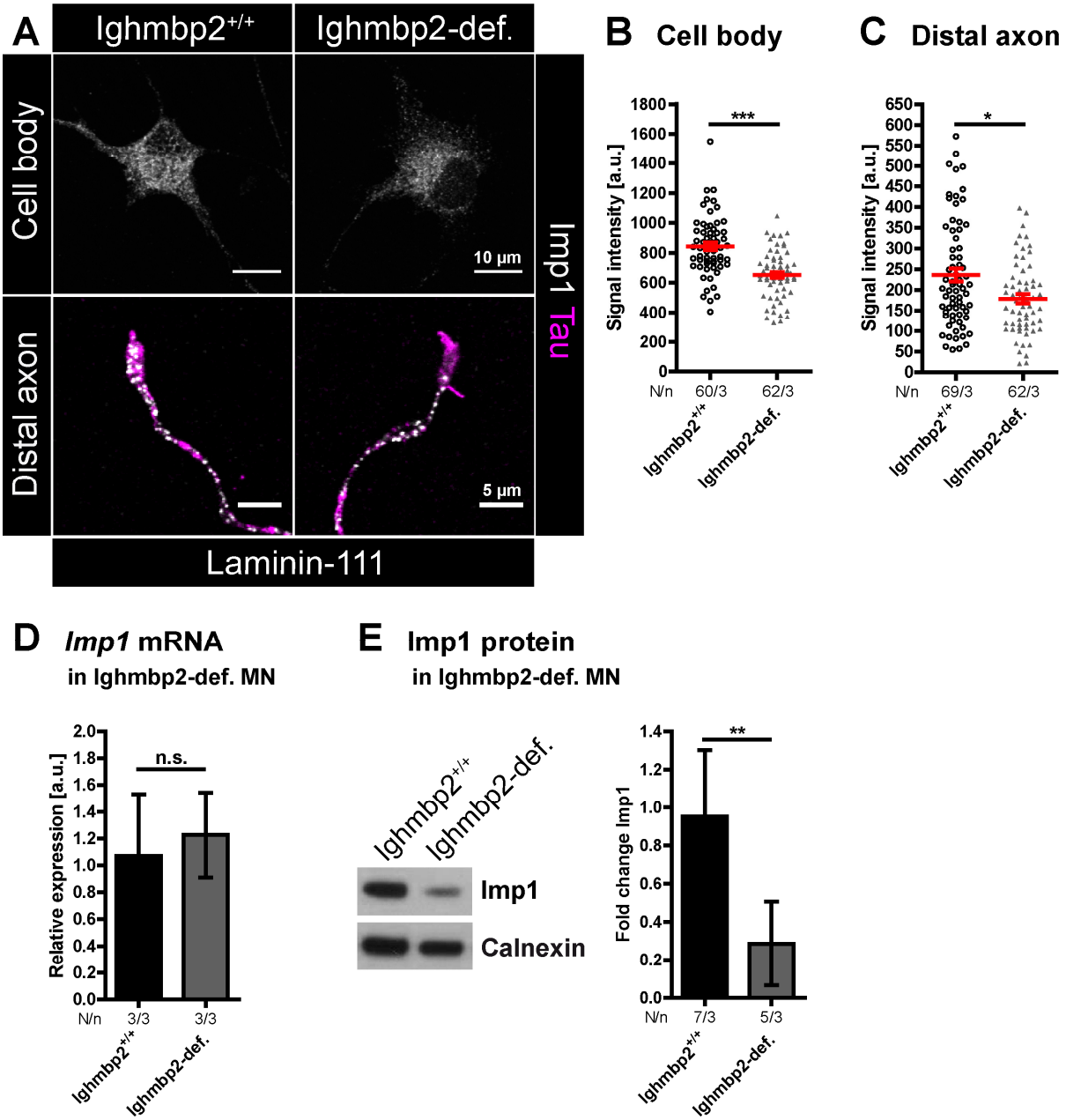

Figure 26 - Amount and distribution of Imp1 mRNA and protein in Ighmbp2-def. motoneurons cultured on laminin-111. (A) Representative images of Imp1 protein distribution in Ighmbp2-def. and Ighmbp2$^{+/+}$ cell bodies and distal axons. Quantification of the (B) cell body and the (C) distal axon in Ighmbp2-def. motoneurons compared to Ighmbp2$^{+/+}$. In both cell compartments, Imp1 signal intensity is significantly reduced in Ighmbp2-def. motoneurons in comparison to Ighmbp2$^{+/+}$. (D) *Imp1* mRNA is not altered in Ighmbp2-def. motoneurons compared to Ighmbp2$^{+/+}$ using qRT-PCR. (E) Representative Western Blot of Imp1 protein in Ighmbp2-def. and Ighmbp2$^{+/+}$ motoneuron lysates (left panel). Quantification of Imp1 protein level (right panel). The total amount of Imp1 protein of Ighmbp2-def. motoneurons is significantly reduced compared to Ighmbp2$^{+/+}$. In B-C, data are shown as mean±SEM. In D-E, data are shown as mean±SD. N defines the number of analyzed cells (B-C) or the number of embryos (D-E); n indicates the number of experiments. Modified according to (Surrey et al., 2018).

First, the distribution and signal intensity of IMP1 protein in Ighmbp2-deficient and Ighmbp2$^{+/+}$ cell bodies and distal axons were investigated. In both cell compartments, a significant reduced Imp1 signal intensity was observed in Ighmbp2-deficient motoneurons in comparison to the Ighmbp2$^{+/+}$ (Fig. 26A-C). *Imp1* mRNA showed no changes using qRT-PCR quantification (Fig. 26C). However, the protein level of Imp1 was significantly reduced in whole cell lysates of Ighmbp2-deficient motoneurons compared to the Ighmbp2$^{+/+}$ (Fig. 26D).

Thus, we detected reduced β-actin protein level at the growth cone of Ighmbp2-deficient motoneurons which was accompanied by reduced levels of Imp1, an interactor of *β-actin* mRNA.

To verify whether Imp1 protein (Fig. 26E) influences *Fgfr1* transcript level (Fig. 18C) caused by Ighmbp2 deficiency, we performed RIP analyses regarding *FGFR1* mRNA and IMP1/IGHMBP2 protein.

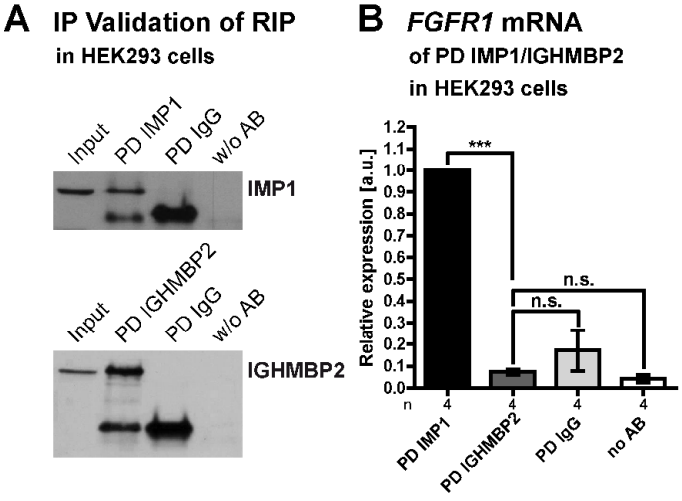

Figure 27 – IMP1 protein binds to *FGFR1* mRNA. (A) Representative Western Blot of IMP1- and IGHMBP2-immunoprecipitation (IP) of RIP for validation of the pulldown (PD). (B) qRT-PCR for *FGFR1* mRNA of immunoprecipitated IMP1 and IGHMBP2 were quantified. Relative *FGR1* mRNA expression of IGHMBP2 in comparison to IMP1 shows that IGHMBP2 does not directly bind to *FGFR1* mRNA, whereas IMP1 shows a direct interaction with *FGFR1* mRNA. In B, data are shown as mean±SD. n indicated the number of experiments. w/o AB means without antibody.

Possible *FGFR1* mRNA interaction with immunoprecipitated IMP1 and IGHMBP2 protein was quantified by qRT-PCR (Fig. 27B). These data showed no direct binding of *FGFR1* mRNA to IGHMBP2 protein, whereas IMP1 protein bound to *FGFR1* mRNA (Fig. 27B). IGHMBP2 and IMP1 PD validation of RIP was done by Western blot analyses (Fig. 27A).

4.4.2 Ighmbp2 deficiency causes reduced fibroblast growth factor receptor 1 (Fgfr1) level in isolated motoneurons

RNA-Sequencing data have shown that *Fgfr1* is significantly upregulated in Ighmbp2-deficient motoneurons compared to Ighmbp2$^{+/+}$ (Fig. 18A, C). This observation was also confirmed by an increased expression in *Fgfr1* mRNA using qRT-PCR (Fig. 28A). In order to analyze whether the changed mRNA level of *Fgfr1* in Ighmbp2-deficient motoneurons is also detectable on the protein level, quantification of Fgfr1 protein amount was performed using Western blot analysis.

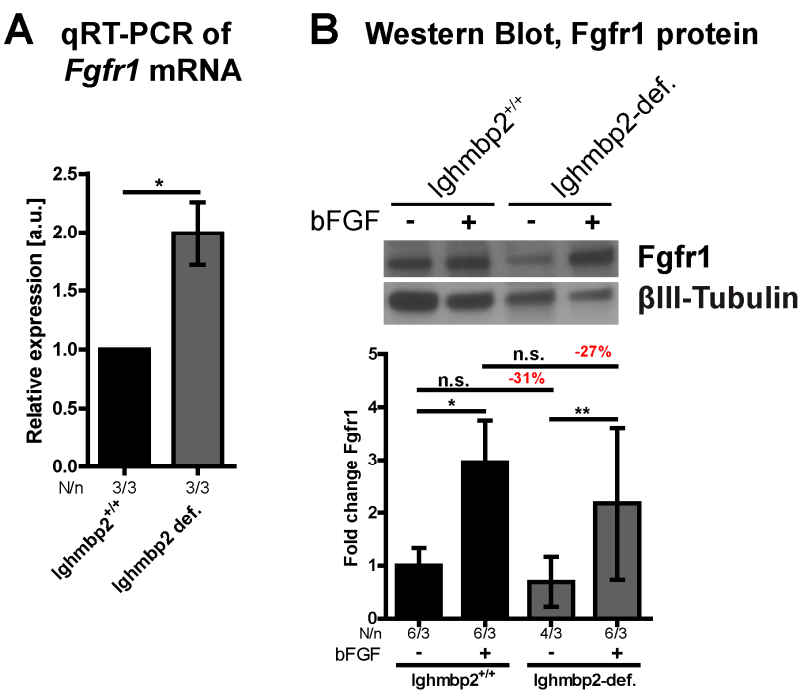

Figure 28 – Ighmbp2-def. motoneurons show an increased expression of *Fgfr1* mRNA, whereas Fgfr1 protein level is reduced. (A) Quantification of *Fgfr1* mRNA using qRT-PCR of Ighmbp2-def. and Ighmbp2$^{+/+}$ motoneurons cultured on laminin-111 at DIV7. Ighmbp2-def. motoneurons display a significantly increased expression of *Fgfr1* mRNA compared to Ighmbp2$^{+/+}$. (B) Western Blot analysis of Fgfr1 in untreated and bFGF long-term treated Ighmbp2-def. and Ighmbp2$^{+/+}$ motoneurons cultured on laminin-111 at DIV7. Untreated Ighmbp2-def. motoneurons show reduced Fgfr1 protein amount about -31% in comparison to untreated Ighmbp2$^{+/+}$ which significantly increases after bFGF long-term treatment in both conditions. Fgfr1 protein amount after bFGF treatment in Ighmbp2-def. motoneurons is 27% lower compared to long-term treated Ighmbp2$^{+/+}$. Data are shown as mean±SD. N defines the number of embryos; n indicates the number of experiments.

In contrast to the increased *Fgfr1* mRNA level, Fgfr1 protein in untreated Ighmbp2-deficient motoneurons displayed a tendential protein reduction of 31% compared to untreated Ighmbp2$^{+/+}$ (Fig. 28B). A long-term treatment of basic fibroblast growth factor (bFGF) increased the protein amount of Fgfr1 in both conditions, Ighmbp2-deficient and Ighmbp2$^{+/+}$, whereas Fgfr1 protein level is 27% lower after bFGF treatment compared to the long-term treated Ighmbp2$^{+/+}$. Treatment of bFGF rescued the protein amount in Ighmbp2-deficient motoneurons more than to an untreated Ighmbp2$^{+/+}$ level (Fig. 28B).

As *Fgfr1* mRNA in Ighmbp2-deficient motoneurons is significantly upregulated whereas the protein amount is reduced but can be rescued by long-term bFGF treatment (Fig. 28A-B), the question arises whether bFGF treatment can also rescue the branching behavior of Ighmbp2-deficient motoneurons. To investigate the potential role of bFGF treatment in Ighmbp2 deficiency, we performed morphological analysis regarding axon branching capacity, growth cone size and signal intensity of β-actin protein. For this purpose, axonal branching capacity was quantified in Ighmbp2-deficient motoneurons and Ighmbp2$^{+/+}$ with long-term bFGF treatment to analyze the effect of this growth factor on motoneuron differentiation behavior.

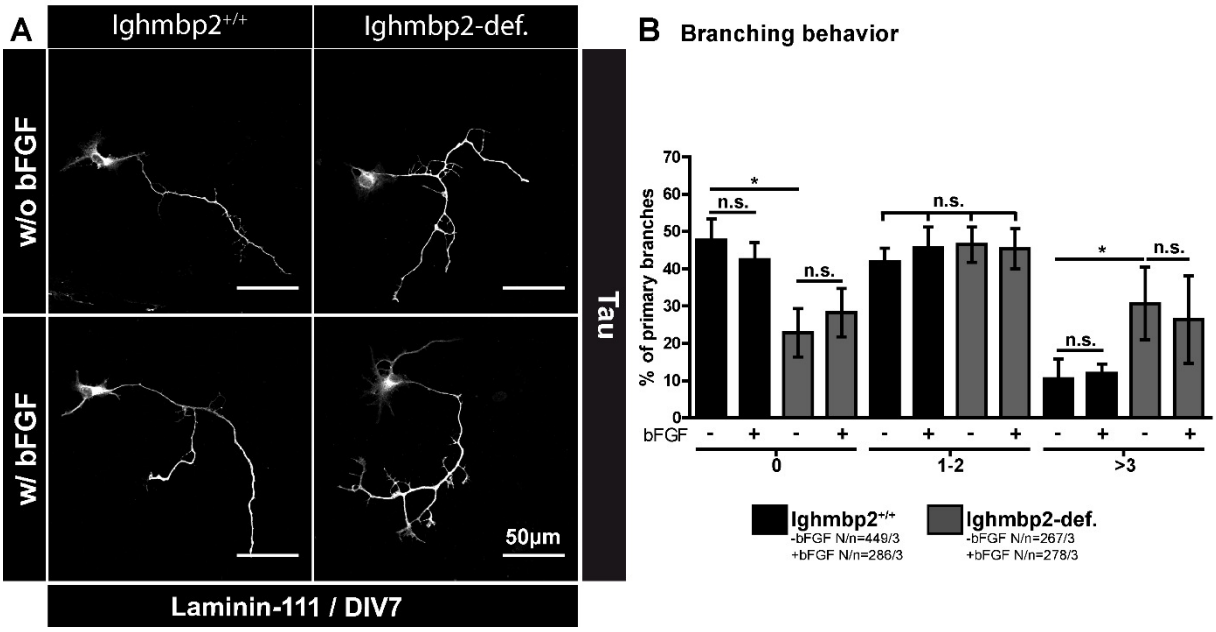

Figure 29 - bFGF treatment does not influence branching behavior of Ighmbp2-def. motoneurons. (A) Representative images of untreated or long-term treated Ighmbp2-def. and Ighmbp2$^{+/+}$ motoneurons cultured on laminin-111 at DIV7. (B) bFGF treatment does not affect axon branching behavior of long-term treated Ighmbp2-def. motoneurons in comparison to untreated Ighmbp2$^{+/+}$ motoneurons. In general, untreated and long-term treated motoneurons of both conditions show no alteration of branching capacity related to the bFGF treatment. In B, data are shown as mean±SD. N defines the number of analyzed cells (C); n indicates the number of experiments. % means percentage.

Affected branching behavior of untreated Ighmbp2-deficient motoneurons compared to untreated Ighmbp2$^{+/+}$ described above in Fig. 13C-D has been confirmed. The long-term treatment with bFGF displayed no significant effect on axonal outgrowth in both conditions. Neither long-term treated Ighmbp2-deficient nor long-term treated Ighmbp2$^{+/+}$ motoneurons showed an altered branching behavior (Fig. 29A-B).

Previous studies have shown that Ighmbp2-deficient motoneurons display reduced growth cone size and a decreased amount of β-actin protein cultured on laminin-211/221 (Krieger et al., 2014b), whereas Ighmbp2-deficient motoneurons show exclusively reduced β-actin protein level in the growth cones without reduced size when cultured on laminin-111 (Surrey et al., 2018). This raises the question whether bFGF treatment influences the growth cone phenotype regarding β-actin protein. Therefore, Ighmbp2-deficient and Ighmbp2$^{+/+}$ motoneurons were cultured with bFGF for 5 days on either laminin-111 or laminin-211/221 and were immuno-stained against β-actin. Then, the effect of long-term bFGF treatment was analyzed by quantifications of the growth cone size and the signal intensity of β-actin (Fig. 30A-C and Fig. 31A-C).

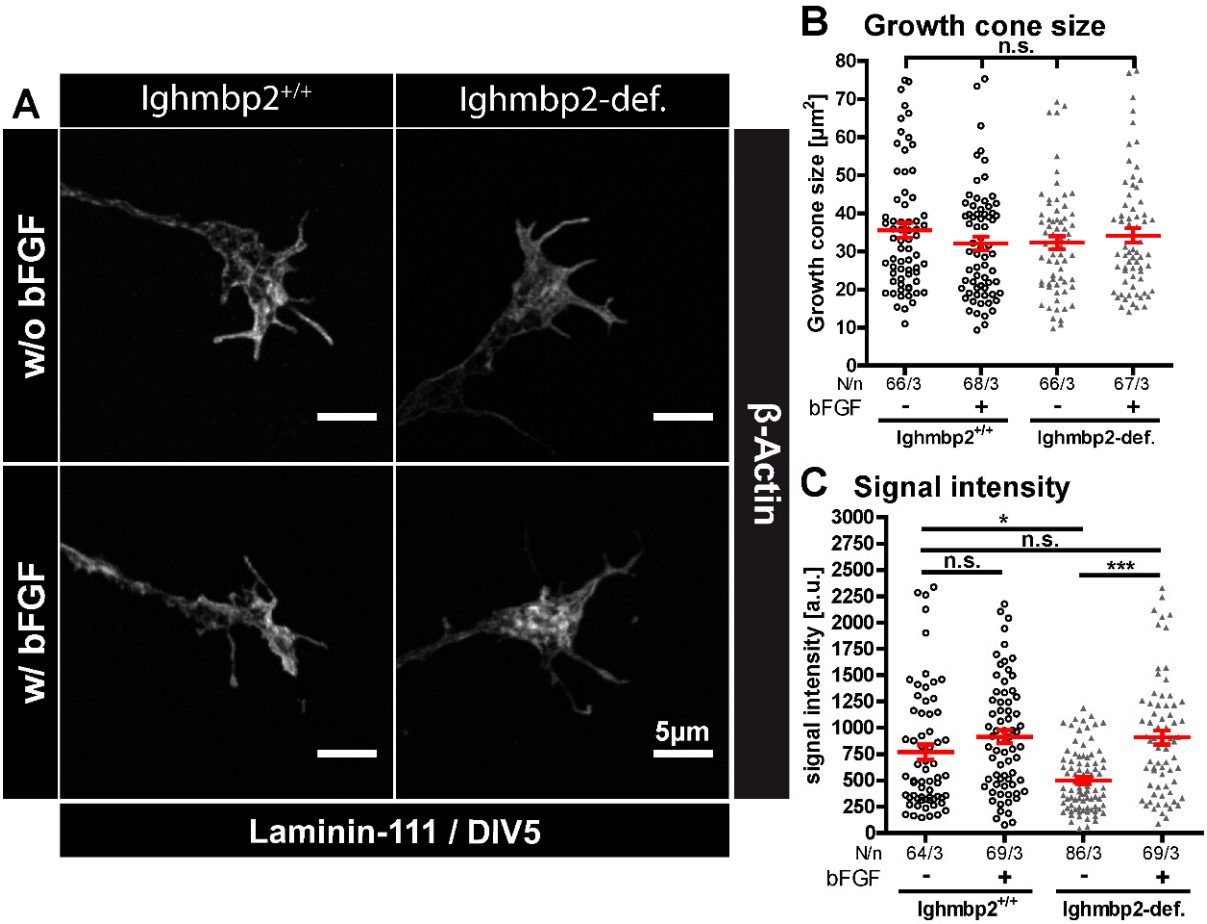

Figure 30 - bFGF long-term treatment increases β-actin protein amount in Ighmbp2-def. growth cones cultured on laminin-111 at DIV5 but has no influence on the size. (A) Representative images of bFGF untreated and long-term treated Ighmbp2-def. and Ighmbp2$^{+/+}$ growth cones cultured on laminin-111 at DIV5. Quantifications of the (B) growth cone size and (C) β-actin signal intensity of bFGF untreated and long-term treated Ighmbp2-def. and Ighmbp2$^{+/+}$ growth cones. (B) bFGF treatment has no effect on the growth cone size. (C) Untreated Ighmbp2-def. motoneurons show a reduced signal intensity of β-actin protein compared to untreated Ighmbp2$^{+/+}$, whereas bFGF long-term treatment increases the β-actin signal intensity to the normal untreated Ighmbp2$^{+/+}$ level. Untreated and bFGF long-term treated Ighmbp2$^{+/+}$ motoneurons display no statistically significant changed β-actin signal intensity. N defines the number of analyzes cells; n indicates the number of experiments.

bFGF treatment of Ighmbp2-deficient and Ighmbp2$^{+/+}$ motoneurons cultured on laminin-111 showed no alteration in growth cone size (Fig. 30A-B). Long-term treated Ighmbp2-deficient growth cones displayed significantly increased β-actin signal intensity which was comparable to the untreated and long-term treated Ighmbp2$^{+/+}$ β-actin signal intensity (Fig. A and C). Treatment of bFGF rescued the β-actin protein amount in Ighmbp2-deficient growth cones to the untreated Ighmbp2$^{+/+}$ level.

In addition, bFGF treatment of Ighmbp2-deficient and Ighmbp2$^{+/+}$ growth cones cultured on laminin-211/221 was quantified regarding size and β-actin signal intensity (Fig. 31A-C).

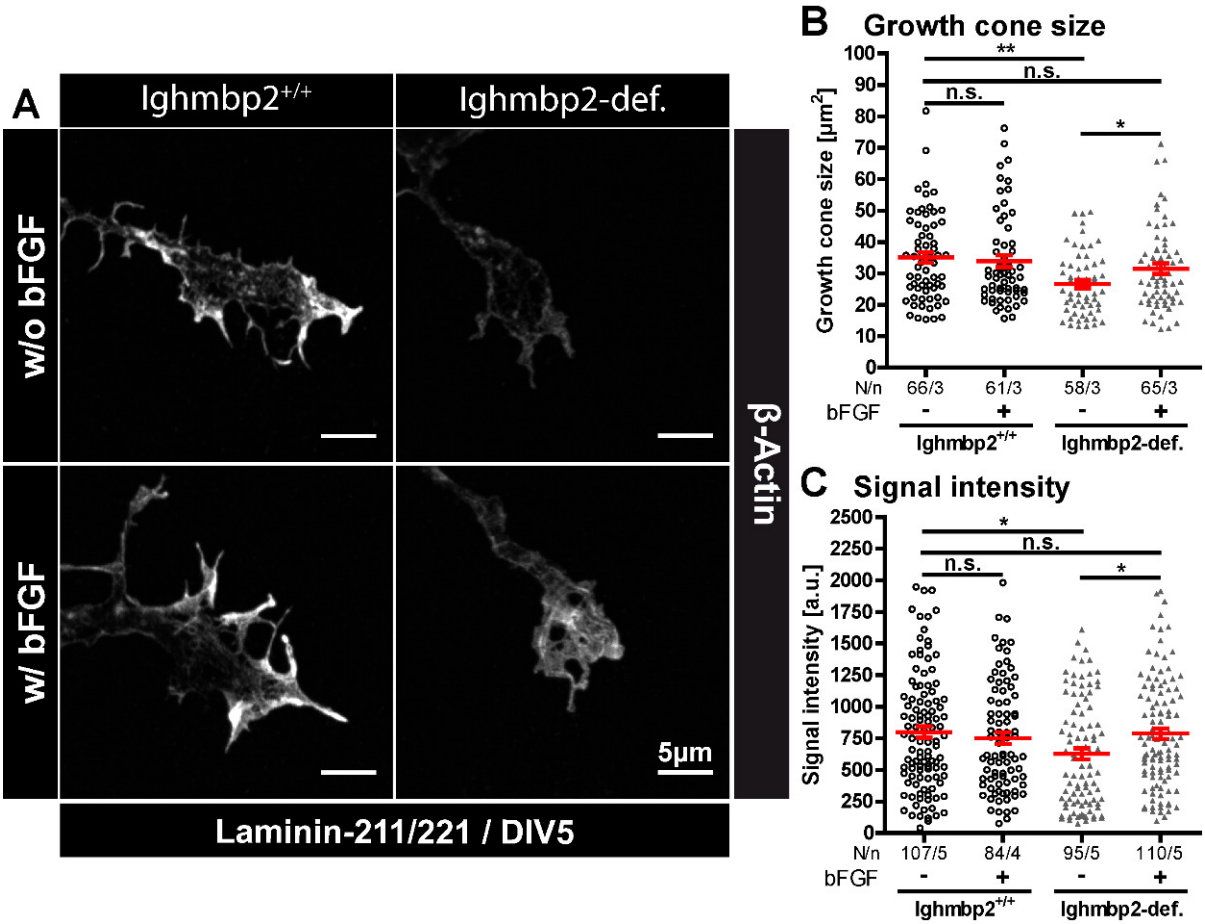

Figure 31 - bFGF long-term treatment increases β-actin protein level and the size of Ighmbp2-def. growth cones cultured on laminin-211/221 at DIV5. (A) Representative images of bFGF untreated and long-term treated Ighmbp2-def. and Ighmbp2$^{+/+}$ growth cones cultured on laminin-211/221 at DIV5. Quantifications of the (B) growth cone size and (C) β-actin signal intensity of bFGF untreated and long-term treated Ighmbp2-def. and Ighmbp2$^{+/+}$ growth cones. (B) bFGF treatment compensated the reduced growth cone size in Ighmbp2-def. motoneurons to normal untreated Ighmbp2$^{+/+}$ growth cone size. Untreated and bFGF long-term treated Ighmbp2$^{+/+}$ growth cones show no alteration. (C) Untreated Ighmbp2-def. motoneurons show a reduced signal intensity of β-actin protein compared to untreated Ighmbp2$^{+/+}$, whereas bFGF long-term treatment increases the β-actin signal intensity to the normal untreated Ighmbp2$^{+/+}$ level. Untreated and bFGF long-term treated Ighmbp2$^{+/+}$ motoneurons display no statistically significant changed β-actin signal intensity. N defines the number of analyzed cells; n indicates the number of experiments.

In accordance with previous publications (Krieger et al., 2014b), untreated Ighmbp2-deficient and Ighmbp2$^{+/+}$ motoneurons cultured on laminin-211/221 showed a reduced growth cone size which was rescued by bFGF treatment to untreated Ighmbp2$^{+/+}$ size level (Fig. 31A-B). Long-term treated Ighmbp2-deficient growth cones displayed significantly increased β-actin signal intensity compared to untreated and long-term treated Ighmbp2$^{+/+}$ β-actin signal intensity levels (Fig. 31A and C). Treatment of bFGF rescued the size and the β-actin protein amount in Ighmbp2-deficient growth cones to the untreated Ighmbp2$^{+/+}$ level.

As already described, bFGF is inter alia a ligand of FGFR1b, and 1c, FGFR2c, FGFR3c, FGFR and FGFR4Δ and can activate those receptors (Ornitz and Itoh, 2015). To determine whether the abundance of bFGF in the blood serum of *Nmd*^{2J} mice causes the decreased amount of Fgfr1, we performed a C2 mouse factor antibody array with blood serum of P28 *Nmd*^{2J} and *Nmd*$^{+/+}$ mice.

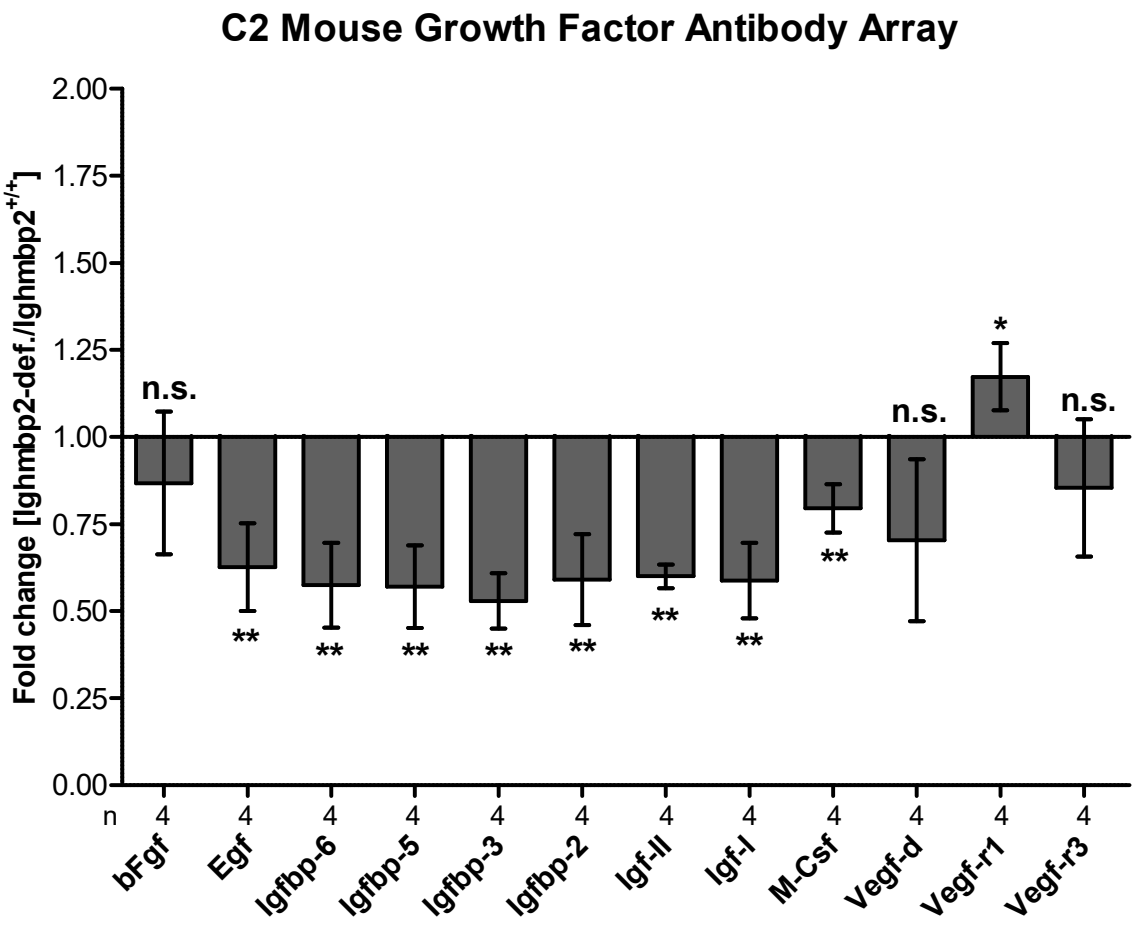

Figure 32 - Regulated growth factors in the blood serum of P28 *Nmd*^{2J} mice compared to *Nmd*$^{+/+}$ using C2 Mouse Growth Factor Antibody Array. Epidermal growth factor (Egf), insulin-like growth factor binding protein-2/-3/-5 and -6 (Igfbp-2/-3/-5 and -6), insulin growth factor-I and II (Igf-I/-II) and macrophage colony stimulating factor (M-Csf) are significantly reduced whereas vascular endothelial growth factor receptor-1 (Vegf-R1) is increased in *Nmd*^{2J} mice compared to *Nmd*$^{+/+}$. Quantifications are normalized to *Nmd*$^{+/+}$ equal to 1. Data are shown as mean±SD. n indicates the number of experiments per *Nmd*^{2J} and *Nmd*$^{+/+}$.

Quantification of C2 mouse growth factor antibody array displayed that bFGF is not significantly changed in *Nmd*^{2J} mice compared to *Nmd*$^{+/+}$. Nevertheless, several growth factors were altered in *Nmd*^{2J} mice compared to *Nmd*$^{+/+}$. Previous studies have shown that the level of insulin growth factor-I (Igf-I) in the blood serum at P14 and P42 *Nmd*^{2J} mice is significantly reduced by 50% compared to *Nmd*$^{+/+}$ but PEG-IGF-I application rescued the Igf-I level in the blood serum and improved the motor deficits seen in *Nmd*^{2J} mice (Krieger et al., 2014a). This treatment did not prevent motoneuron loss, which elucidated that additional mechanisms are involved leading to motoneuron loss in the *Nmd*^{2J} mice. Significant reduction of approximately 41% of Igf-I confirmed the validity of our C2 mouse growth factor antibody array (Fig. 32, Igf-I). Strikingly, all IGF binding proteins of this array (Igfbp-2/ -3/ -5 and -6) as well as Igf-II displayed a significant reduction in *Nmd*^{2J} mice (Fig. 32, Igfbp-2/ -3/ -5/ -6 and Igf-II). A reduction of immune modulator macrophage colony stimulating factor (M-Csf) could also be observed, whereas vascular endothelial growth factor

receptor-1 (Vegf-r1) was significantly upregulated in *Nmd*^{2J} mice compared to *Nmd*$^{+/+}$ (Fig. 32, M-Csf and Vegf-r1).

4.5 Protein-protein Interactions of Ighmbp2 using ICC and Co-IPs

To clarify the function of Ighmbp2, it is also necessary to identify interaction partners. Therefore, in the following section, possible protein interaction partners of Ighmbp2 were investigated using ICC and Co-IP.

4.5.1 Glutamylated / tyrosinated tubulin and Ighmbp2 protein in wildtype (CD1) motoneurons

As already described by (de Planell-Saguer et al., 2009), Ighmbp2 is co-localized with tubulin. Microtubules are very important in the development and formation of the nervous system, as they are responsible for the formation and stability of elongated axons and dendrites. Thus, they are also crucial factors when it comes to the development of neurodegenerative diseases and form directional railways for organelle transport and create a structural backbone for axons and dendrites, which is responsible for the maintenance and formation of morphology.

To determine a possible reason for increased branching behavior of Ighmbp2-deficient motoneurons, we performed immunocytochemical staining of wildtype motoneurons against Ighmbp2 and two types of tubulin – stable, glutamylated and labile, tyrosinated tubulin.

Glutamylated tubulin was evenly distributed throughout the cytoplasm of the cell body, alongside the axon but faintly expressed in the neurites and growth cones (Fig. 33A, upper and lower panel). Directional railways starting from the middle of the soma regarding and along the axons can be clearly observed (Fig. 33A, upper panel).

Tyrosinated tubulin was predominantly expressed in the protrusions, including the growth cones and axonal branches. It was highly concentrated in the dendritic protrusions, but less expressed in the soma. The tyrosinated tubulin also formed railway structures (Fig. 33B).

As previously described, Ighmbp2 localization is predominantly in the cytoplasm and in the axons of motoneurons, whereas its expression in the growth cone is omitted (Fig. 33A-B). Both types of tubulin were very similar distributed to Ighmbp2 (Fig. 33).

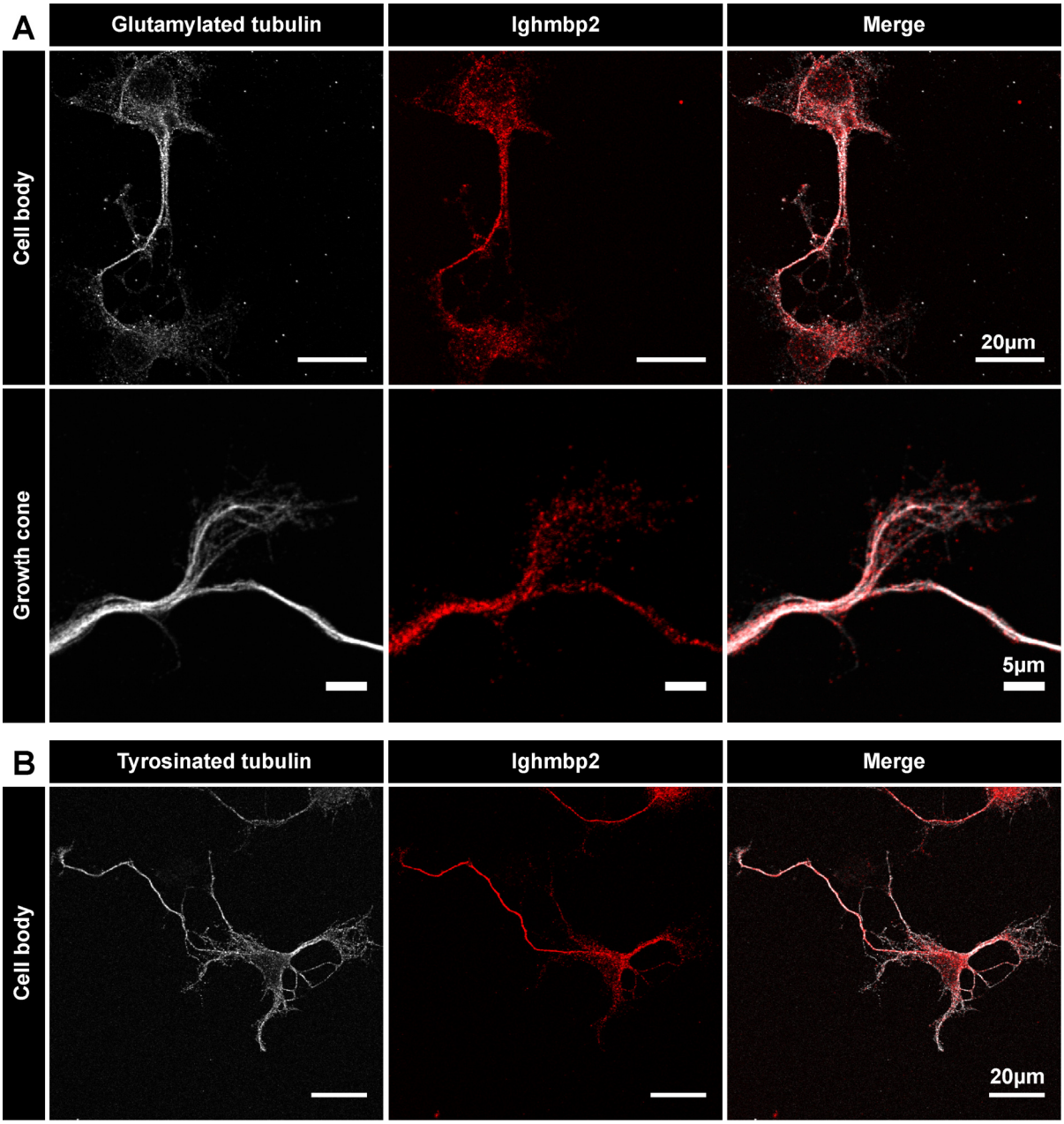

Figure 33 – Localization of glutamylated / tyrosinated tubulin and Ighmbp2 in wildtype motoneurons. Representative images of (A) glutamylated and (B) tyrosinated distribution pattern compared to Ighmbp2 protein localization. (A) Glutamylated tubulin is evenly distributed except the neurites (upper panel) and the growth cones (lower panel), whereas (B) tyrosinated tubulin is predominantly localized in distal parts of motoneurons, like neurites and axons. Ighmbp2 is similarly distributed to both types of tubulins. Each experiment was repeated at least 3 times, if not mentioned otherwise.

4.5.2 Co-IP with tyrosinated tubulin and IGHMBP2 in HEK293 cells

To examine a possible protein-protein interaction of tyrosinated tubulin and IGHMBP2, we performed a pulldown of IGHMBP2 in HEK293 cells following by a Co-immunoprecipitation (IP) of tyrosinated tubulin protein.

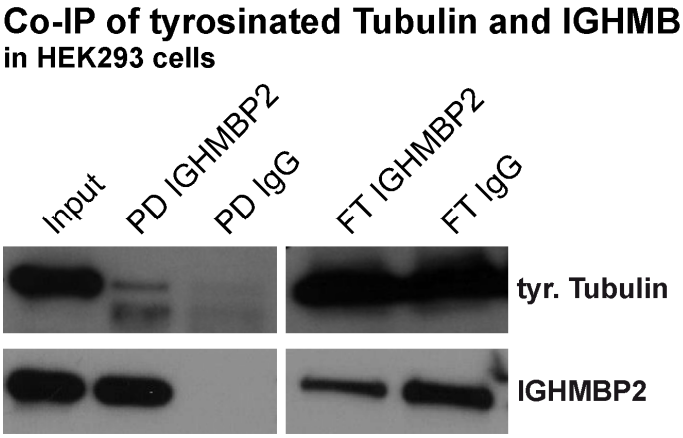

Figure 34 – Tyrosinated tubulin interacts with IGHMBP2 in HEK293 cells using Co-IP. Representative Western blot of immunoprecipitated IGHMBP2 and co-immunoprecipitated tyrosinated tubulin (tyr. Tubulin). Validation of successful pulldown (PD) of IGHMBP2 (lower panel). Tyr. tubulin protein is detectable in immuno-precipitated PD IGHMBP2 and therefore associated with IGHMBP2 protein. PD IgG, as a negative control, is free of IGHMBP2 and tyr. Tubulin. FT means flow-through.

Pulldown (PD) of IGHMBP2 was performed in HEK293 cells and validated using Western blot analysis against IGHMBP2 protein (Fig. 34, lower panel). Negative control condition with rabbit IgG antibody (PD IgG) was free of immunoprecipitated IGHMBP2, whereas IGHMBP2 protein was visible in PD of IGHMBP2 (PD Ighmbp2). Reduced amount of IGHMBP2 in the flow-through of immunoprecipitated IGHMBP2 (FT IGHMBP2) compared to the amount in FT IgG confirmed successful PD of IGHMBP2 protein (Fig. 34, lower panel). Co-IP of tyrosinated tubulin (tyr. tubulin) in immunoprecipitated IGHMBP2 protein lysate was performed to test whether both proteins interact with each other. In the PD of IGHMBP2, tyr. tubulin was detected, but no protein was visible in the negative control, PD IgG (Fig. 34, upper panel). Thus, IGHMBP2 protein interacts with tyrosinated tubulin in HEK293 cell.

4.5.3 Protein-protein interaction of IGHMBP2 using Co-IP

To analyze whether IGHMBP2 interacts with other proteins, we performed further Co-IP related to common and known protein interactors in Ighmbp2-deficient motoneurons and in other motoneuron diseases.

IGHMBP2 belongs to the UPF1-like group within the helicase superfamily 1, which can unwind DNA and RNA duplices (Guenther et al., 2009a; Jankowsky, 2011). Two other members of the UPF1-like group are UPF1 and MOV10, which bind to the 3'UTR of co-target mRNAs. It is known that MOV10 forms a complex with UPF1 at 3'UTR (Gregersen et al., 2014; Taylor et al., 2013). As both helicases belong to the same group as IGHMBP2, it should be tested whether IGHMBP2 is also a part of this complex. But neither UPF1 (Fig. 35A, upper panel), nor MOV10 (Fig. 35A, lower panel) show a direct interaction with IGHMBP2 (Fig. 35A). IGHMBP2 shows no direct interaction with MOV10, but it is known that

inter alia argonaute 2 (AGO2) is co-located with MOV10 in P-bodies. Based on this, the question arises whether P-bodies interact with Ighmbp2. For this purpose, we performed Co-IPs of U6 snRNA-associated Sm-like protein 4 (LSM4), AGO2 and trinucleotide repeat-containing gene 6B protein (TNRC6B), which is associated with Ago proteins, with immunoprecipitated IGHMBP2 protein in HEK293 cells. However, LSM4 (Fig. 35B, upper panel), AGO2 (Fig. 35B, lower panel) or TNRC6B (data not shown) were not co-located with immunoprecipitated IGHMPB2. A regulatory role of miRNAs which is already shown for the SMN protein (Kye et al., 2014) also needs to be questioned for IGHMBP2 and requires further investigation. In order to exclude an interaction of SMN and IGHMBP2, a Co-IP was performed between the two proteins. It is known that UPF1 affects FUS- and TDP43-associated toxicity in ALS (Barmada et al., 2015). IGHMBP2 shows a very high structural similarity to UPF1. Therefore, it was tested if SMN (Fig. 35D, upper panel), TDP43 (Fig. 35D, lower panel) or FUS (data not shown) interact with IGHMBP2. Finally, Co-IPs of the three proteins with IGHMBP2 showed that they were not associated with IGHMBP2. Pulldown (PD) of IGHMBP2 was performed in HEK293 cells and confirmed using Western blot analysis against IGHMBP2 protein (Fig. 35E).

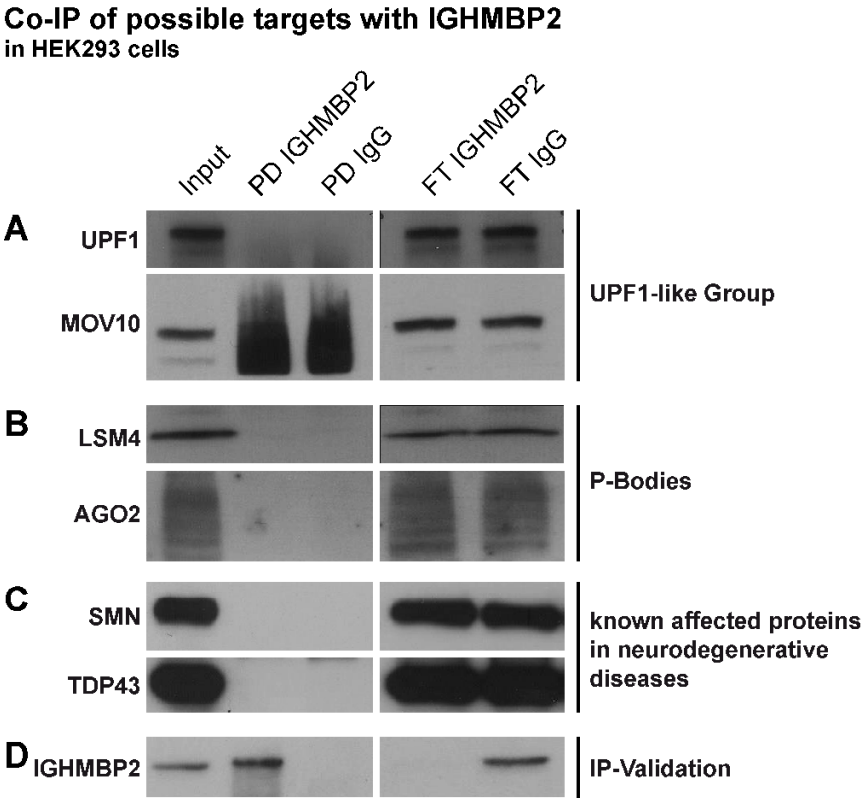

Figure 35 – Co-IPs of potential target proteins with IGHMBP2 in HEK293 cells. (A-D) Representative Western blot of immunoprecipitated Ighmbp2 and co-immunoprecipitated possible target proteins. (A) Two members of the UPF1-like group within the helicase superfamily 1, UPF1 and Mov10, show no direct interaction with IGHMBP2. (B) Known P-bodies, LSM4 and Ago2, do not interact with IGHMBP2. (C) The two affected proteins, SMN and TDP43, in known neurodegenerative diseases are not associated with IGHMBP2. (D) Validation of successful pulldown (PD) of IGHMBP2.

5. Discussion

Most parts of this discussion are published in (Surrey et al., 2018).

The cellular role of Ighmbp2 in the PNS is still unclear, but previous studies suggest that Ighmbp2 has an influence on DNA and / or RNA metabolism (de Planell-Saguer et al., 2009; Guenther et al., 2009a; Jankowsky, 2011). Defects in cytoplasmatic assembly of spliceosomal small nuclear ribonucleoproteins, pre-mRNA processing and activation of transcripts have already been shown in the pathomechanism of classical SMA (Campbell et al., 2000; Charroux et al., 1999; Fischer et al., 1997; Jablonka et al., 2001; Lefebvre et al., 1998; Meister et al., 2000; Pellizzoni et al., 2001; Strasswimmer et al., 1999). This raises the question whether functional differences at RNA and protein level can also be detected under Ighmbp2 deficiency in addition to morphological anomalies of motoneurons. Functional studies on the Ighmbp2 protein can only be carried out if it is possible to tag or label the protein of interest, especially using an antibody. This self-produced antibody first had to be verified in order to determine its specificity and to prove the credibility of functional studies (see Fig. 8 and Fig. 9). The purified Ighmbp2 antibody was validated by fractionation assay, immunoprecipitation, immunocytochemical staining (ICC) of primary motoneurons and Western blot investigations (see Fig. 10). As previously described, studies have shown that Ighmbp2 is predominantly localized in the cytoplasm (Grohmann et al., 2004). The fractionation assay and immunocytochemical staining confirmed the localization with the help of this antibody (see Fig. 10A, C). Ighmbp2 is reduced about 73% in primary cultured motoneurons from *Nmd*^{2J} mouse embryos (see Fig. 10D). The reduced protein amount of 20-30% remaining level of functional Ighmbp2 under Ighmbp2 deficiency is comparable to what has already been described for embryonic (Grohmann et al., 2004) and postnatal spinal cord tissue (Krieger et al., 2014a), although neither of these studies provided quantification.

Besides the distribution pattern by ICC and the general protein amounts determination of Ighmbp2 by Western blot quantification, it was also feasible to perform protein-protein interaction examinations between Ighmbp2 and postulated target proteins because immunoprecipitation was possible and specific (see Fig. 10B). An acute knockdown (KD) of *Ighmbp2* in wildtype motoneurons results in approximately 72% reduction of *Ighmbp2* transcript levels (see Fig. 11B), whereas the Ighmbp2 protein level is not reduced during the weeklong culture period (see Fig. 11A). Likewise, no effect on axonal outgrowth or branching capacity under acute KD of *Ighmbp2* could be determined (see Fig. 11C). Thus, only motoneurons from *Nmd*^{2J} mouse models show Ighmbp2 deficiency / reduction, all further experiments with motoneurons had to be carried out with *Nmd*^{2J} mice.

In general, axon length measurements are performed at DIV7 to include additional morphological changes at later time points. Functional and morphological analyses at growth cones (growth cone sizes, distribution of β-actin protein and mRNA, FRAP, AHA labeling and

calcium imaging studies) are carried out at DIV5, the latest time point at which growth cones are properly shaped and less collapsed. RNA-Seq, Western blot, and SUnSET data are collected at DIV7 to include the latest time point at which the cells are viable and less affected by apoptotic changes. pSILAC experiments are carried out at DIV3 due to the amount of cells needed for the experiment.

5.1 Ighmbp2 Deficiency in primary Motoneurons causes only minor morphological and functional Alterations

The primary cultured Ighmbp2-deficient motoneurons cultured on Laminin-111 showed no altered excitability at distal axons (see Fig. 12) or an affected axon elongation (see Fig. 13), but an increase of the axonal branches at DIV7 (see Fig. 13C, D). This slight morphological abnormality differs from primary motoneurons of SMA type I mouse models (Smn-deficient motoneurons) (Jablonka et al., 2007; Rossoll et al., 2003). In contrast to Ighmbp2-deficient motoneurons, Smn-deficient motoneurons show severe morphological and functional anomalies including the affected axonal outgrowth and growth cone size (Jablonka et al., 2007; Rossoll et al., 2003), as well as reduced spontaneous Ca^{2+} transients (Jablonka et al., 2007). Ighmbp2-deficient motoneurons show no alterations in spontaneous Ca^{2+} influx cultured on Laminin-111 (see Fig. 12) and only moderate changes cultured on Laminin-221 (Krieger et al., 2014b). A similar effect can also be observed with the growth cone size. The reduced growth cone size of Ighmbp2-deficient motoneurons on laminin-221 (Krieger et al., 2014b) is not visible on laminin-111 (see Fig. 14A, B and Fig. 15 A, B). A possible reason could be a failure of the F-actin assembly. Previous studies have shown that F-actin assembly in the growth cone of primary motoneurons is more prominent on β-chain laminin isoforms such as laminin-211/221 (Dombert et al., 2017).

Based on these data, the disease mechanism in Ighmbp2-deficient motoneurons does not correspond to the defective Ca^{2+} homeostasis as described for Smn-deficient motoneurons (Jablonka et al., 2007; Ruiz et al., 2010). This assumption is supported by further studies describing an unaffected neurotransmission at the neuromuscular endplates of *Nmd*^{2J} mice (Krieger et al., 2013). The late appearance of increased axonal branching of Ighmbp2-deficient motoneurons at DIV7 is consistent with observations in the *Nmd*^{2J} mouse in which increased axonal sprouting of NMJ was observed at the gastrocnemius muscle (Krieger et al., 2013).

However, defective collateral re-innervation was observed in some infantile SMARD1 patients (Diers et al., 2005). This induced compensatory mechanisms of axonal re-growth and the formation of new NMJs is a positive feature regarding compensation of motoneuron loss in the early stages of the disease (Krieger et al., 2013). Neither severe forms of SMA

patients (Korinthenberg et al., 1997) nor related SMA mouse models (Murray et al., 2013) showed this kind of motoneuron behavior. These findings suggest that pre-symptomatic motoneuron loss in *Nmd*^{2J} mice does not follow a “dying back” mechanism but could be induced by external effects. Previous studies have already shown that motoneurons prolong survival by inducing trophic factors using neuronal stem cells (Simone et al., 2014). If defects in the neurotrophic factor release exist, e.g. by Schwann cells, post-synapse, astrocytes, and other cells, this can lead to motoneuron loss. It has already been shown that *Nmd*^{2J} mice suffer from Igf-1 deficiency (Krieger et al., 2014a) and that the external application of PEG-IGF-1 to two-week-old mice compensates this deficiency. The increase of Igf-1 in the blood prevents muscle fiber degeneration in the gastrocnemius muscle and diaphragm but has no effect on the survival of motoneurons (Krieger et al., 2014a). As already described above, the differentiation and functionality of primary motoneurons cultured on a synapse-specific laminin isoform are mainly caused by BDNF and not GDNF or CNTF (Dombert et al., 2017). Based on these findings, the question arises whether Ighmbp2-deficient motoneurons cannot correctly recognize trophic factors and thus induce motoneuron death. In the *pmn* mouse and in the SOD1 mouse model for fALS, an external application of CNTF was able to extend the lifespan by counteracting the loss of motoneurons with the increase of CNTF (Giess et al., 2002; Sendtner et al., 1992). Furthermore, previous studies of the *pmn* mouse have already shown that increased Igf-1 causes an extended lifespan associated with mitigated motoneuron cell body and axon loss in the phrenic nerve (Jablonka et al., 2011).

It is therefore very obvious to consider and speculate about the affected trophic support, deficits in motoneurons to recognize these factors or other non-neuronal cells regarding the *Nmd*^{2J} mouse.

5.2 Ighmbp2 Deficiency in primary Motoneurons causes only minor Differences in Protein Biosynthesis

As already described, Ighmbp2 seems to be a ribosome-associated helicase belonging to the superfamily 1 (SF1) of helicases (Jankowsky, 2011), and is able to unwind RNA (Guenther et al., 2009a). Members of these SF1 helicases are UPF1, MOV10, and Senataxin. In general, they are functionally linked to various processes of RNA metabolism such as transcription, splicing, translation and RNA decay (Fairman-Williams et al., 2010; Guenther et al., 2009a; Jankowsky, 2011). Reduced growth cone size cultured on laminin-211/221 (Krieger et al., 2014b) and the decreased amount of α-/β-actin protein cultured on both laminin isoforms (see Fig. 14A, B and Fig. 15A, B) in combination with an increased axonal branching at DIV7 cultured on laminin-111 (see Fig. 13C, D) gives an indication of dysregulation of cytoskeletal proteins in *Nmd*^{2J} motoneurons. Therefore, the question arises

whether Ighmbp2 deficiency also affects cellular mechanisms that lead to altered protein biosynthesis. Due to the high incidence and crucial function of α- and β-actin in the cytoskeleton, our study is focused on these proteins. Immunocytochemical co-staining of both actin isotypes with Ighmbp2 showed a similar distribution pattern (see Fig. 17A, B). In addition, RNA-Sequencing (see Fig. 18A, D and E), FISH (see Fig. 18F and see Fig. 19), and qRT-PCR quantification (see Fig. 18 G and H) showed no changes in the amount and distribution of both isotypes in Ighmbp2-deficient motoneurons compared to Ighmbp2$^{+/+}$. Examination of α- and β-actin protein in Ighmbp2-deficient growth cones cultivated on laminin-111 displayed a compartment-specific reduced protein amount of both isotypes (see Fig. 14A, C and see Fig. 15A, C). This reduced amount can be considered as a consequence of a generally delayed protein biosynthesis (see Fig. 20 and see Fig. 21). FRAP analysis showed that the local translation of eGFP^{myr}-β-actin 3'UTR reporter in growth cones and cell body was significantly reduced in Ighmbp2-deficient motoneurons. However, it should be noted that this delayed translation effect was observed exclusively on Laminin-111 and was not visible on Laminin-211/221. It has already been shown that the local translation of the eGFP^{myr}-β-actin 3'UTR reporter is regulated depending on the laminin isoforms, laminin-111 and laminin-211/221 (Rathod et al., 2012). The local translation in growth cones of motoneurons cultured on laminin-211/221 shows a lower efficiency compared to motoneurons cultured on laminin-111 (Rathod et al., 2012). These data and the results of this FRAP analysis suggest that the local translation is influenced by the substrate and the protein biosynthesis in motoneurons cultured on Laminin-211/221 is impoverished compared to Laminin-111. The invisible effect on the local translation of the eGFP^{myr}-β-actin 3'UTR reporter in Ighmbp2-deficient motoneurons cultured on Laminin-211/221 can be explained hereby.

A comparable study of the local translation of α-actin is still pending, however, it is likely that a delayed compartment-independent protein biosynthesis is also present here.

At the beginning of this study, the FRAP data should be visualized with the help of a time course Western blotting analysis. However, this was not feasible as the GFP protein itself is not eliminated by the laser power. The high-intensity illumination only causes the fluorescence lifetime to quickly elapse, while the GFP protein is structurally unaffected. Thus, a time course of newly synthesized GFP-expressed 3'UTR β-actin reporter via Western blot is not possible. In connection with the delayed local translation of the eGFP^{myr}-β-actin 3'UTR reporter no change in the total amount of β-actin protein in whole cell lysates was detected (see Fig. 14D). This observation was found for the total amount of α-actin protein (see Fig. 15D). Based on these results, dysregulation of the initiation or early elongation during translation could provide a possible clarification. It could be speculated that Ighmbp2 modulates the entrance of specific mRNAs into the translational process. This would result in

a translational delay of specific proteins without showing a global effect on newly synthesized proteins. This hypothesis is supported by the pulsed SILAC (see Fig. 22), AHA-labeling (see Fig. 23A-C) and SUnSET studies (see Fig. 23D) which we performed.

Furthermore, the slight effect on the two candidates, Top1 and Sars2, in the pSILAC approach of Ighmbp2-deficient motoneurons at DIV3 (see Fig. 22A, C) and the undetectable alteration by western blot verification at DIV7 (see Fig. 22B) implies a critical role of Ighmbp2 at the initial steps of the translation. These slight effects on protein biosynthesis also indicate a cell compartment-specific role of Ighmbp2 on the translation mechanisms in primary cultured *Nmd*^{2J} motoneurons. The delayed local translation of the eGFP^{myr}-β-actin 3'UTR reporter could not be explained by a direct interaction of Ighmbp2 protein with the β-actin mRNA by RIP analysis (see Fig. 25A, B). Therefore, Ighmbp2 as a factor for mRNP clearance or mRNA degradation, as described for MOV10 or Upf1, is rather unlikely. As already described, these two helicases form a complex at 3'UTR (Gregersen et al., 2014; Taylor et al., 2013). Supporting results for this hypothesis can be found in the protein-protein interaction analysis between Ighmbp2 with Mov10 or UPF1. It was found that Ighmbp2 is neither associated with Mov10 nor with UPF1 (see Fig. 35A). The short residence time of IGHMB2 onto nucleic acids gives additional hints regarding the function of this helicase (Kanaan et al., 2018). Despite the high similarity to UPF1, IGHMBP2 does not guarantee the required time window to accomplish several successive steps such as translation-dependent recognition of a premature termination codon, ribosome dissociation, mRNP remodeling, and recruitment of RNA decay factors (Kanaan et al., 2018). This also suggests that IGHMBP2 is not involved in NMD.

In the case that Ighmbp2 has a regulatory role of miRNAs, as described for the SMN protein (Kye et al., 2014), it should still be questioned and it needs further investigation.

5.3 Affected Targets in Ighmbp2-deficient Motoneurons

5.3.1 Reduced Imp1 protein amount in Ighmbp2-deficient motoneurons

In order to get a more direct link to β-actin, further results on Imp1 protein level were achieved. Quantifications of Imp1 protein level via Western blot analysis were done.

In whole cell lysates of Ighmbp2-deficient motoneurons a reduced protein amount of insulin-like growth factor-2 mRNA binding protein 1 (Imp1) was found (see Fig. 26E) but the mRNA level was not affected (see Fig. 26D). Imp1 is described as *β-actin* mRNA interacting protein (Deshler et al., 1998; Ross et al., 1997) and in combination with a delayed local translation of the eGFP^{myr}-β-actin 3'UTR reporter in Ighmbp2-deficient motoneurons (see Fig. 20 and 21), it can be assumed that Imp1 may have an influence on this delayed

synthesis. The protein-mRNA interaction between IMP1 and *β-actin* is well described and is mediated by a sequence element in the 3' UTR of β-actin ("zipcode") mRNA and the mRNA-binding KH domain of IMP1 (Chao et al., 2010; Farina et al., 2003; Patel et al., 2012). As already described, RNA looping is mediated by protein-mRNA interaction, which is regulated by the IMP1 concentration (Nicastro et al., 2017). IMP1 is found as ribonucleoprotein granules within the cell (Jonson et al., 2007) and it releases *β-actin* mRNA after phosphorylation (Ceci et al., 2012; Huttelmaier et al., 2005; Sasaki et al., 2010; Urbanska et al., 2017).

To understand the role of Imp1 in delayed eGFPmyr-β-actin 3'UTR synthesis of Ighmbp2-deficient motoneurons, an extended morphological study on the specific distribution of Imp1-positive granules in different cell compartments is necessary. The immunocytochemical staining of Imp1 in Ighmbp2-def motoneurons also showed a reduced protein amount by signal intensity measurements of the soma and the distal axon (see Fig. 26A-C). These data are not reliable, as Imp1 is localized in granule-like structures (Degrauwe et al., 2016; Jonson et al., 2007; Niewidok et al., 2018) unevenly distributed throughout the whole cell. An exact quantification of Imp1 in different cell compartments requires high-resolution microscopy such as SIM, dSTORM or STED as well as *Imp1* knockdown or knockout in primary cultured motoneurons as a control. Quantification of Imp1 positive granules would include size and shape of the granules besides signal intensities. Confocal microscopy with a resolution limit of 200nm would not yield reliable / reasonable data. However, additional experiments with high-resolution microscopy in combination with *in situ* hybridization of *β-actin* mRNA are required as well. In addition, validation of the used Imp1 antibody with a KD of *Imp1* in motoneurons has to be completed to prove specificity. Studies in SMA motoneurons have already described in detail the crucial role of Imp1 in intracellular localization and local translation (Donlin-Asp et al., 2017a; Fallini et al., 2014). Furthermore, another study has already shown the crucial importance of Imp1 in neurodegenerative diseases (Donlin-Asp et al., 2017b). *Nmd*^{2J} motoneurons show only a small morphological and functional alteration, although Imp1 cannot be excluded as an important regulator of cellular mechanisms in Ighmbp2-deficient motoneurons by a compartment-specific β-actin reduction in combination with Imp1. A possible reason why the protein amount of Imp1 in the pSILAC experiment is not detectable could be due to the short pulse-duration of 20h. Only newly synthesized proteins are labeled. Unfortunately, the number of motoneurons from a single mouse embryo is limited. Therefore, extended biochemical approaches such as ribosomal profiling and whole proteome analysis are not feasible.

To investigate the connection between Ighmbp2 deficiency and Imp1 reduction, additional cellular and functional experiments have to be performed. The clarification of

further mRNA or protein interaction molecules with Imp1 could give us hints that influence the differentiation and survival of motoneurons.

The reduced Imp1 protein amount could have an effect on the transport (Chao et al., 2010; Farina et al., 2003; Patel et al., 2012) as well as on the translation of its bound mRNAs (Leung et al., 2006). A novel mRNA interaction with IMP1 protein was discovered by RIP analysis (see Fig. 27A, B). It should be emphasized that the *Fgfr1* mRNA and the protein in Ighmbp2-deficient motoneurons are altered (see Fig. 28). In correlation with a reduced Imp1 protein level, disturbed mRNA transport of *Fgfr1* could be responsible for this effect. Therefore, the increased *Fgfr1* mRNA (see Fig. 28A) and its reduced protein level (see Fig. 28B) could be explained by a predominantly local translation. To further investigate this hypothesis, *in situ* hybridization of *Fgfr1* mRNA in combination with immunocytochemical staining of the Imp1 protein should be performed. This allows the quantification of the amount and distribution of mRNA and protein. Furthermore, the increased mRNA levels and the reduced protein amount of Fgfr1 under Ighmbp2 deficiency suggest impaired translation. As described above, the IMP1 protein also influences the translation of its bound mRNAs (Leung et al., 2006). The impaired translation of Fgfr1 can therefore also be explained by the reduced amount of Imp1 protein as its interaction partner. In addition, an impairment of the transport of the Fgfr1 to the membrane can be discussed. Further experiments regarding the Fgfr1 protein distribution in Ighmbp2-deficient motoneurons could provide hints for this and influence Fgfr1 signaling.

5.3.2 Altered mRNA and protein amount of FGFR1 in Ighmbp2-deficient motoneurons

As previously described, the RNA sequencing data identified a significantly increased *Fgfr1* mRNA in Ighmbp2-def motoneurons cultured on laminin-111 on DIV7 (see Fig. 18C). qRT-PCR quantification confirmed this up-regulation (see Fig. 28A) so that Fgfr1 considers as a possible target under Ighmbp2 deficiency.

The paracrine growth factor bFGF binds to FGFR1 (Ibrahimi et al., 2004), which is dimerized and activated by that (Chen et al., 2008; Furdui et al., 2006). The binding of bFGF depends on co-factors such as heparin, heparan sulfate proteoglycans and klotho (Schlessinger et al., 2000; Suzuki et al., 2008) and activates the MAPK signaling pathway as well as the PI3K/Akt, PLCγ and STAT signaling pathways (Ornitz and Itoh, 2015). These bFGF/FGFR1 mediated signaling pathways play a crucial role in neurogenesis and have been considered as a treatment approach for neurodegenerative diseases (Woodbury and Ikezu, 2014). Further investigations are needed to show whether the increase in Fgfr1 protein by stimulation of bFGF leads to a rescue of the functional receptor. The functionality of the bFGF/FGFR1 mediated activation under Ighmbp2 deficiency can be performed with

the help of further Western Blot quantifications in which the phosphorylated Fgfr1 is investigated. Moreover, the distribution and localization of the receptor after bFGF long-term treatment in the growth cones as well as in soma should be analyzed to obtain details of impaired distribution patterns in Ighmbp2-deficient motoneurons.

To investigate the influence of Fgfr1 in Ighmbp2-deficient motoneurons, further morphological and functional studies were performed under long-term treatment with bFGF. The Fgfr1 protein level under bFGF stimulation using Western Blot and the effect on the branching capacity as well as on the growth cone size and therein impaired β-actin protein amount was investigated. In addition, the content of different growth factors, especially bFGF, in the blood serum of P28 *Nmd*^{2J} mice was tested.

In contrast to the increased RNA level, a reduction of 31% Fgfr1 protein in untreated Ighmbp2-deficient motoneurons compared to untreated Ighmbp2$^{+/+}$ was detected (see Fig. 28B). This observation suggests a translational defect so that the up-regulated mRNA could be a compensatory mechanism of the motoneuron. In a seven days long-term treatment with bFGF an upregulation of Fgfr1 in Ighmbp2-deficient and Ighmbp2$^{+/+}$ motoneurons was observed, whereby treated motoneurons under Ighmbp2 deficiency showed a reduced amount of 27% Fgfr1 compared to treated Ighmbp2$^{+/+}$ (see Fig. 28B). Nevertheless, the protein level of Fgfr1 in treated Ighmbp2-deficient motoneurons increased higher compared to untreated Ighmbp2$^{+/+}$ (see Fig. 28B). Thus, stimulation with bFGF of Ighmbp2-deficient motoneurons were able to compensate the reduced protein content. The activation of Fgfr1 and down signaling pathways mediated by bFGF could explain this effect. The function of MAPK and PI3K/act pathways is associated with cell proliferation, growth and mRNA translation activation (Roux and Topisirovic, 2012). The external activation of the afore-mentioned signal cascades using bFGF treatment could promote the translation of the significantly increased *Fgfr1* mRNA in Ighmbp2-deficient motoneurons and thus compensate the missing protein amount. Therefore, a possible treatment strategy using bFGF stimulation under Ighmbp2 deficiency should be considered. Increased branching behavior of Ighmbp2-deficient motoneurons at DIV7 (see Fig. 13C, D) was already described in chapter 5.1. Therefore, the effect of long-term bFGF stimulation should be investigated on the axonal behavior of Ighmbp2-deficient motoneurons. The long-term treatment of bFGF showed no influence on axonal branching in Ighmbp2-deficient or Ighmbp2$^{+/+}$ motoneurons (see Fig. 29). Increased branching behavior of Ighmbp2-deficient motoneurons compared to Ighmbp2$^{+/+}$ displayed no alteration under bFGF stimulation (see Fig. 29). As already discussed in chapter 5.1, the ability to form additional axonal branches is to be regarded as a compensatory mechanism in the early stage of the disease and thus rather as a good feature. Consequently, this behavior is not mediated by the activation of the Fgfr1 and its signaling pathways.

Furthermore, analyses of the growth cone size and signal intensity of β-actin in Ighmbp2-deficient growth cones after long-term treatment with bFGF cultured on Laminin-111 (see Fig. 30) and Laminin-211/221 (see Fig. 31) were performed. In accordance with the results discussed in chapter 5.1, neither untreated nor treated Ighmbp2-deficient motoneurons cultured on Laminin-111 showed an altered growth cone size compared to untreated or treated Ighmbp2$^{+/+}$ (see Fig. 30A, B). However, the bFGF stimulation of Ighmbp2-deficient motoneurons compensated the reduced β-actin signal intensity up to the Ighmbp2$^{+/+}$ level, whereas untreated and long-term bFGF-treated Ighmbp2$^{+/+}$ motoneurons showed no change in β-actin signal intensity (see Fig. 30A, C).

bFGF long-term treatment of Ighmbp2-deficient motoneurons cultured on Laminin-211/221 exhibits not only a compensation of the β-actin signal intensity (see Fig. 31A, C), but also an increase of the growth cone size (see Fig. 31A, B). Independent of the substrate, the bFGF stimulation mediates FGFR activation, which can compensate and rescue the reduced growth cone size on laminin-211/221 and the reduced β-actin signal intensity on laminin-111 and laminin-211/221 *in vitro*.

The phenotypical symptoms of P28 *Nmd*^{2J} mice are already pronounced at this developmental stage. Severe atrophy of the gastrocnemius muscle, a reduced height, and body weight can be observed (Cox et al., 1998; Grohmann et al., 2004; Krieger et al., 2014a). The examination of several growth factors in the blood serum of P28 *Nmd*^{2J} compared to *Nmd*$^{+/+}$ mice showed clear dysregulation, but bFGF was not significantly altered in the blood serum (see Fig. 32). However, this result does not exclude that activation of Fgfr1 is impaired. Therefore, further investigations should be performed regarding Fgfr1 activation. It should be noted that all Igfbps and both Igf-I and -II were significantly reduced in the *Nmd*^{2J} mice compared to *Nmd*$^{+/+}$. As previous studies have shown, Igf-1 is significantly reduced to about 50%, but P14 *Nmd*^{2J} mice showed a significant upregulation of Igfbp-2 and Igfbp-3 in the blood serum (Krieger et al., 2014a). However, P42 *Nmd*^{2J} mice exhibited no significant differences of Igfbp-2 and Igfbp-3 in the blood serum compared to *Nmd*$^{+/+}$ (Krieger et al., 2014a). These published results contrast with the observed Igfbp-2 and Igfbp-3 levels in the blood serum of P28 *Nmd*^{2J} mice, as a clear downregulation can be observed here (see Fig. 32). A possible reason could be the heterogeneity of the developmental stages of P14, P28, and P42. Nevertheless, the involvement of Igfs and their binding proteins in SMARD1 is evident. For this reason, further investigations should be conducted. Interestingly, an upregulation of Vegf-r1 protein was detected in the blood serum of P28 *Nmd*^{2J} mice. Previous publications have shown that Vegf-r1 can be stimulated autocrine by Fgfr1 activation via the MAPK signaling pathway (Golfmann et al., 2018). Thus, the regulated Vegf-r1 protein is also related to the affected Fgfr1, which should be investigated later.

5.3.3 Imp1 and Fgfr1 as affected proteins in SMARD1 disease

Additional and detailed investigation of the newly identified Imp1 and Fgfr1 targets in the *Nmd*^{2J} mouse model could reveal the influenced cellular and functional mechanisms that occur under Ighmbp2 deficiency. Compensation of the altered protein levels of Imp1 and Fgfr1 by the external application could possibly inhibit or even stop the progression of SMARD1 disease. In order to carry out an all-encompassing analysis, further experiments with patient material are indispensable. This makes it possible to determine whether IMP1 and FGFR1 also have an influence on the pathogenesis of SMARD1 in humans. The identification of Imp1 and Fgfr1 as affected targets in *Nmd*^{2J} mice seems to be very promising, but it does not explain the exact function of Ighmbp2 but only opens secondary effects. Motoneurons under Ighmbp2 deficiency display only a minor regulation on RNA level, which show an upregulation of *Fgfr1* mRNA (see Fig. 18A, C). At the protein level, the Fgfr1 (see Fig. 28B) and the Imp1 protein (see Fig. 26E) are downregulated. This observation is again more likely to suggest a translational defect rather than an affected RNA level. Previous studies can also confirm this assumption, as most mutations in SMARD1 patients are located in the helicase domain of IGHMPB2 (Guenther et al., 2009a; Guenther et al., 2009b). A missing ribosome arrangement or an impairment in the tRNA pathway can be discussed as possible translational defects. Some studies have also hypothesized that translation cannot be correctly initiated due to bound miRNAs or proteins that cannot be properly removed caused by Ighmbp2 deficiency (de Planell-Saguer et al., 2009; Guenther et al., 2009a). The clarification of affected translational deficits under Ighmbp2 deficiency, which among others lead to reduced Imp1 and Fgfr1 protein levels, could provide an indication of the Ighmbp2 function. This could furnish an explanation for motoneuron death and thus yield an overview of the affected cellular mechanisms present in SMARD1 disease.

5.4 Protein-protein Interaction of IGHMBP2 and possible Protein Targets

The identification of protein interaction partners of IGHMBP2 could give an additional impression of its function. Immunocytochemical staining and Co-IP were performed to detect protein-protein interactions between IGHMBP2 and possible targets. Based on published results that IGHMBP2 was associated with tubulin (de Planell-Saguer et al., 2009) immunocytochemical staining of wildtype motoneurons against Ighmbp2 and two types of tubulin - stable, glutamylated and labile, tyrosinated tubulin- were performed (see Fig. 33).

Tubulin is a heterodimer consisting of an α-tubulin and a β-tubulin subunit. These two subunits have a very high affinity to each other and form a heterodimer, which creates an intrinsic polarity - the dynamic plus end consisting of β-tubulins and the stable minus end

consisting of the α-tubulins. This polarity, in turn, is used by motor proteins such as dynein and kinesin to migrate on the surface of the microtubule to the plus and minus end with the help of ATP hydrolysis (Baas et al., 1988; Baas et al., 1989; Baas and Lin, 2011; Baas et al., 2016). Therefore, a neuron consists of balanced stable (glutamylated) microtubule fractions and balanced, unstable (tyrosinated) microtubule fractions. In the axon, the microtubules are mainly uniformly oriented with their plus end toward to the distal end, whereas in the dendrites the microtubules exhibit a non-uniform, rather mixed polar distribution (Baas et al., 1988; Baas et al., 1989; Baas and Lin, 2011; Baas et al., 2016). As already mentioned, microtubules have an important function during the development and formation of the nervous system, as they are responsible for the formation and stability of elongated axons and dendrites. Both types of tubulin show a very similar distribution to Ighmbp2 and this suggests a co-localization, especially in the axons and axonal branches (see Fig. 33). IP using anti-Ighmbp2 antibody from HEK293 cells was performed and probed against tyrosinated tubulin to analyze the interaction between immunoprecipitated IGHMBP2 and tyrosinated tubulin. It was possible to detect a faint signal (see Fig. 34, upper panel). Thus, IGHMBP2 protein interacts with tyrosinated tubulin in HEK293 cell. This observation is consistent with the results of Planell-Saguer et al. 2009, which also showed only a faint interaction of α-tubulin with IGHMBP2 (de Planell-Saguer et al., 2009). Co-IP of immunoprecipitated IGHMBP2 of HEK293 cells with glutamylated tubulin is still outstanding. The crucial role of microtubules in axonal outgrowth or stabilization and the protein-protein interaction with Ighmbp2 provides a possible explanation for the increased branching capacity of Ighmbp2-deficient motoneurons. Further studies should be carried out based on these results.

IGHMBP2 belongs to the UPF1-like group within the helicase superfamily 1 and is able to unwind DNA and RNA duplices (Guenther et al., 2009a; Jankowsky, 2011). Two other known members of this group are UPF1 and MOV10, which bind to the 3'UTR of co-target mRNAs. Mov10, which is a messenger ribonucleoprotein (mRNP) clearance factor, remodels local secondary structures of mRNAs and displaces proteins from mRNAs targeted for UPF1-mediated degradation (Gregersen et al., 2014). UPF1 is one key factor in nonsense-mediated decay (NMD) (Kervestin and Jacobson, 2012). It is known that MOV10 forms a complex with UPF1 at 3'UTR (Gregersen et al., 2014; Taylor et al., 2013). Since IGHMBP2 belongs to the same group as MOV10 and UPF1, it should be determined if it belongs to this complex as well. However, it was demonstrated that neither UPF1 (see Fig. 35A, upper panel) nor MOV10 (see Fig. 35A, lower panel) interact with IGHMBP2. In summary, IGHMBP2 is not part of the complex of MOV10 and UPF1 at 3'UTR, but it is known that among others argonaute 2 (Ago2) is co-localized with Mov10 in P-bodies. Processing bodies (P-bodies) are located in the cytoplasm of eukaryotic cells. They consist

of several enzymes involved in mRNA turnover. Previous studies have already described that P-bodies play a crucial role in general mRNA decay, nonsense-mediated mRNA decay, adenylate-uridylate-rich element-mediated mRNA decay, and microRNA induced mRNA silencing (Kulkarni et al., 2010). Thus, the question arises whether Ighmbp2 interacts with P-bodies. Co-IPs were performed with LSM4 (a decapping co-activator as part of the multimeric protein complex with P-bodies) AGO2, and TNRC6B, which is associated with Ago proteins, with immunoprecipitated IGHMBP2 in HEK293 cells (Eulalio et al., 2007). Even so, IGHMBP2 did not interact with LSM4 (Fig. 35B, upper panel), AGO2 (Fig. 35B, lower panel) and TNRC6B (data not shown). The similarity to UPF1 caused additional investigations. It is already described that UPF1 reduces FUS- and TDP43-associated toxicity by a NMD mechanism in ALS (Barmada et al., 2015). In addition, a regulatory role of miRNAs for the SMN protein was demonstrated (Kye et al., 2014), which could also be questionable for IGHMBP2 protein. Based on this, protein interaction between IGHMBP2 with FUS, TDP43, and SMN was determined. No interaction between the proteins could be found, which makes the role of Ighmbp2 as a factor for mRNP clearance or mRNA degradation unlikely. This was already discussed in chapter 5.2.

5.5 SMARD1 compared to SMA and CMT2

Previous studies have shown that the SMN protein and its role in spinal muscular atrophy (SMA) has been described as a master regulator in ribosome biology (Bernabo et al., 2017), mRNA localization and local translation (Akten et al., 2011; Donlin-Asp et al., 2016; Fallini et al., 2011; Fallini et al., 2014; Fallini et al., 2016; Hubers et al., 2011; Rossoll et al., 2003; Sanchez et al., 2013). In comparison to Smn-deficient motoneurons, Ighmbp2-deficient motoneurons show only minor changes at RNA and protein level. A possible conclusion is that a limited but highly specific number of target molecules under Ighmbp2 deficiency could be responsible for the differentiation and survival of motoneurons. However, another hypothesis could be that Ighmbp2 also has cellular functions in addition to its function as a translation modulator. External studies have identified two heterozygous mutations in IGHMBP2 associated with Charcot-Marie-Tooth type 2 (CMT2) which is the axonal form of CMT disease (Cottenie et al., 2014). The phenotypic appearance of CMT2 patients is slow progressive muscle weakness, sensory loss, and axonal neuropathy, but no respiratory impairment, which contrasts with SMARD1 patients (Cottenie et al., 2014). Patients with CMT2 show a higher IGHMBP2 protein level compared to SMARD1 patients (Cottenie et al., 2014). Dominantly inherited mutations in five different genes of cytoplasmic tRNA synthetase (aaRS) could be described as the genetic cause for axonal and intermediate forms of CMT. In general, aaRSs are enzymes that catalyze “tRNA aminoacylation” by covalently binding

amino acids to their related tRNAs. With this knowledge in combination that Ighmbp2 is a ribosome-associated helicase, ribosomal stalling could be debated as another possible disease mechanism for SMARD1 (Surrey and Jablonka, 2018).

It is questionable whether further cellular signaling pathways under Ighmbp2 deficiency are impaired. If all previously mentioned facts regarding postmitotic motoneurons are placed in context, the new synthesis of proteins does not influence global cellular change at the protein level. In addition, no direct mRNA binding of affected target proteins such as β-actin were detected (see Fig. 25A, B). In general, the interaction of IGHMBP2 protein with RNA molecules was moderate to weak (see Fig. 24). Therefore, there are many arguments in support of an indirect or modulating role of Ighmbp2 in translation. However, it should not be ruled out that even small alterations can lead to motoneuron loss. Nevertheless, further investigations should be carried out regarding non-cell autonomous mechanisms, as it is well known that this can also lead to the death of motoneurons.

5.6 Non-cell-autonomous Disease Mechanisms

It can be summarized that the fast and enormous loss of motoneurons only a few days after the birth of the *Nmd*^{2J} mouse cannot be completely explained by small morphological and functional changes of the postmitotic primary cultured Ighmbp2-deficient motoneurons. In principle, many studies have been conducted on the Ighmbp2 function regarding RNA and translation processes in non-neuronal proliferating cells or neuron-like cell lines (de Planell-Saguer et al., 2009; Guenther et al., 2009a). This makes it possible to investigate an effect of cellular mechanisms in non-neuronal cells under Ighmbp2 deficiency, which in addition to motoneurons can lead to loss. Non-cell autonomous mechanisms have already been described for various forms of amyotrophic lateral sclerosis by mutations in SOD1 (Clement et al., 2003) and TDP-43 (Haidet-Phillips et al., 2011; Lee et al., 2016; Meyer et al., 2014) and spinal and bulbar muscular atrophy (SBMA) (Sambataro and Pennuto, 2012). This opens the view on non-cell autonomous mechanisms which might impact motoneuron differentiation and survival because of affected trophic support.

6. References

Acevedo, V.D., et al., 2007. Inducible FGFR-1 activation leads to irreversible prostate adenocarcinoma and an epithelial-to-mesenchymal transition. Cancer Cell. 12, 559-71.

Akten, B., et al., 2011. Interaction of survival of motor neuron (SMN) and HuD proteins with mRNA cpg15 rescues motor neuron axonal deficits. Proc Natl Acad Sci U S A. 108, 10337-42.

Albuisson, J., et al., 2005. Kallmann syndrome: 14 novel mutations in KAL1 and FGFR1 (KAL2). Hum Mutat. 25, 98-9.

AlSaman, A., Tomoum, H., 2010. Infantile spinal muscular atrophy with respiratory distress type 1: a case report. J Child Neurol. 25, 764-9.

Baas, P.W., et al., 1988. Polarity orientation of microtubules in hippocampal neurons: uniformity in the axon and nonuniformity in the dendrite. Proc Natl Acad Sci U S A. 85, 8335-9.

Baas, P.W., Black, M.M., Banker, G.A., 1989. Changes in microtubule polarity orientation during the development of hippocampal neurons in culture. J Cell Biol. 109, 3085-94.

Baas, P.W., Lin, S., 2011. Hooks and comets: The story of microtubule polarity orientation in the neuron. Dev Neurobiol. 71, 403-18.

Baas, P.W., et al., 2016. Stability properties of neuronal microtubules. Cytoskeleton. 73, 442-460.

Barde, Y.A., 1989. Trophic factors and neuronal survival. Neuron. 2, 1525-34.

Barmada, S.J., et al., 2015. Amelioration of toxicity in neuronal models of amyotrophic lateral sclerosis by hUPF1. Proc Natl Acad Sci U S A. 112, 7821-6.

Bernabo, P., et al., 2017. In Vivo Translatome Profiling in Spinal Muscular Atrophy Reveals a Role for SMN Protein in Ribosome Biology. Cell Rep. 21, 953-965.

Bertini, E., et al., 1989. Distal infantile spinal muscular atrophy associated with paralysis of the diaphragm: a variant of infantile spinal muscular atrophy. Am J Med Genet. 33, 328-35.

Bleyl, D.W.R., 1975. K. THEILER: THE HOUSE MOUSE. DEVELOPMENT AND NORMAL STAGES FROM FERTILIZATION TO 4 WEEKS OF AGE. 168 Seiten, 312 Abb. Springer Verlag, Berlin-Heidelberg-New York 1972, Preis: 124,— DM; 50,60 $. Food / Nahrung. 19, 737-737.

Borello, U., et al., 2008. FGF15 promotes neurogenesis and opposes FGF8 function during neocortical development. Neural Dev. 3, 17.

Bossy-Wetzel, E., Schwarzenbacher, R., Lipton, S.A., 2004. Molecular pathways to neurodegeneration. Nat Med. 10 Suppl, S2-9.

Bove, K.E., Lannaccone, S.T., 1988. Atypical Infantile Spinomuscular Atrophy Presenting as Acute Diaphragmatic Paralysis. Pediatric Pathology. 8, 95-107.

Briese, M., et al., 2016. Whole transcriptome profiling reveals the RNA content of motor axons. Nucleic Acids Res. 44, e33.

Briscoe, J., et al., 2000. A homeodomain protein code specifies progenitor cell identity and neuronal fate in the ventral neural tube. Cell. 101, 435-45.

Bruijn, L.I., Miller, T.M., Cleveland, D.W., 2004. Unraveling the mechanisms involved in motor neuron degeneration in ALS. Annu Rev Neurosci. 27, 723-49.

Buller, A.J., Eccles, J.C., Eccles, R.M., 1960. Interactions between motoneurones and muscles in respect of the characteristic speeds of their responses. J Physiol. 150, 417-39.

Campbell, L., et al., 2000. Direct interaction of Smn with dp103, a putative RNA helicase: a role for Smn in transcription regulation? Hum Mol Genet. 9, 1093-100.

Ceci, M., et al., 2012. RACK1 is a ribosome scaffold protein for beta-actin mRNA/ZBP1 complex. PLoS One. 7, e35034.

Chao, J.A., et al., 2010. ZBP1 recognition of beta-actin zipcode induces RNA looping. Genes Dev. 24, 148-58.

Chao, M.V., 2003. Neurotrophins and their receptors: a convergence point for many signalling pathways. Nat Rev Neurosci. 4, 299-309.

Charroux, B., et al., 1999. Gemin3: A novel DEAD box protein that interacts with SMN, the spinal muscular atrophy gene product, and is a component of gems. J Cell Biol. 147, 1181-94.

Chen, H., et al., 2008. A crystallographic snapshot of tyrosine trans-phosphorylation in action. Proc Natl Acad Sci U S A. 105, 19660-5.

Chen, Y.Z., et al., 2004. DNA/RNA helicase gene mutations in a form of juvenile amyotrophic lateral sclerosis (ALS4). Am J Hum Genet. 74, 1128-35.

Christensen, P.B., Hojer-Pedersen, E., Jensen, N.B., 1990. Survival of patients with amyotrophic lateral sclerosis in 2 Danish counties. Neurology. 40, 600-4.

Clement, A.M., et al., 2003. Wild-type nonneuronal cells extend survival of SOD1 mutant motor neurons in ALS mice. Science. 302, 113-7.

Cook, S.A., et al., 1995. Neuromuscular degeneration (nmd): a mutation on mouse chromosome 19 that causes motor neuron degeneration. Mamm Genome. 6, 187-91.

Cottenie, E., et al., 2014. Truncating and missense mutations in IGHMBP2 cause Charcot-Marie Tooth disease type 2. Am J Hum Genet. 95, 590-601.

Cox, G.A., Mahaffey, C.L., Frankel, W.N., 1998. Identification of the mouse neuromuscular degeneration gene and mapping of a second site suppressor allele. Neuron. 21, 1327-37.

Crawford, T.O., Pardo, C.A., 1996. The neurobiology of childhood spinal muscular atrophy. Neurobiol Dis. 3, 97-110.

de Planell-Saguer, M., et al., 2009. Biochemical and genetic evidence for a role of IGHMBP2 in the translational machinery. Hum Mol Genet. 18, 2115-26.

Degrauwe, N., et al., 2016. IMPs: an RNA-binding protein family that provides a link between stem cell maintenance in normal development and cancer. Genes Dev. 30, 2459-2474.

Deshler, J.O., et al., 1998. A highly conserved RNA-binding protein for cytoplasmic mRNA localization in vertebrates. Curr Biol. 8, 489-96.

Dessaud, E., McMahon, A.P., Briscoe, J., 2008. Pattern formation in the vertebrate neural tube: a sonic hedgehog morphogen-regulated transcriptional network. Development. 135, 2489-503.

Diers, A., et al., 2005. The ultrastructure of peripheral nerve, motor end-plate and skeletal muscle in patients suffering from spinal muscular atrophy with respiratory distress type 1 (SMARD1). Acta Neuropathol. 110, 289-97.

Dobin, A., et al., 2013. STAR: ultrafast universal RNA-seq aligner. Bioinformatics. 29, 15-21.

Dombert, B., et al., 2017. BDNF/trkB Induction of Calcium Transients through Cav2.2 Calcium Channels in Motoneurons Corresponds to F-actin Assembly and Growth Cone Formation on beta2-Chain Laminin (221). Front Mol Neurosci. 10, 346.

Donaghy, M., 1999. Classification and clinical features of motor neurone diseases and motor neuropathies in adults. J Neurol. 246, 331-3.

Donlin-Asp, P.G., Bassell, G.J., Rossoll, W., 2016. A role for the survival of motor neuron protein in mRNP assembly and transport. Curr Opin Neurobiol. 39, 53-61.

Donlin-Asp, P.G., et al., 2017a. The Survival of Motor Neuron Protein Acts as a Molecular Chaperone for mRNP Assembly. Cell Rep. 18, 1660-1673.

Donlin-Asp, P.G., Rossoll, W., Bassell, G.J., 2017b. Spatially and temporally regulating translation via mRNA-binding proteins in cellular and neuronal function. FEBS Lett. 591, 1508-1525.

Dull, T., et al., 1998. A third-generation lentivirus vector with a conditional packaging system. J Virol. 72, 8463-71.

Eckart, M., et al., 2012. The natural course of infantile spinal muscular atrophy with respiratory distress type 1 (SMARD1). Pediatrics. 129, e148-56.

Edgar, R., Domrachev, M., Lash, A.E., 2002. Gene Expression Omnibus: NCBI gene expression and hybridization array data repository. Nucleic Acids Res. 30, 207-10.

Ekestern, E., 2004. Neurotrophic factors and amyotrophic lateral sclerosis. Neurodegener Dis. 1, 88-100.

Eom, T., et al., 2003. Localization of a beta-actin messenger ribonucleoprotein complex with zipcode-binding protein modulates the density of dendritic filopodia and filopodial synapses. J Neurosci. 23, 10433-44.

Ericson, J., et al., 1996. Two critical periods of Sonic Hedgehog signaling required for the specification of motor neuron identity. Cell. 87, 661-73.

Eulalio, A., et al., 2007. P-body formation is a consequence, not the cause, of RNA-mediated gene silencing. Mol Cell Biol. 27, 3970-81.

Evergren, E., Benfenati, F., Shupliakov, O., 2007. The synapsin cycle: a view from the synaptic endocytic zone. J Neurosci Res. 85, 2648-56.

Fairman-Williams, M.E., Guenther, U.P., Jankowsky, E., 2010. SF1 and SF2 helicases: family matters. Curr Opin Struct Biol. 20, 313-24.

Fallini, C., et al., 2011. The survival of motor neuron (SMN) protein interacts with the mRNA-binding protein HuD and regulates localization of poly(A) mRNA in primary motor neuron axons. J Neurosci. 31, 3914-25.

Fallini, C., et al., 2014. Dynamics of survival of motor neuron (SMN) protein interaction with the mRNA-binding protein IMP1 facilitates its trafficking into motor neuron axons. Dev Neurobiol. 74, 319-332.

Fallini, C., et al., 2016. Deficiency of the Survival of Motor Neuron Protein Impairs mRNA Localization and Local Translation in the Growth Cone of Motor Neurons. J Neurosci. 36, 3811-20.

Farina, K.L., et al., 2003. Two ZBP1 KH domains facilitate beta-actin mRNA localization, granule formation, and cytoskeletal attachment. J Cell Biol. 160, 77-87.

Ferraiuolo, L., et al., 2011. Molecular pathways of motor neuron injury in amyotrophic lateral sclerosis. Nat Rev Neurol. 7, 616-30.

Fischer, U., Liu, Q., Dreyfuss, G., 1997. The SMN-SIP1 complex has an essential role in spliceosomal snRNP biogenesis. Cell. 90, 1023-9.

Furdui, C.M., et al., 2006. Autophosphorylation of FGFR1 kinase is mediated by a sequential and precisely ordered reaction. Mol Cell. 21, 711-7.

Giannini, A., et al., 2006. Respiratory failure in infants due to spinal muscular atrophy with respiratory distress type 1. Intensive Care Med. 32, 1851-5.

Giess, R., et al., 2002. Early onset of severe familial amyotrophic lateral sclerosis with a SOD-1 mutation: potential impact of CNTF as a candidate modifier gene. Am J Hum Genet. 70, 1277-86.

Gill, J.C., Moenter, S.M., Tsai, P.S., 2004. Developmental regulation of gonadotropin-releasing hormone neurons by fibroblast growth factor signaling. Endocrinology. 145, 3830-9.

Gilmartin, R.C., et al., 1977. Familial fatal neonatal radiculoneuropathy. Birth Defects Orig Artic Ser. 13, 95-101.

Golfmann, K., et al., 2018. Synergistic anti-angiogenic treatment effects by dual FGFR1 and VEGFR1 inhibition in FGFR1-amplified breast cancer. Oncogene.

Gorbalenya, A.E., et al., 1989. Two related superfamilies of putative helicases involved in replication, recombination, repair and expression of DNA and RNA genomes. Nucleic Acids Res. 17, 4713-30.

Gospodarowicz, D., Greene, G., Moran, J., 1975. Fibroblast growth factor can substitute for platelet factor to sustain the growth of Balb/3T3 cells in the presence of plasma. Biochem Biophys Res Commun. 65, 779-87.

Gospodarowicz, D., Moran, J.S., Mescher, A.L., 1978. Cellular specificities of fibroblast growth factor and epidermal growth factor. Symp Soc Dev Biol. 33-63.

Gregersen, L.H., et al., 2014. MOV10 Is a 5' to 3' RNA helicase contributing to UPF1 mRNA target degradation by translocation along 3' UTRs. Mol Cell. 54, 573-85.

Grohmann, K., et al., 1999. Diaphragmatic spinal muscular atrophy with respiratory distress is heterogeneous, and one form Is linked to chromosome 11q13-q21. Am J Hum Genet. 65, 1459-62.

Grohmann, K., et al., 2001. Mutations in the gene encoding immunoglobulin mu-binding protein 2 cause spinal muscular atrophy with respiratory distress type 1. Nat Genet. 29, 75-7.

Grohmann, K., et al., 2003. Infantile spinal muscular atrophy with respiratory distress type 1 (SMARD1). Ann Neurol. 54, 719-24.

Grohmann, K., et al., 2004. Characterization of Ighmbp2 in motor neurons and implications for the pathomechanism in a mouse model of human spinal muscular atrophy with respiratory distress type 1 (SMARD1). Hum Mol Genet. 13, 2031-42.

Gubbay, S.S., et al., 1985. Amyotrophic lateral sclerosis. A study of its presentation and prognosis. J Neurol. 232, 295-300.

Guenther, U.P., et al., 2004. Genomic rearrangements at the IGHMBP2 gene locus in two patients with SMARD1. Hum Genet. 115, 319-26.

Guenther, U.P., et al., 2007. Clinical and mutational profile in spinal muscular atrophy with respiratory distress (SMARD): defining novel phenotypes through hierarchical cluster analysis. Hum Mutat. 28, 808-15.

Guenther, U.P., et al., 2009a. IGHMBP2 is a ribosome-associated helicase inactive in the neuromuscular disorder distal SMA type 1 (DSMA1). Hum Mol Genet. 18, 1288-300.

Guenther, U.P., et al., 2009b. Clinical variability in distal spinal muscular atrophy type 1 (DSMA1): determination of steady-state IGHMBP2 protein levels in five patients with infantile and juvenile disease. J Mol Med (Berl). 87, 31-41.

Haidet-Phillips, A.M., et al., 2011. Astrocytes from familial and sporadic ALS patients are toxic to motor neurons. Nat Biotechnol. 29, 824-8.

Hansen, T.V., et al., 2004. Dwarfism and impaired gut development in insulin-like growth factor II mRNA-binding protein 1-deficient mice. Mol Cell Biol. 24, 4448-64.

Holden, P., Horton, W.A., 2009. Crude subcellular fractionation of cultured mammalian cell lines. BMC Research Notes. 2, 243.

Huang, E.J., Reichardt, L.F., 2001. Neurotrophins: roles in neuronal development and function. Annu Rev Neurosci. 24, 677-736.

Hubers, L., et al., 2011. HuD interacts with survival motor neuron protein and can rescue spinal muscular atrophy-like neuronal defects. Hum Mol Genet. 20, 553-79.

Huttelmaier, S., et al., 2005. Spatial regulation of beta-actin translation by Src-dependent phosphorylation of ZBP1. Nature. 438, 512-5.

Huxley, A.F., Stampfli, R., 1949. Evidence for saltatory conduction in peripheral myelinated nerve fibres. J Physiol. 108, 315-39.

Ibrahimi, O.A., et al., 2004. Kinetic model for FGF, FGFR, and proteoglycan signal transduction complex assembly. Biochemistry. 43, 4724-30.

Jablonka, S., et al., 2001. Co-regulation of survival of motor neuron (SMN) protein and its interactor SIP1 during development and in spinal muscular atrophy. Hum Mol Genet. 10, 497-505.

Jablonka, S., et al., 2007. Defective Ca2+ channel clustering in axon terminals disturbs excitability in motoneurons in spinal muscular atrophy. J Cell Biol. 179, 139-49.

Jablonka, S., et al., 2011. Therapeutic effects of PEGylated insulin-like growth factor I in the pmn mouse model of motoneuron disease. Exp Neurol. 232, 261-9.

Jankowsky, E., 2011. RNA helicases at work: binding and rearranging. Trends Biochem Sci. 36, 19-29.

Jedrzejowska, M., et al., 2014. Severe phenotypes of SMARD1 associated with novel mutations of the IGHMBP2 gene and nuclear degeneration of muscle and Schwann cells. Eur J Paediatr Neurol. 18, 183-92.

Jonson, L., et al., 2007. Molecular composition of IMP1 ribonucleoprotein granules. Mol Cell Proteomics. 6, 798-811.

Kaindl, A.M., et al., 2008. [Distal spinal-muscular atrophy 1 (DSMA1 or SMARD1)]. Arch Pediatr. 15, 1568-72.

Kalil, K., Dent, E.W., 2014. Branch management: mechanisms of axon branching in the developing vertebrate CNS. Nat Rev Neurosci. 15, 7-18.

Kanaan, J., et al., 2018. UPF1-like helicase grip on nucleic acids dictates processivity. Nat Commun. 9, 3752.

Kandel, E.R., et al., 2012. Principles of neural science., Vol., MacGraw-Hill.

Kanning, K.C., Kaplan, A., Henderson, C.E., 2010. Motor neuron diversity in development and disease. Annu Rev Neurosci. 33, 409-40.

Kaplan, D.R., Miller, F.D., 2000. Neurotrophin signal transduction in the nervous system. Curr Opin Neurobiol. 10, 381-91.

Kervestin, S., Jacobson, A., 2012. NMD: a multifaceted response to premature translational termination. Nat Rev Mol Cell Biol. 13, 700-12.

Kiernan, M.C., et al., 2011. Amyotrophic lateral sclerosis. Lancet. 377, 942-55.

Klausmeyer, A., et al., 2011. Influence of glial-derived matrix molecules, especially chondroitin sulfates, on neurite growth and survival of cultured mouse embryonic motoneurons. J Neurosci Res. 89, 127-41.

Kong, B., et al., 2014. Fibroblast growth factor 15 deficiency impairs liver regeneration in mice. Am J Physiol Gastrointest Liver Physiol. 306, G893-902.

Korinthenberg, R., et al., 1997. Congenital axonal neuropathy caused by deletions in the spinal muscular atrophy region. Ann Neurol. 42, 364-8.

Korsching, S., 1993. The neurotrophic factor concept: a reexamination. J Neurosci. 13, 2739-48.

Krieger, F., et al., 2013. Fast motor axon loss in SMARD1 does not correspond to morphological and functional alterations of the NMJ. Neurobiol Dis. 54, 169-82.

Krieger, F., et al., 2014a. Polyethylene glycol-coupled IGF1 delays motor function defects in a mouse model of spinal muscular atrophy with respiratory distress type 1. Brain. 137, 1374-93.

Krieger, F., Metzger, F., Jablonka, S., 2014b. Differentiation defects in primary motoneurons from a SMARD1 mouse model that are insensitive to treatment with low dose PEGylated IGF1. Rare Dis. 2, e29415.

Kulkarni, M., Ozgur, S., Stoecklin, G., 2010. On track with P-bodies. Biochem Soc Trans. 38, 242-51.

Kye, M.J., et al., 2014. SMN regulates axonal local translation via miR-183/mTOR pathway. Hum Mol Genet. 23, 6318-31.

Lee, J., et al., 2016. Astrocytes and Microglia as Non-cell Autonomous Players in the Pathogenesis of ALS. Exp Neurobiol. 25, 233-240.

Lee, K.J., Dietrich, P., Jessell, T.M., 2000. Genetic ablation reveals that the roof plate is essential for dorsal interneuron specification. Nature. 403, 734-40.

Leeds, P., et al., 1997. Developmental regulation of CRD-BP, an RNA-binding protein that stabilizes c-myc mRNA in vitro. Oncogene. 14, 1279-86.

Leenders, A.G., et al., 2001. Rab3a is involved in transport of synaptic vesicles to the active zone in mouse brain nerve terminals. Mol Biol Cell. 12, 3095-102.

Lefebvre, S., et al., 1998. The role of the SMN gene in proximal spinal muscular atrophy. Hum Mol Genet. 7, 1531-6.

Leung, K.M., et al., 2006. Asymmetrical beta-actin mRNA translation in growth cones mediates attractive turning to netrin-1. Nat Neurosci. 9, 1247-56.

Levi-Montalcini, R., 1987. The nerve growth factor 35 years later. Science. 237, 1154-62.

Lewin, G.R., Barde, Y.A., 1996. Physiology of the neurotrophins. Annu Rev Neurosci. 19, 289-317.

Lim, S.C., et al., 2012. The Ighmbp2 helicase structure reveals the molecular basis for disease-causing mutations in DMSA1. Nucleic Acids Res. 40, 11009-22.

Lunn, M.R., Wang, C.H., 2008. Spinal muscular atrophy. Lancet. 371, 2120-33.

Luo, L., 2002. Actin cytoskeleton regulation in neuronal morphogenesis and structural plasticity. Annu Rev Cell Dev Biol. 18, 601-35.

Luttmann, W., et al., 2009. Der Experimentator: Immunologie, Vol. 3, Springer Spektrum, Berlin, Heidelberg.

Maddatu, T.P., et al., 2004. Transgenic rescue of neurogenic atrophy in the nmd mouse reveals a role for Ighmbp2 in dilated cardiomyopathy. Hum Mol Genet. 13, 1105-15.

Maddatu, T.P., et al., 2005. Dilated cardiomyopathy in the nmd mouse: transgenic rescue and QTLs that improve cardiac function and survival. Hum Mol Genet. 14, 3179-89.

Mayford, M., et al., 1996. Control of memory formation through regulated expression of a CaMKII transgene. Science. 274, 1678-83.

Maystadt, I., et al., 2004. Allelic heterogeneity of SMARD1 at the IGHMBP2 locus. Hum Mutat. 23, 525-6.

McWilliam, R.C., et al., 1985. Diaphragmatic paralysis due to spinal muscular atrophy. An unrecognised cause of respiratory failure in infancy? Archives of Disease in Childhood. 60, 145-149.

Medioni, C., et al., 2014. Imp promotes axonal remodeling by regulating profilin mRNA during brain development. Curr Biol. 24, 793-800.

Meister, G., et al., 2000. Characterization of a nuclear 20S complex containing the survival of motor neurons (SMN) protein and a specific subset of spliceosomal Sm proteins. Hum Mol Genet. 9, 1977-86.

Mellins, R.B., et al., 1974. Respiratory distress as the initial manifestation of Werdnig-Hoffmann disease. Pediatrics. 53, 33-40.

Meyer, K., et al., 2014. Direct conversion of patient fibroblasts demonstrates non-cell autonomous toxicity of astrocytes to motor neurons in familial and sporadic ALS. Proc Natl Acad Sci U S A. 111, 829-32.

Mizuta, T.R., et al., 1993. Isolation of cDNA encoding a binding protein specific to 5'-phosphorylated single-stranded DNA with G-rich sequences. Nucleic Acids Res. 21, 1761-6.

Mohan, U., et al., 2001. Inherited early onset severe axonal polyneuropathy with respiratory failure and autonomic involvement. Neuromuscul Disord. 11, 395-9.

Moradi, M., et al., 2017. Differential roles of alpha-, beta-, and gamma-actin in axon growth and collateral branch formation in motoneurons. J Cell Biol. 216, 793-814.

Murphy, N.P., Davidson, D.C., Bouton, J., 1985. Diaphragmatic paralysis due to spinal muscular atrophy. Arch Dis Child. 60, 495.

Murray, L.M., et al., 2013. Defects in neuromuscular junction remodelling in the Smn(2B/-) mouse model of spinal muscular atrophy. Neurobiol Dis. 49, 57-67.

Nicastro, G., et al., 2017. Mechanism of beta-actin mRNA Recognition by ZBP1. Cell Rep. 18, 1187-1199.

Nielsen, J., et al., 1999. A family of insulin-like growth factor II mRNA-binding proteins represses translation in late development. Mol Cell Biol. 19, 1262-70.

Niewidok, B., et al., 2018. Single-molecule imaging reveals dynamic biphasic partition of RNA-binding proteins in stress granules. The Journal of Cell Biology. 217, 1303-1318.

Nishino, J., et al., 2013. A network of heterochronic genes including Imp1 regulates temporal changes in stem cell properties. Elife. 2, e00924.

Nomura, T., et al., 2013. Catastrophic autonomic crisis with cardiovascular collapse in spinal muscular atrophy with respiratory distress type 1. J Child Neurol. 28, 949-51.

Novelli, G., et al., 1995. Neonatal spinal muscular atrophy with diaphragmatic paralysis is unlinked to 5q11.2-q13. Journal of Medical Genetics. 32, 216-219.

Oppenheim, R.W., 1991. Cell death during development of the nervous system. Annu Rev Neurosci. 14, 453-501.

Ornitz, D.M., Itoh, N., 2015. The Fibroblast Growth Factor signaling pathway. Wiley Interdiscip Rev Dev Biol. 4, 215-66.

Patel, V.L., et al., 2012. Spatial arrangement of an RNA zipcode identifies mRNAs under post-transcriptional control. Genes Dev. 26, 43-53.

Pellizzoni, L., et al., 2001. A functional interaction between the survival motor neuron complex and RNA polymerase II. J Cell Biol. 152, 75-85.

Peritz, T., et al., 2006. Immunoprecipitation of mRNA-protein complexes. Nat.Protoc. 1, 577-580.

Perrin, B.J., Ervasti, J.M., 2010. The actin gene family: function follows isoform. Cytoskeleton (Hoboken). 67, 630-4.

Pitt, M., et al., 2003. Severe infantile neuropathy with diaphragmatic weakness and its relationship to SMARD1. Brain. 126, 2682-92.

Poets, C., et al., 1990. [Acute respiratory insufficiency as the initial clinical manifestation of spinal muscular atrophy]. Monatsschr Kinderheilkd. 138, 157-9.

Pollard, T.D., Cooper, J.A., 2009. Actin, a central player in cell shape and movement. Science. 326, 1208-12.

Porro, F., et al., 2014. The wide spectrum of clinical phenotypes of spinal muscular atrophy with respiratory distress type 1: a systematic review. J Neurol Sci. 346, 35-42.

Potthoff, M.J., Kliewer, S.A., Mangelsdorf, D.J., 2012. Endocrine fibroblast growth factors 15/19 and 21: from feast to famine. Genes Dev. 26, 312-24.

Rathod, R., et al., 2012. Laminin induced local axonal translation of beta-actin mRNA is impaired in SMN-deficient motoneurons. Histochem Cell Biol. 138, 737-48.

Rehberg, M., et al., 2008. A new non-disruptive strategy to target calcium indicator dyes to the endoplasmic reticulum. Cell Calcium. 44, 386-99.

Robitaille, R., et al., 1993. Functional colocalization of calcium and calcium-gated potassium channels in control of transmitter release. Neuron. 11, 645-55.

Ross, A.F., et al., 1997. Characterization of a beta-actin mRNA zipcode-binding protein. Mol Cell Biol. 17, 2158-65.

Rossoll, W., et al., 2003. Smn, the spinal muscular atrophy-determining gene product, modulates axon growth and localization of beta-actin mRNA in growth cones of motoneurons. J Cell Biol. 163, 801-12.

Roux, P.P., Topisirovic, I., 2012. Regulation of mRNA translation by signaling pathways. Cold Spring Harb Perspect Biol. 4.

Rudnik-Schoneborn, S., et al., 1996. Clinical spectrum and diagnostic criteria of infantile spinal muscular atrophy: further delineation on the basis of SMN gene deletion findings. Neuropediatrics. 27, 8-15.

Rudnik-Schoneborn, S., et al., 2004. Long-term observations of patients with infantile spinal muscular atrophy with respiratory distress type 1 (SMARD1). Neuropediatrics. 35, 174-82.

Ruiz, R., et al., 2010. Altered intracellular Ca2+ homeostasis in nerve terminals of severe spinal muscular atrophy mice. J Neurosci. 30, 849-57.

Sambataro, F., Pennuto, M., 2012. Cell-autonomous and non-cell-autonomous toxicity in polyglutamine diseases. Prog Neurobiol. 97, 152-72.

Sanchez, G., et al., 2013. A novel function for the survival motoneuron protein as a translational regulator. Hum Mol Genet. 22, 668-84.

Sasaki, Y., et al., 2010. Phosphorylation of zipcode binding protein 1 is required for brain-derived neurotrophic factor signaling of local beta-actin synthesis and growth cone turning. J Neurosci. 30, 9349-58.

Schapira, D., Swash, M., 1985. Neonatal spinal muscular atrophy presenting as respiratory distress: A clinical variant. Muscle & Nerve. 8, 661-663.

Schlessinger, J., et al., 2000. Crystal structure of a ternary FGF-FGFR-heparin complex reveals a dual role for heparin in FGFR binding and dimerization. Mol Cell. 6, 743-50.

Schmidt, E.K., et al., 2009. SUnSET, a nonradioactive method to monitor protein synthesis. Nat Methods. 6, 275-7.

Schmidt, R.F., 2001. Physiologie kompakt, Vol.

Segal, R.A., Greenberg, M.E., 1996. Intracellular signaling pathways activated by neurotrophic factors. Annu Rev Neurosci. 19, 463-89.

Sendtner, M., et al., 1992. Ciliary neurotrophic factor prevents degeneration of motor neurons in mouse mutant progressive motor neuronopathy. Nature. 358, 502-4.

Sendtner, M., et al., 2000. Developmental motoneuron cell death and neurotrophic factors. Cell Tissue Res. 301, 71-84.

Sendtner, M., 2014. Motoneuron disease. Handb Exp Pharmacol. 220, 411-41.

Shababi, M., et al., 2016. Rescue of a Mouse Model of Spinal Muscular Atrophy With Respiratory Distress Type 1 by AAV9-IGHMBP2 Is Dose Dependent. Mol Ther. 24, 855-66.

Shaw, P.J., 2001. Genetic inroads in familial ALS. Nat Genet. 29, 103-4.

Simone, C., et al., 2014. iPSC-Derived neural stem cells act via kinase inhibition to exert neuroprotective effects in spinal muscular atrophy with respiratory distress type 1. Stem Cell Reports. 3, 297-311.

Sivan, Y., Galvis, A., 1990. Early Diaphragmatic Paralysis:In Infants with Genetic Disorders. Clinical Pediatrics. 29, 169-171.

Song, A.H., et al., 2009. A selective filter for cytoplasmic transport at the axon initial segment. Cell. 136, 1148-60.

Strasswimmer, J., et al., 1999. Identification of survival motor neuron as a transcriptional activator-binding protein. Hum Mol Genet. 8, 1219-26.

Surrey, V., Jablonka, S., 2018. Disease mechanisms in spinal muscular atrophy with respiratory distress type 1 (SMARD1): what about motoneurons? Medical Research Archives. 6, 1-10.

Surrey, V., et al., 2018. Impaired Local Translation of beta-actin mRNA in Ighmbp2-Deficient Motoneurons: Implications for Spinal Muscular Atrophy with respiratory Distress (SMARD1). Neuroscience. 386, 24-40.

Suter, D.M., Miller, K.E., 2011. The emerging role of forces in axonal elongation. Prog Neurobiol. 94, 91-101.

Suzuki, M., et al., 2008. betaKlotho is required for fibroblast growth factor (FGF) 21 signaling through FGF receptor (FGFR) 1c and FGFR3c. Mol Endocrinol. 22, 1006-14.

Taylor, M.S., et al., 2013. Affinity proteomics reveals human host factors implicated in discrete stages of LINE-1 retrotransposition. Cell. 155, 1034-48.

Taylor, T.D., et al., 2006. Human chromosome 11 DNA sequence and analysis including novel gene identification. Nature. 440, 497-500.

Thoenen, H., Barde, Y.A., 1980. Physiology of nerve growth factor. Physiol Rev. 60, 1284-335.

Thoenen, H., 1995. Neurotrophins and neuronal plasticity. Science. 270, 593-8.

Tintignac, L.A., Brenner, H.R., Ruegg, M.A., 2015. Mechanisms Regulating Neuromuscular Junction Development and Function and Causes of Muscle Wasting. Physiol Rev. 95, 809-52.

Tom Dieck, S., et al., 2012. Metabolic labeling with noncanonical amino acids and visualization by chemoselective fluorescent tagging. Curr Protoc Cell Biol. Chapter 7, Unit7.11.

Trapnell, C., et al., 2012. Differential gene and transcript expression analysis of RNA-seq experiments with TopHat and Cufflinks. Nat Protoc. 7, 562-78.

Ugolini, F., et al., 1999. Differential expression assay of chromosome arm 8p genes identifies Frizzled-related (FRP1/FRZB) and Fibroblast Growth Factor Receptor 1 (FGFR1) as candidate breast cancer genes. Oncogene. 18, 1903-10.

Urbanska, A.S., et al., 2017. ZBP1 phosphorylation at serine 181 regulates its dendritic transport and the development of dendritic trees of hippocampal neurons. Sci Rep. 7, 1876.

Vincentz, J.W., et al., 2005. Fgf15 is required for proper morphogenesis of the mouse cardiac outflow tract. Genesis. 41, 192-201.

Wang, K., et al., 2018. FGFR1-ERK1/2-SOX2 axis promotes cell proliferation, epithelial-mesenchymal transition, and metastasis in FGFR1-amplified lung cancer. Oncogene.

Wiese, S., et al., 2010. Isolation and enrichment of embryonic mouse motoneurons from the lumbar spinal cord of individual mouse embryos. Nat.Protoc. 5, 31-38.

Wilmshurst, J.M., et al., 2001. Severe infantile axonal neuropathy with respiratory failure. Muscle Nerve. 24, 760-8.

Wong, V.C., et al., 2006. Mutation of gene in spinal muscular atrophy respiratory distress type I. Pediatr Neurol. 34, 474-7.

Wood, S.J., Slater, C.R., 2001. Safety factor at the neuromuscular junction. Prog Neurobiol. 64, 393-429.

Woodbury, M.E., Ikezu, T., 2014. Fibroblast growth factor-2 signaling in neurogenesis and neurodegeneration. J Neuroimmune Pharmacol. 9**,** 92-101.

Xu, K., Zhong, G., Zhuang, X., 2013. Actin, spectrin, and associated proteins form a periodic cytoskeletal structure in axons. Science. 339**,** 452-6.

Yisraeli, J.K., 2005. VICKZ proteins: a multi-talented family of regulatory RNA-binding proteins. Biol Cell. 97**,** 87-96.

Zufferey, R., et al., 1998. Self-inactivating lentivirus vector for safe and efficient in vivo gene delivery. J Virol. 72**,** 9873-80.

7. Attachment

7.1 List of Figures

7.2 List of Tables

7.3 List of Abbreviations

A	aaRS	Cytoplasmic tRNA synthetase
	AB	Antibody
	ACh	Acetylcholine
	AChRs	Acetylcholine receptors
	AGO2	Argonaute 2
	AHA	L-azidohomoalanine
	AIS	Axon initial segment
	Akt	Protein kinase B
	ALS	Amyotrophic lateral sclerosis
	ALS4	Juvenile form of ALS
	ATP	Adenosine triphosphate
B	BCA	Bicinchoninic acid
	BDNF	Brain-derived neurotrophic factor
	bFGF	Basic fibroblast growth factor
	Bp	Base pairs
	BSA	Bovine serum albumin
C	Ca^{2+}	Calcium
	CaM kinase	Ca^{2+}/calmodulin-dependent protein kinase II
	cDNA	Complementary DNA
	Ch.	Chapter
	CMT2	Charcot-Marie-Tooth type 2
	CNS	Central nervous system
	CNTF	Ciliary neurotrophic factor
	CO_2	Carbon dioxide
	Co-IP	Co-immunoprecipitation
	Cont.	Continuous
	Ctrl	Control
D	DAPI	4′,6-Diamidino-2-Phenylindole
	DIG	Digoxigenin
	DIV	Days *in vitro*
	DMEM	Dulbecco´s Modified Eagle Medium)
	DMP	Dimethyl-pimelimidate
	DMSO	Dimethyl sulfoxide
	DNA	Deoxyribonucleic acid
	DSMA1	Distal spinal muscular atrophy type 1
E	E	Embryonal day
	E. coli	Escherichia coli
	ECL	Enhanced chemiluminescence
	Egf	Epidermal growth factor
	Elong.	Elongation
	ELPHO	Electrophoresis buffer
	EPP	Endplate potential
	et al.	Et alii/aliae
F	FC	Fold change
	FCS	Fetal Calf Serum
	FGFR1	*Fibroblast growth factor receptor 1*
	Fig.	Figure

	Fiji	Fiji is just ImageJ
	FISH	Fluorescence *in situ* hybridization
	FPKM	Fragments per kilobase million
	FRAP	Fluorescence recovery after photobleaching
	FT	Flow-through
	FUNCAT	Fluorescent noncanonical amino acid tagging
G	GAPDH	Glyeraldehyde 3-phosphate dehydrogenase
	GC	Growth cone
	GDNF	Glia-derived neurotrophic factor
	GFP	Green fluorescent protein
	GST	Glutathione Sepharose transferase
	GTP	Guanosine triphosphate
H	h	Hours
	HBSS	Hank's Balanced Salt Solution
	HD	Homeodomain
	heparin/HS	Heparin/heparan sulfate
	HEPES	4-(2-hydroxyethyl)-1-piperazineethanesulfonic acid
	HGF	Hepatocyte growth factor
	Hz	Hertz
I	ICC	Immunocytochemical staining
	Ig	Immunoglobulin
	IGF	Insulin-like growth-factor
	Igfbp-2/-3/-5 and -6	Insulin-like growth factor binding protein-2/-3/-5 and -6
	Igf-I/-II	Insulin growth factor-I and II
	IGHMBP2	Immunoglobulin μ-binding protein 2
	Ighmbp2-def.	Ighmbp2-deficient
	IMP1	Insulin-like growth factor-2 mRNA binding protein 1
	IP	Immunoprecipitation
	IPTG	Isopropyl-β-D-thiogalactopyranoside
K	KD	Knockdown
	kDa	Kilodalton
L	laminin-111	Schwann cell-specific laminin isoform
	laminin-211/221	Synapse-specific laminin isoform
	LIF	Leukemia inhibitory factor
	LNA	Locked nucleic acid
	LSM4	U6 snRNA-associated Sm-like protein 4
M	M	Molar
	MAPK	Mitogen-activated protein kinase
	M-Csf	Macrophage colony-stimulating factor
	mEPC	Miniature endplate current
	min	Minutes
	ml	Milliliter
	MN	Motoneuron
	MOV10	Moloney leukemia virus 10
	mRNA	Messenger ribonucleic acid
	mRNP	Messenger ribonucleoprotein
	mV	Millivolt
N	n	Number of experiments
	n.s.	Not significant

	nA	Nanoampere
	NB	Neurobasal
	Ni-NTA	Nickel nitrilotriacetic acid agarose
	nmd	Neuromuscular degeneration
	NMD	Nonsense-mediated decay
	Nmd^{2J}	Neuromuscular disorder
	NMJ	Neuromuscular junction
O	OD	Optical density
	OGB	Oregon Green 488 BAPTA-1
P	P	Postnatal day
	PBS	Phosphate-buffered saline
	PCR	Polymerase chain reaction
	PD	Pulldown
	PEG-IGF1	Polyethylene glycol-coupled insulin growth factor 1
	PFA	Paraformaldehyde
	pH	Potentia hydrogenii
	PI3K	Phosphatidylinositol-4,5-bisphosphate 3-kinase
	PLCγ	Phospholipase C gamma
	Pmn	Progressive motor neuropathy
	PNS	Peripheral nervous system
	POD	Peroxidase
	PORN-H	Poly-DL-ornithine hydrobromide
	pSILAC	Pulsed Stable Isotope Labeling by Amino acids in cell culture
	PVDF	Polyvinylidene fluoride
Q	QL	Quantum levels
R	rcf	Relative centrifugal force
	RIP	Immunoprecipitation of mRNA-protein complexes
	RIPA	Radioimmunoprecipitation assay
	RNA	Ribonucleic acid
	RNA-Seq	RNA-Sequencing
	ROIs	Regions of interest
	rpm	Revolutions per minute
	RT	Room temperature
	RT-PCR	Quantitative real-time PCR
S	Sars2	Mitochondrial Serine-tRNA ligase
	SBMA	Spinal and bulbar muscular atrophy
	SD	Standard deviation
	SDS	Sodium dodecyl sulfate
	sec	Seconds
	SEM	Standard error of the mean
	SF family	Scatter factor family
	SF1	Superfamily 1
	SFs	Superfamilies
	sh	Short hairpin
	Shh	Sonic hedgehog
	sh*Ighmbp2*	KD of *Ighmbp2* gene
	SMA	Spinal muscular atrophy
	SMARD1	Spinal muscular atrophy with respiratory distress type 1
	SMN1	Survival motor neuron gene 1

	SSC	Saline-sodium citrate
	STAT	Signal transducer and activator of transcription
	SUnSET	SUrface SEnsing of Translation
T	Tab.	Table
	TAE buffer	Tris-acetate-EDTA buffer
	TBS-T	Tris-buffered saline with TWEEN20
	Temp.	Temperature
	TNRC6B	Trinucleotide repeat-containing gene 6B protein
	Top1	DNA topoisomerase 1
	Trans.	Transition
	Tris	Tris (hydroxymethyl) -aminomethane
	tRNA	Transfer RNA
	tyr. tubulin	Tyrosinated tubulin
U	Upf1	Up-frameshift 1
	UV	Ultraviolet
V	V	Volt
	Vegf-R1/3	Vascular endothelial growth factor receptor-1/3
W	w/	With
	w/o	Without
	WB	Western blot
	wt	Wildtype
others	α	Alpha/anti
	β	Beta
	γ	Gamma
	%	Percentage
	°C	Degrees Celcius
	µg	Microgram
	µl	Microliter
	µm	Micrometer

7.4 Acknowledgments

First of all, I would like to thank my supervisor PD Dr. Sibylle Jablonka, who offered me the opportunity to work on this interesting and challenging topic in her working group. I thank her for the continuous support, the inspiring and critical discussions and her trust in my work. I highly appreciate her guidance and valuable support in writing this thesis.

I would like to extend my thanks to Prof. Dr. Utz Fischer for his interest in my Ph.D. thesis and encouragement as one of my supervisors. I thank him for the constant support, the numerous pieces of advice and the instructive time.

Likewise, I want to thank Prof. Dr. Carmen Villmann for her support as my supervisor, many pieces of advice and the evaluation of my thesis.

Prof. Dr. Markus Sauer I want to thank for taking over the job of the chairperson during my defense.

I would like to thank the Studienstiftung des Deutschen Volkes for the encouragement of professional skills and financial support.

Within my working group, I would like to thank several people, without whom this work would not have been possible and the laboratory time would certainly have been desolating. Nicole Rachor, I thank you and your helping hands, without whom some experiments would never have been possible. Stefanie Balk, I thank you for your companionship - you made the time of my Ph.D. much nicer and have become a friend to me. My two master students, Caren Zöller and Alicia Andrea Lork, also deserve great thanks. Your energetic support was incredibly precious to me.

I would also like to thank Prof. Dr. Michael Sendtner and all members of the Institute of Clinical Neurobiology for the great working atmosphere and good cooperation. I would like to thank all Ph.D. students and Postdocs for the uncomplicated way to discuss results and for their great fellowship. I especially would like to thank Dr. Mehri Moradi, Dr. Benjamin Rüdt von Collenberg and Dr. Micheal Briese for their expert support and many pieces of advice.

Special thanks also go to Dr. Lena Saal-Bauernschubert and Vivien-Charlott Stadler. Thank you for your commitment, the supportive words and the intensive evaluation of this thesis. Your help was invaluable for the achievement of this work.

At this point, I would also like to thank all my friends who accompanied me during my studies and ensured the necessary balance.

Two people have always been at my side during my Ph.D. thesis and therefore have a special value for me - Thomas Andreska and Linda Full (soon Andreska). I thank you for your support, all the conversations, the distractions and especially your friendship. To know you next to me fills me with pride and I do not want to miss you in my life!

My heartfelt thanks likewise go to my parents - Birgit and Volker Urban. You have accompanied me from the beginning of my study, supported me in several aspects, helped me with proofreading and always believed in me. I thank you from the bottom of my heart!
I would also like to thank the rest of my family most sincerely. I thank you for your unconditional support and interest.

7.5 Curriculum Vitae

7.6 Affidavit / Eidesstattliche Erklärung

Affidavit

I hereby confirm that my thesis entitled **"Identification of affected cellular targets, mechanisms and signaling pathways in a mouse model for spinal muscular atrophy with respiratory distress type 1 (SMARD1)"** is the result of my own work. I did not receive any help or support from commercial consultants. All sources and/or materials applied are listed and specified in the thesis.

Furthermore, I confirm that this thesis has not yet been submitted as part of another examination process neither in identical nor in similar form.

Würzburg.....

Date Signature

Eidesstattliche Erklärung

Hiermit erkläre ich an Eides statt, die Dissertation **„Identifizierung betroffener zellulärer Zielmoleküle, Mechanismen und Signalwege in einem Maus-Modell für spinale Muskelatrophie mit Ateminsuffizienz Typ 1 (SMARD1)"** eigenständig, d.h. insbesondere selbstständig und ohne Hilfe eines kommerziellen Promotionsberaters, angefertigt und keine anderen als die von mir angegebenen Quellen und Hilfsmittel verwendet zu haben.

Ich erkläre außerdem, dass die Dissertation weder in gleicher noch in ähnlicher Form bereits in einem anderen Prüfungsverfahren vorgelegen hat.

Würzburg.....

Datum Unterschrift